# DEVELOPMENT OF A NEW COLLOID FILTRATION THEORY IN THE PRESENCE OF ENERGY BARRIERS VIA DISCRETE NANOSCALE HETEROGENEITY

by

Eddy Fernando Pazmiño

A dissertation submitted to the faculty of
The University of Utah
in partial fulfillment of the requirements for the degree of

Doctor of Philosophy

in

Geological Engineering

Department of Geology and Geophysics

The University of Utah

August 2015

**The University of Utah Graduate School**

# STATEMENT OF DISSERTATION APPROVAL

The dissertation of **Eddy Fernando Pazmiño**

has been approved by the following supervisory committee members:

| | | |
|---|---|---|
| **William P. Johnson** | , Chair | 3/19/2015<br>Date Approved |
| **Douglas K. Solomon** | , Member | 12/09/2014<br>Date Approved |
| **Vladimir Hlady** | , Member | 12/09/2014<br>Date Approved |
| **Diego P. Fernandez** | , Member | 12/09/2014<br>Date Approved |
| **Bruce K. Gale** | , Member | 12/09/2014<br>Date Approved |

and by **William P. Johnson** , Associate Chair

of the Department of **Geology and Geophysics**

and by David B. Kieda, Dean of The Graduate School.

## ABSTRACT

Traditional colloidal filtration theory (CFT) predicts zero attachment when repulsion exists between colloid and filtering media (collector). Notably, repulsion is prevalent in environmental systems, e.g., riverbank filtration, and is manifested as energy barriers to attachment due to electro osmotic interactions between surfaces of the same charge. A mechanistic particle trajectory model that incorporates discrete nanoscale attractive zones (heterodomains) to account for attachment under bulk repulsive colloid-collector interactions was developed and tested against an array of direct observation experiments conducted in an impinging jet system. Retention of 0.25 to 1.95 μm colloids on soda-lime glass slides was examined for 6 and 20 mM ionic strengths (IS) and average jet velocities of $1.7x10^{-3}$ to $5.94x10^{-3}$ $ms^{-1}$ (equivalent pore water velocity of 1.9 and 8.2 $mday^{-1}$, respectively) in order to characterize the heterodomain size distribution and surface coverage. Simulations indicate that a power law distribution of 60 and 120 nm radii heterodomains (4:1 number ratio) and 0.04% surface coverage is able to quantitatively capture observed retention across all conditions examined. Furthermore, the same heterogeneity characteristics were able to capture qualitative trends of release of colloids deposited in contact with heterodomains in response to perturbations in flow and IS relative to the loading condition, i.e., factor 25 increase in jet velocity or factor 20 decrease in IS. Finally, a correlation equation was developed to incorporate the mechanistic basis provided from the discrete heterogeneity model and calibrated from the

array of experiments. The equation is a function of the colloidal number, which captures the main characteristics of the energy barrier, and the fraction of colloids that persist in the near surface fluid domain (secondary minimum) obtained from a Maxwell distribution of kinetic energies. Notably, the proposed correlation equation captures scores of experiments reported in the literature for a broad range of conditions for colloid sizes ranging from 0.06 to 3.1 μm, IS from 0.1 to 300 mM, and average pore water velocities from 4 to 588 $mday^{-1}$on soda-lime glass beads. The main coefficient of the correlation equation is a linear function heterodomain surface coverage, indicating that different coefficients may capture filtration across different aquifer-relevant minerals.

*A la memoria de Celia María Saavedra*

TABLE OF CONTENTS

# ACKNOWLEDGEMENTS

I want to thank Bill Johnson for his support and close guidance during all the stages of this work. Additionally, I want to thank my fellow graduate students that collaborated with the colloid transport project. Thanks a lot to my family and friends in Ecuador who supported me all the time. Special thanks to Tash, who supported me and provided valuable feedback during the composition of this document. Finally, thanks to all the friends from all over the world that I met in Salt Lake City during this last six years.

This research was supported by the U.S. National Science Foundation Chemical, Biological and Environmental Transport, and Hydrological Sciences Programs (awards 0822102 and 1215726 respectively). Any opinions, findings, and conclusions or recommendations expressed in this material are those of the authors and do not necessarily reflect the views of the National Science Foundation.

# CHAPTER 1

# INTRODUCTION

Colloid transport in the subsurface is a key environmental process that governs the extent of contamination of viruses, bacteria, and protozoa in aquifers. Additionally, in engineering applications, this process determines the design of low energy river-bank filtration systems, water sources set-back distances from contaminant sources, and in situ remediation via engineered nanoparticles.

However, colloid transport in the subsurface is not fully understood due to the complexity of the interactions that govern colloid removal under environmental (unfavorable) conditions. At these conditions energy barriers are manifested as repulsive forces between colloid and filtering surface (collector). While traditional colloid filtration theory (CFT) accounts for this interactions via a mechanistic force and torque balance in order to simulate colloid trajectories,[1,2] CFT predicts zero attachment when any significant energy barrier exists. This limitation arises from the assumption that all surfaces are homogeneously repulsive, i.e., surface properties don't change spatially.

An alternative approach is to incorporate discrete surface heterogeneity to mechanistically account for colloid attachment under bulk-repulsive conditions.[3–5] In this work we incorporate this strategy via discrete nanoscale zones (heterodomains) of local attraction (opposite surface charge). However, the determination of size and spatial distribution of heterodomain at the scale relevant to colloid interactions and across a

representative area is a paradigm that remains intractable. Therefore, the hypothesis tested in Chapter 2 is that heterogeneity characteristics (size and surface coverage) of the soda-lime glass slides can be extracted via comparison of simulations with impinging jet direct observation experiments for a comprehensive range of conditions, i.e., different colloid sizes, ionic strengths (IS), and fluid velocities.

In Chapter 3, release of colloids attached over heterodomains in response to flow and IS perturbations is examined via simulations and direct observation experiments in order to further test the heterodomain characteristics extracted in Chapter 2. Additionally, a sensitivity analysis of adhesion parameters that govern colloid immobilization is provided.

In Chapter 4, a correlation equation is developed from the discrete heterogeneity results in order to provide a versatile predictor of colloid attachment in porous media. The correlation equation is tested against numerous soda-lime glass bead packed column experiments reported in the literature.

## References

(1) Yao, K.-M.; Habibian, M. T.; O'Melia, C. R. Water and Wastewater Filtration: Concepts and Applications. *Environ. Sci. Technol.* **1971,** *5* (11), 1105–1112.

(2) Rajagopalan, R.; Tien, C. Trajectory Analysis of Deep-bed Filtration with the Sphere-in-cell Porous Media Model. *AIChE J.* **1976,** *22* (3), 523–533.

(3) Duffadar, R. D.; Davis, J. M. Interaction of Micrometer-scale Particles with Nanotextured Surfaces in Shear Flow. *J. Colloid Interface Sci.* **2007,** *308* (1), 20–29.

(4) Duffadar, R. D.; Davis, J. M. Dynamic Adhesion Behavior of Micrometer-scale Particles Flowing over Patchy Surfaces with Nanoscale Electrostatic Heterogeneity. *J. Colloid Interface Sci.* **2008,** *326* (1), 18–27.

(5) Ma, H.; Pazmino, E.; Johnson, W. P. Surface Heterogeneity on Hemispheres-in-

cell Model Yields all Experimentally-observed Non-straining Colloid Retention Mechanisms in Porous Media in the Presence of Energy Barriers. *Langmuir* **2011,** *27* (24), 14982–14994.

# CHAPTER 2

# POWER-LAW SIZE-DISTRIBUTED HETEROGENEITY EXPLAINS COLLOID RETENTION ON SODA-LIME GLASS IN THE PRESENCE OF ENERGY BARRIERS


## Abstract

This paper concerns reading the nanoscale heterogeneity thought responsible for colloid retention on surfaces in the presence of energy barriers (unfavorable attachment conditions). We back out this heterogeneity on glass surfaces by comparing mechanistic simulations incorporating discrete heterogeneity with colloid deposition experiments performed across a comprehensive set of experimental conditions. Original data are presented for attachment to soda lime glass for three colloid sizes (0.25, 1.1, and 1.95 μm microspheres) under a variety of ionic strengths and fluid velocities in an impinging jet system. Comparison of mechanistic particle trajectory simulations incorporating discrete surface heterogeneity represented by nanoscale zones of positive charge (heterodomains) indicates that a power-law size distribution of heterodomains ranging in size from 120 to 60 nm in radius was able to explain observed retention for all conditions examined. In contrast, uniform and random placement of single-sized heterodomains failed to capture experimentally-observed colloid retention across the range of conditions examined.

## Introduction

No functional, easily applied theory yet exists to quantitatively predict colloid retention in porous media in the presence of energy barriers (unfavorable colloid attachment conditions), which is thought to be the prevalent condition in environmental systems. Existing heuristic expressions derived from colloidal filtration theory (CFT)[1–5] predict zero colloid attachment even under modestly unfavorable conditions[6] because they rely on mean-field approaches which assume that measured surface characteristics (e.g., ζ–potentials) are equivalent all across the given surface(s). Whereas mean–field approaches predict a lack of colloid attachment in the presence of significant energy barriers, their power derives from an ability to qualitatively predict trends in experimentally-observed retention, i.e., increasing colloid retention with increased solution ionic strengthh.[6, 7] Increasing ionic strength reduces the energy barrier by compressing electric double layer repulsion closer to the surface, where the van der Waals forces are greater. However, mean-field DLVO parameters yield a very stiff dependence of simulated attachment on ionic strength, which does not reflect more gradual experimentally-observed trends.[6, 8–10] These outcomes of the mean field approach has long led to the expectation that nano- to microscale heterogeneity (e.g., charge or roughness) locally reduces or eliminates repulsion and is responsible for colloid attachment in the presence of energy barriers.

Direct assay of surface heterogeneity (e.g., via x-ray photoelectron spectroscopy or other techniques) has no simple or direct translation to spatial variation in surface properties directly relevant to colloid-surface interaction, e.g., ζ–potentials. Whereas the force volume approach of atomic force microscopy (AFM) [11–13] directly yields colloid-

surface interaction forces over an area, it is highly laborious to perform force volume imaging over a representative area of the collector at the resolution corresponding to colloid-collector interactions. Furthermore, colloidal probe measurements for < 0.5 μm colloids are very challenging because of the small size of the colloid relative to the cantilever and the limited range in cantilever sensitivity (spring constant).

While direct exploration of spatial variation in surface properties is certainly worthwhile, an alternative approach is to back out heterogeneity characteristics from colloid retention experiments. Incorporation of discrete surface heterogeneity into mechanistic simulation of colloid–surface interaction under unfavorable conditions allows mechanistic simulation of colloid retention under unfavorable conditions.[14–21] This approach, which replaces mean-field DLVO theory with discrete representation of heterogeneity, boils down to identifying the net coverage by attractive versus repulsive surface within the zone of significant colloid-collector interaction (ZOI). The ZOI is restricted to the zone of the closest separation, as the rapid decay of interaction forces with separation distance (driven by colloid curvature) renders interactions outside the ZOI negligible. Duffadar et al.[21] determined that the radius of the ZOI ($R_{ZOI}$) is

$$R_{ZOI} \sim 2\sqrt{\kappa^{-1} a_p} \qquad (2.1)$$

where $\kappa^{-1}$ is the Debye length and $a_p$ the particle radius. Since the net colloid-collector interaction is determined by the combination of attractive and repulsive forces within the ZOI, and the $R_{ZOI}$ is dependent on colloid size, the colloid-collector interaction depends on the interplay of colloid size, heterodomain size, and IS (Figure 2.1). For a given heterodomain size and IS, the net repulsive force (blue = smallest, red = largest repulsion)

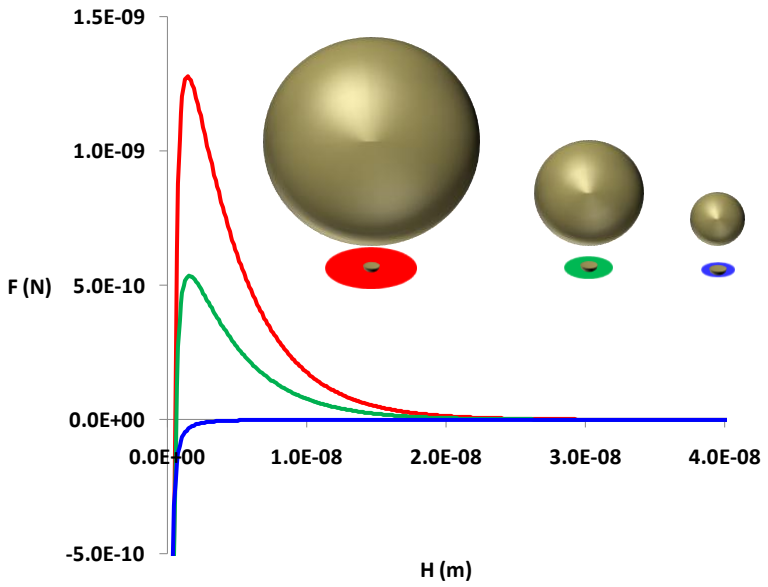


Figure 2.1 Colloidal force profiles. Profiles shown as a function of colloid-collector separation distance (H) for 1.95, 1.1, and 0.25 μm colloids, red, green and blue series, respectively. The projected colored circle represents the ZOI, and the inner circle represents an 80-nm radius heterodomain. The ZOI color corresponds to the force profile. The repulsive force is greatest for the lowest ZOI coverage by heterodomain(s).

is directly related to colloid size since the $R_{ZOI}$ increases with colloid size (blue = smallest, red = largest colloid size), and the fractional coverage (of ZOI) by heterodomains decreases as colloid size (and $R_{ZOI}$) increases relative to a given heterodomain size. This is shown in Figure 2.1 under a condition with 80 nm heterodomains and 6 mM IS, where the ZOIs and the corresponding colloid-collector interaction force profiles as a function of minimum separation distance (H) are shown for the three colloid sizes examined in this study (blue = 0.25 μm, green = 1.1 μm, red = 1.95 μm). Likewise, for a given colloid size and IS, the repulsive force is inversely related to heterodomain size since larger heterodomains occupy greater fractions of the ZOI (red = smallest, blue = largest fractional coverage).

Since the Debye length decreases with increasing IS, $R_{ZOI}$ decreases with

increasing IS (for a given colloid size). Hence, for a given heterodomain and colloid size, repulsion increases with IS (blue = lowest, red = highest IS). The critical outcome is that different-sized colloids "experience" different colloid-surface repulsion for an equivalent surface. Notably, all of the studies cited above that inferred heterogeneity characteristics based on the retention of a population of colloids did so for a single-size population of colloids. Such an approach makes uncertain the likelihood that the inferred surface characteristic is unique since a different sized colloid, or fluid velocity, or IS may require a different surface characteristic to explain the observed colloid retention.

The central hypothesis of this study is that simulation of colloid retention behavior across ranges of colloid size, fluid velocity, and IS allows extraction of representative heterogeneity characteristics of the collector surface. We test this hypothesis on glass slides starting with the simplest representation of heterogeneity (uniformly-spaced and uniformly-sized heterodomains). We show that uniformly sized/spaced heterodomains and normally size-distributed heterodomains are not capable of explaining the array of data. We demonstrate that Pareto-like (power-law) size distributions of heterodomains (sizes ranging from tens to hundreds of nm) are capable of explaining the observed data array.

## Methods

### *Microspheres*

Carboxylate-modified polystyrene microspheres (Molecular Probes, Inc. Eugene, OR) of three sizes (0.25, 1.1, and 1.95 μm in diameter) were used in the experiments. Colloid suspensions were prepared from dilution from the stock in pure water (Milli-Q) to the required concentrations of 1E7, 3.5E6, and 1E6 microspheres per ml the 0.25, 1.1,

and 1.95 μm colloids, respectively. The desired ionic strength (IS) was adjusted by addition of NaCl. The solution was buffered with 2.2 mM MOPS with pH set to 6.72 using NaOH (0.5 M). Colloid electrophoretic mobilities were measured using a ζ–potential analyzer (Zetasizer nano, Malvern Instruments Ltd. Worcestershire, UK). ζ-potentials were calculated from the electrophoretic mobilities via the Smoluchowski equation.[22] ζ-potentials for the 0.25, 1.1, and 1.95 μm colloids were -18.3±1.15, -65.4±2.0, -29.9±0.9 mV (6 mM IS), and -10.5±4.7, -50.1±2.8, -8.2±4.7 mV (20 mM IS), respectively.

*Glass surfaces*

Microscope soda-lime glass slides (Fisher Scientific, Inc) were used as impinging surface in the cell. Glass slides were cleaned via the SC-1 procedure[23] prior to every experiment. Glass-slide ζ-potentials were adopted from representative values reported in the literature,[24] and the corresponding ζ-potentials were -70.0 and -53.5 mV for the 6 and 20 mM IS condition, respectively.

*Impinging jet experiments*

A custom made stainless steel radial stagnation point flow cell was used to observe colloid retention for the range of jet velocities, colloid sizes, and ionic strengths examined. The jet (cell inlet) was 0.50 mm in radius, and the impinging surface was located 1.22 mm perpendicular to the jet axis. To assure evenly radial distribution of the flow across the cell, four outlets were evenly spaced in a circular array at a radial distance 1 cm from the jet center. Experimental conditions were defined as low and high IS (6 and 20 mM) and low and high average jet velocity (1.70 and 5.94 E-3 $ms^{-1}$). Colloid

retention experiments were conducted injecting colloidal suspensions in the flow cell after 30 minutes of equilibration with colloid-free solution. The duration of the experiments ranged from 1 to 6 hours. A minimum of 20 attachments was required to obtain a representative number of colloid deposited per unit time. A total internal reflection microscopy system (Eclipse TE2000-S inverted microscope) (Nikon, Japan) using a Melles Griot IMA 101 Argon laser (Melles Griot Laser Group, Carlsbad, CA) was utilized to illuminate near surface and attached colloids. Images were acquired every 15 seconds via a CCD camera CoolSNAP HQ (Photometrics, Tucson, AZ), and a detailed description of the optical setup is provided in a previous publication.[25] During the experiments a linear slope of deposition versus time was observed, indicating that neither blocking nor ripening occurred during the experiments. An exemplary deposition slope is shown in Appendix A.

*Particle trajectory model*

A previous Lagrangian particle trajectory model[25] was modified to implement the GSI technique (described below) to account for heterodomain contributions to the net colloidal force. The particle trajectory model accounts for the various forces acting on the colloid, including fluid drag, hydrodynamic retardation, gravity, diffusion, virtual mass, and colloidal (DLVO) forces. The electric double layer force calculation was updated to a more general expression (Appendix A) developed by Ling and Wiesner, [26] which is more general and applicable to the ranges of IS and colloid size examined in this study. The force and torque balances used in the model are described in detail in previous publications.[19,25]

*Colloidal force integration techniques*

DLVO-based colloidal force was modified to account for the discrete heterogeneity contributions to colloid-collector interactions adapting the GSI technique developed by Duffadar and Davis[17] as described in Ma et al.[19] The integration of every surface element contribution in GSI demands intensive computational cost. Bendersky and Davis[15] showed that the GSI technique can be simplified by linear approximation (LA) of favorable and unfavorable contributions within the zone of colloid-surface interaction (ZOI), assuming that the influence of the curvature of the colloid within the ZOI is negligible. Calculations of colloid-collector interactions under the range of Debye lengths examined in this study (~2 to 4 nm, corresponding to high and low IS, respectively) demonstrated this assumption to be applicable; equivalent results were obtained for the GSI and LA calculations, as shown in exemplary colloidal force profile distributions (Appendix A). Therefore, in this work, the colloidal force was calculated according to the LA.

*Heterodomains*

For simplicity, heterodomain $\zeta$–potentials were assumed to be of the same magnitude and opposite charge relative to the bulk collector. This simplification is reasonable given that once the fractional coverage of ZOI by heterodomains is sufficient to eliminate the energy barrier to attachment; the energy of attraction, as indicated by collector efficiency, is relatively insensitive to the magnitude of the attractive $\zeta$–potential (Appendix A).

In order to model heterogeneous surfaces, the location of heterodomains needed to be explicitly defined over the collector. The rationale is that the physics of colloid

interaction with heterodomains cannot be represented statistically, as performed in Bradford and Torkzaban.[27] In statistical approaches, the only condition for attachment is net colloid-collector attraction. Since random diffusion of colloids influences the likelihood that attractive interactions with heterodomains will yield attachment over the finite time of attractive interaction, it is a necessary but not sufficient condition for attachment that the colloid-collector interaction be net attractive. This concept is demonstrated in exemplary trajectories in Appendix A. If one assumes attractive colloid-collector interaction equivalent to attachment, then the nondeterministic physics of the transport are absent. Notably, if a statistical representation of heterodomains is used in explicit particle trajectory simulations, the surface is different at each transport step, thereby requiring a larger surface coverage by heterodomains to allow colloid arrest. For example, arrest of a 2-μm particle requires 30% surface coverage by statistically represented 200-nm heterodomains, whereas only 0.02% coverage is needed when both the heterodomains and transport are explicit (data not shown).

To reduce the computational intensity involved in explicit representation of heterodomains, we defined a "unit cell" of heterodomains within a square subdomain ("tile") of the collector surface. This tile was repeated across the whole collector using a fixed regular grid. Heterodomains were defined by the original location relative to the tile and an offset that defines the position of the tile in the fixed grid. A visual representation of this strategy is shown in Appendix A.

*Fluid flow field*

A solution of the three-dimensional fluid flow field of the impinging jet cell was obtained from the Navier-Stokes equations for laminar flow using a finite-element

computational software.[28] The solution was defined by two boundary conditions: laminar inflow corresponding to a given average jet velocity at the inlet ($H_{max}$) and atmospheric pressure at the outflow boundary. The outflow boundary radius (5 mm) was set 5 times larger than the jet radius to represent radial expansion of the flow. A mesh of 352,895 tetrahedral elements was generated to define flow field nodes in the three dimensional domain.

In order to reduce computational intensity in trajectory simulations, the flow field was represented by a continuum expression relating the radial ($v_R$) and normal ($v_N$) fluid velocities as functions of normal ($z$) and radial ($r$) coordinates scaled using the field intensity,[29] $\alpha_f$, and average jet velocity ($v_{jet}$),

$$v_R = v_{jet}\alpha_f \left(\frac{z}{\xi R_{jet}}\right)^2 \tag{2.2}$$

$$v_N = v_{jet}\alpha_f \left(\frac{z}{\xi R_{jet}}\right)\left(\frac{r}{R_{jet}}\right) \tag{2.3}$$

where a z-scaling factor ($\xi$) accounts for the fact that $H_{max}$ in our system is slightly larger than 2x$R_{jet}$. The parameter $\xi$ was calibrated to a value of 0.90 by matching simulated colloid retention with experimental results obtained under favorable conditions under multiple flow regimes (Appendix A). To determine $\alpha_f$, the 3D numerical solution of the flow field was collapsed to a 2D *r-z* plane, and $\alpha_f$ was fit as a logarithmic function of the normalized distance to the impinging plane (z coordinate) as shown in equation 2.4.

$$\alpha_f = \alpha_{f1}\, ln\left(\frac{z}{R_{jet}}\right)^2 + \alpha_{f2} \tag{2.4}$$

where $\alpha_{f1}$ and $\alpha_{f2}$ are fitting coefficients. The best fit was determined by matches to two independent observations of velocity: 1) numerically determined velocities near the forward flow stagnation axis and near the collector surface (fits shown in Appendix A) and 2) experimentally determined near-surface radial velocities of 1.1 and 1.95 μm colloids reentrained in response to ionic strength perturbation.[30] Observed average near surface velocities were 1.47E-6 ± 5.33 E-7 $ms^{-1}$ and 1.14E-7 ±3.57E-7 $ms^{-1}$, for the 1.1 and 1.95 μm colloids, respectively. Best fits by both criteria above yielded simulated average radial velocities of 1.23E-6 ± 7.75 E-7 $ms^{-1}$ and 8.71E-7 ± 8.71E-7 $ms^{-1}$ for the 1.1 and 1.95 μm colloids, respectively.

*Diffusion scaling*

The Brownian force ($F_B$) was represented as a Gaussian white noise random process,[31] using the following expression:

$$F_B = C_B U \sqrt{\frac{12\pi a_p \mu k_B T}{\Delta t}} \qquad (2.5)$$

where $C_B$ is a scaling factor, $U$ is a random number from a Gaussian distribution of zero mean and unit variance, $k_B$ is the Boltzmann constant, $T$ is the absolute temperature, $\mu$ is the viscosity of the fluid, $a_p$ is the particle radius, and $\Delta t$ is the simulated time step. To represent uncorrelated (random) motion, $\Delta t$ should be larger than the characteristic particle momentum relaxation time, $dt_{MRT}$ [32], which is equal to

$$dt_{MRT} = \frac{m_p}{6\pi\mu a_p} \qquad (2.6)$$

where $m_p$ is the mass of the particle. Displacements from an origin were evaluated at different times following release to compare predicted mean displacement ($r_{mean}$) with those from kinetic theory

$$r_{mean} = \sqrt{6D_{ES}t} \quad (2.7)$$

where $D_{ES}$ is the Einstein-Stokes diffusion coefficient[33] and $t$ is time. The diffusion coefficient is equal to

$$D_{ES} = \frac{k_B T}{6\pi\mu a_p} \quad (2.8)$$

Simulations showed that $\Delta t$'s ranging from 10x$dt_{MRT}$ to100x$dt_{MRT}$ produced equivalent average displacements for a population of particles (n = 500) for all sizes (0.25, 1.1, and 1.95 μm colloids). In order to scale average simulated displacement with expected $r_{mean}$ displacements (equation 2.7), the scaling factor, $C_B$, was fitted to 1.35 yielding good agreement (+- 3%) for all colloid sizes examined (comparison shown in Appendix A). In order to optimize computational performance, $\Delta t$ was set to 100x$dt_{MRT}$ for the 0.25 μm colloids and 10x$dt_{MRT}$ for > 0.25 μm colloids in the particle transport simulations.

<u>*Non-DLVO forces*</u>

Steric forces were incorporated into the model by a simple relationship for hydration repulsion[34] (equation 2.9 below), wherein the repulsive steric energy per unit area of interaction ($W(H)$) decays exponentially as a function of separation distance ($H$) and a characteristic decay length ($\lambda_0$):

$$W(H) = W_O e^{-\frac{H}{\lambda_O}} \quad (2.9)$$

where $W_0$ is the maximum repulsive energy per unit area at the closest possible separation distance. Calibration of steric force parameters are provided in Pazmino et al.,[30] and the values of $W_0$ and $\lambda_0$ used here were 0.21 $Jm^{-2}$ and 0.0635 nm, respectively. The combination of repulsive steric force and locally attractive DLVO forces define an equilibrium separation distance (maximum attractive force). At this separation distance, surface friction was incorporated into the force and torque balance via adhesion theory.[35] Attachment was attained when the resisting torque counteracted the driving torque, yielding zero tangential velocity (particle arrest).

*Determination of collector efficiency ($\eta$)*

In experiments, the number of particle deposited at several time intervals, e.g., every 15 seconds, was measured. In the absence of blocking and ripening effects, the number of colloids attached was a linear function of time. This initial slope of deposition (across the area of observation, $A_{obs}$) was used to calculate collector efficiency ($\eta$) via the following equation:

$$\eta = \frac{\left(\frac{\#_{attached}}{time}\right)_{A_{OBS}}}{\left(\frac{\#_{injected}}{time}\right)_{A_{JET}}} = \frac{\frac{\#_{attached}}{time}}{C_O\, Q} \quad (2.10)$$

where $C_O$ is the injected concentration of colloids, and $Q$ is the flow rate of the fluid that enters the cell (across the area of the jet, $A_{jet}$). The product $C_O\, Q$ is equal to the number of particles injected per unit time across $A_{jet}$.

In simulations, colloid injection was performed across a smaller radius ($R_{lim}$) than

$R_{jet}$ for computational efficiency. This approach is based on the fact that beyond a limiting radius from the jet center (forward flow stagnation axis), a colloid has zero chance of reaching near the surface of the collector.[29] An appropriate $R_{lim}$ was found to be that for which $\eta$ was found to be constant despite doubling or halving $R_{lim}$. $R_{lim}$ values were typically several μm for our system.

To determine the simulated $C_o$ that would correspond to injection across $A_{jet}$, the number of colloids injected within $R_{lim}$ was extrapolated to $R_{jet}$, noting that whereas $C_o$ at the jet exit is not a function of $r$, colloid flux toward the surface is a function of $r$ due to fluid velocity ($v_N$) at the jet exit being a function of $r$. Notably, the flow field of interest in this extrapolation is not the idealized version used for small $r$ and z values in the particle trajectory simulations (equations 2.2 and 2.3); rather it is the experimental flow field, which displays a parabolic dependence of $v_N$ on $r$:

$$v_N(r) = v_{Nmax}\left[1 - \left(\frac{r}{R_{jet}}\right)^2\right] \qquad (2.11)$$

where $v_{Nmax}$ is the maximum normal velocity (at $r = 0$), and the average velocity is equal to $v_{jet}$. Hence, the number of colloids injected within $A_{jet}$ was equal to that injected in $A_{lim}$ plus the number hypothetically injected between $A_{lim}$ and $A_{jet}$. For simulations this was calculated from

$$\left(\frac{\#_{injected}}{time}\right)_{A_{JET}} = \left(\frac{\#_{injected}}{time}\right)_{A_{lim}} \frac{A_{jet}v_{jet}}{A_{lim}v_{lim}} \qquad (2.12)$$

where $v_{lim}$ is the average velocity in $A_{lim}$. The radius of the area of observation ($A_{obs}$) in simulations was chosen to circumscribe the same area as the rectangular experiment-based $A_{obs}$ (450 x 336 μm), and the corresponding radius served as the exit point in the

simulations. A detailed schematic of the jet geometry is provided in Appendix A. It should be noted that while $\eta$ is defined consistently between experiments and simulations, direct comparison of these values (impinging jet-based) to colloid filtration theory (Happel sphere-in-cell-based) requires definition of porosity in the impinging jet, which will be described in a forthcoming publication.

*Blocking*

The number of heterodomains occupied by deposited colloids at simulation's end was compared to the total number of heterodomains that existed across $A_{obs}$ to determine whether a large fraction of heterodomains were hypothetically occupied in simulations, which would violate the observed absence of blocking in experiments. For all cases, simulated attachment occupied less than 10% of the available heterodomains, and therefore simulated heterodomain coverage by colloids was consistent with experiments for all conditions described below.

## Results and Discussion

*Experimental results*

Experimentally-observed colloid retention (quantified as $\eta$) on similar glass surfaces varied over one order of magnitude even for experiments examining a single colloid size, and even on glass slides from the same lot (Figure 2.2). Greater variability was observed for the 0.25 and 1.95 μm colloids relative to the 1.1 μm colloids. For the 0.25 μm colloids, optical limitations (limited visibility at the ≤ 20x magnification required for representative field of observation) likely contribute to the enhanced variability for this colloid size. The apparent greater variability for the 1.95 μm relative to

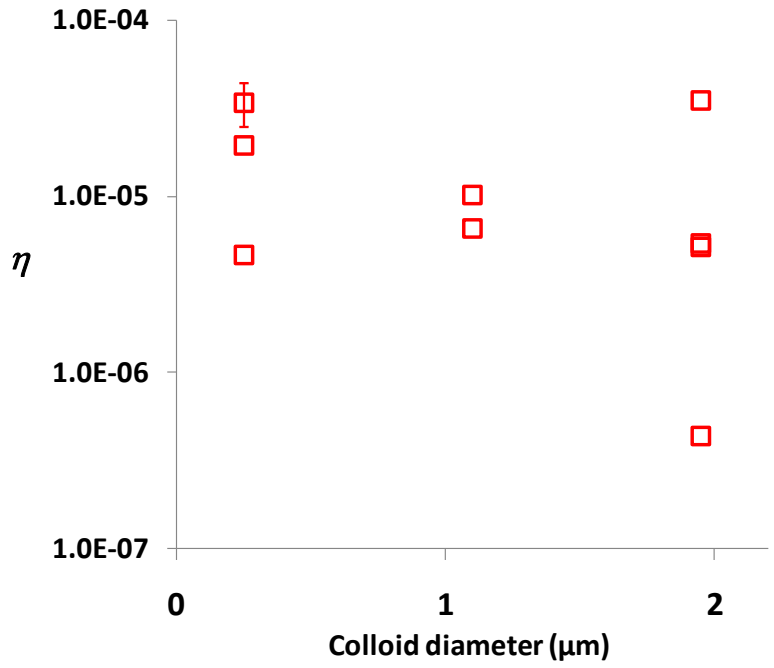


Figure 2.2 Experimental values of colloid retention for different glass slides of a same lot. Average jet velocity = 1.7E-3 $ms^{-1}$, IS = 6 mM. Error bars denote minimum and maximum values for duplicate experiments.

the 1.1 µm colloids may be due to the fact that the injection concentration for the 1.95 µm colloids (~1E6 $ml^{-1}$) was a factor of 3.5 lower relative to the 1.1 µm colloids, yielding lower absolute attachment in the observation area over a 2-hour period (<20 versus >40 colloids attached).

Variation in colloid retention was reduced to within a factor of two by repeated use of a single slide (Figure 2.3) (with cleaning between experiments). Preliminary retention results were examined for 10 slides (A to J). Among these, two representative slides were chosen (slides B and E) to demonstrate that among the glass slides there were generally equivalent trends in retention as a function of colloid size. However, these representative slides also demonstrate notable differences in absolute magnitudes of $\eta$ between slides under particular conditions (Figure 2.3). This result indicates that each

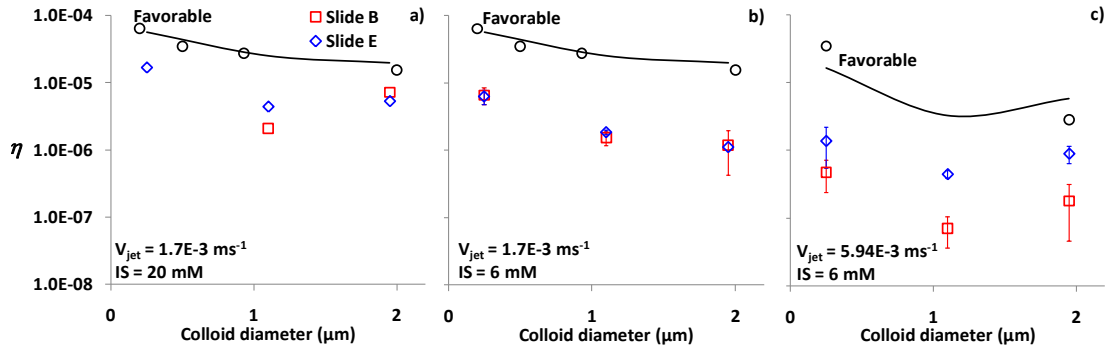


Figure 2.3 Experimental (open symbols) for indicated experimental conditions, average jet velocity (Vjet), and IS. Red squares and blue diamonds series correspond to slides B and E for unfavorable conditions and black circles correspond to favorable conditions for attachment. Black lines correspond to favorable conditions simulations. Error bars denote maximum and minimum values for duplicate experiments.

slide in the lot has similar but unique surface characteristics governing colloid retention.

Colloid retention increased with increased IS, consistent with expected trends based on mean-field DLVO (increased electric double layer repulsion with decreasing IS) (Figure 2.3a and 3b). Consistent results were repeatedly observed following cleaning of the surface, indicating that surface properties were consistent despite repeated cleaning. While retention under a given IS was nearly equivalent on slides B and E under low fluid velocity (Figure 2.3b), retention differed by an order of magnitude between the two slides under high fluid velocity (Figure 2.3c).

Retention showed a characteristic minimum in the colloid size range of 1–2 µm, for all conditions examined, suggesting that diffusion- and settling-enhanced transport to the near-surface controlled retention under unfavorable conditions, as is well known to be the case for favorable conditions (Figure 2.3). However, important differences in the trends do exist, such as the accentuated minimum retention for the 1-µm colloids under unfavorable relative to favorable conditions (Figure 2.3a), which will be discussed further below.

*Simulations*

The simplest representation of heterogeneity corresponds to a single-size heterodomain uniformly distributed across the surface. Heterodomain size (Figure 2.4 top row) and surface coverage (Figure 2.4 bottom row) were varied independently to determine whether simulated retention captured experimental observations using single-sized uniformly distributed heterodomains. Below a certain size threshold, the heterodomain comprises an insufficiently small fraction of the ZOI to produce net attraction. For example, under the conditions examined, a 40-nm (radius) heterodomain captured 0.25, but not 1.1 or 1.95 μm colloids (Figure 2.4a). An 80-nm (radius) heterodomain captured 0.25 and 1.1 μm colloids, but not 1.95 μm colloids (Figure 2.4b). Above a certain size threshold, the heterodomain size exceeded the critical size relative to the ZOI to produce attraction, and retention occurred for all colloid sizes. However, for a given surface coverage by heterodomains, increased heterodomain size reduced the number of heterodomains, yielding a decrease in colloid retention (Figure 2.4a). For example, under the conditions examined, 200 nm heterodomains yielded lower retention than 100 nm heterodomains for a given surface coverage (0.02% in Figure 2.4a).

For a given heterodomain size that captured the retention of all three colloid sizes examined, e.g., 120 nm heterodomains, retention was proportional to surface coverage. Notably, the simulations captured the general decrease in retention with decreased IS (compare Figure 2.4a and 2.4b) and also the general decrease in retention with increased fluid velocity (compare Figure 2.4b and 2.4c). However, important characteristics of the experimentally-observed trends were not preserved, specifically minimum retention corresponding to the range of 1–2 μm colloids.

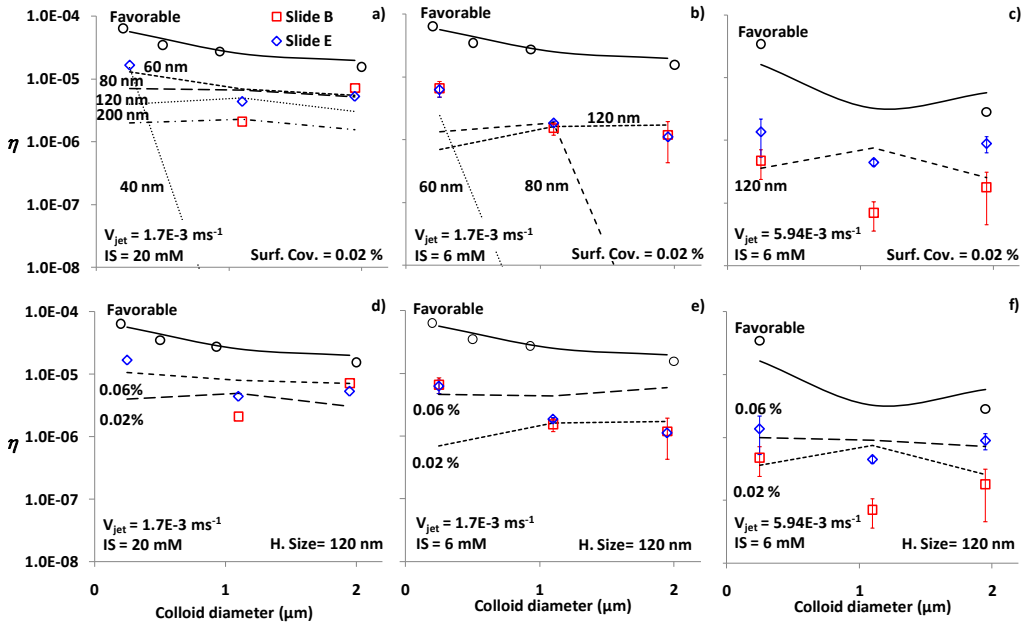


Figure 2.4 Experimental (open symbols) for indicated experimental conditions, average jet velocity (Vjet) and IS, and simulations (lines) for uniform size heterodomains. Red squares and blue diamonds series correspond to slides B and E for unfavorable conditions. Black circles correspond to favorable conditions to attachment. Top row: different heterodomains sizes same surface coverage (0.02%). Bottom row: different surface coverage for the same heterodomain size (120 nm radius). Error bars denote maximum and minimum values for duplicate experiments.

Notably, the simulations using uniformly-sized and -spaced heterodomains did not yield a clear retention minimum corresponding to the 1.1 µm colloids, and in fact, the simulated retention of 1.95 µm colloids was insignificantly greater (and was sometimes even lower) than that of 1.1 µm colloids (Figure 2.4). These simulated trends at first glance seem to violate expectations based on transport-limited delivery of colloids to the near surface (CFT); i.e., interception of the surface should be least for colloids in the 1–2 µm size range since greater diffusion of < 1 µm colloids, and greater settling of > 2 µm colloids should yield a relatively greater interception of the surface. The reason for the "reversed" simulated trend is that the residence times of colloids in the near-surface fluid (the domain in which secondary energy minimum attraction and electric double layer

influence colloid trajectories) vary with colloid size. The average simulated residence time in the near-surface fluid for colloids that reached the near-surface domain was least for the 0.25 μm colloids (15.1 ± 8.3 seconds) and were much greater for the larger colloid sizes (172.5 ±144.3 and 164.3 ± 133.8 seconds for the 1.1 μm and 2.0 μm sizes, respectively). This demonstrates that smaller colloids more readily exited the near-surface domain relative to larger colloids, which is an expectation from Maxwell theory[9, 36] and which resulted in a reduced simulated likelihood of interaction with heterodomains for the 0.25 μm colloids. Note that Maxwell theory does not speak to the fate of the colloids that remain within the secondary energy minimum (whether they attach or remain mobile in the near surface fluid). In contrast, the trajectory simulations with discrete heterogeneity determine mechanistically whether those colloids that remain in the near-surface fluid eventually attach.

The above findings (Figure 2.4) indicate that our experimental array cannot be captured using single-size uniformly-spaced heterodomains. The repeated under-prediction of 0.25 μm colloid retention relative to larger colloid sizes suggests that a distribution of heterodomain sizes that emphasizes smaller-sized heterodomains might preferentially increase the retention of smaller colloids and thereby explain colloid retention across the experimental matrix. Power law size distributions have been observed in numerous natural and engineered systems, including defects ranging from nm to μm in size on various surfaces[37, 38]. Natural colloid size distributions in aquatic and groundwater systems show number-based Pareto size distributions.[39, 40]

In order to represent the collector surface, a simple Pareto type I distribution was developed using only two heterodomains sizes (60 and 120 nm). The minimum

heterodomain size utilized in the distribution (base size) corresponds to the one that captures only the 0.25 μm colloids under all the experimental conditions. In contrast, the maximum heterodomain size corresponds to the smallest heterodomain that captures all colloid sizes (Figure 2.4). The number-based probability density function for Pareto distributions is[41]

$$PDF_{TypeI} = \frac{\gamma}{(X_n)^{1+\gamma}} \tag{2.13}$$

where $\gamma$ is the Pareto index parameter, and $X_n$ is any heterodomain normalized to the base size.

It is important to note that whereas only two heterodomain sizes were examined for the Pareto type I distribution, it is possible that the heterodomain size distribution continues to smaller sizes on the glass slide. While these smaller heterodomains would be unable to influence the retention of colloids reported here (e.g., Figure 2.4), additional experiments and simulations with smaller nanoparticles may reveal their existence. For simplicity, we restrict the simulations to the heterodomain size range necessary to explain observed retention of colloids.

Particle retention simulations for two $\gamma$ values (1 and 2), which correspond to surfaces with 1:4 and 1:8 number ratios for the 120 relative to 60 nm heterodomains, are shown in Figure 2.5. Notably, the simulated trend yields a reasonable match to experiments across all conditions examined. The larger ratio of small to large heterodomains (1:4) required a lesser surface coverage (0.04%) to achieve a similar fit as the larger ratio (1:8) at a greater surface coverage (0.06%) (Figure 2.5). This indicates that the number of large heterodomains was a limiting factor on the fit, whereas retention

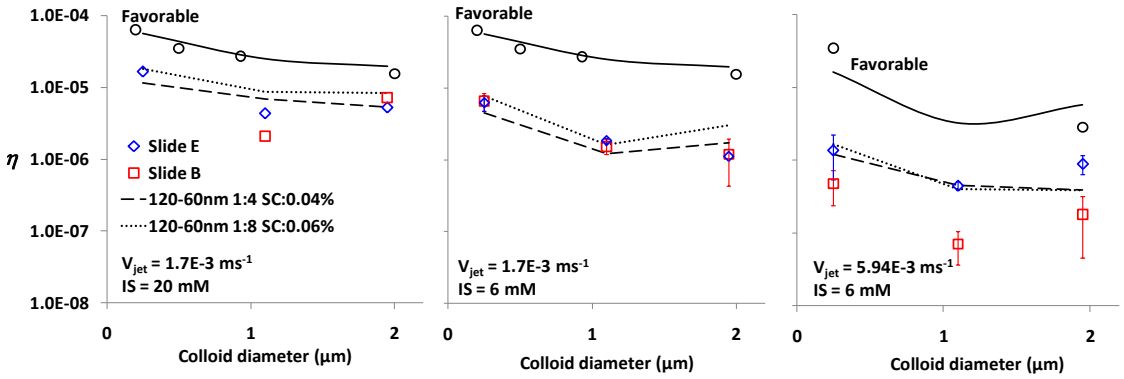


Figure 2.5 Experimental and simulated retention for Pareto distribution of heterodomains. Experimental (open symbols) for indicated experimental conditions, average jet velocity (Vjet) and IS, and simulations (lines) for two types of Pareto size-distributed heterodomains at indicated surface coverage. Dashed lines corresponds to 1:4 number ratio 120 to 60 nm heterodomains 0.04 surface coverage (SC), and dotted lines corresponds to 1:8 number ratio of 120 to 60 nm 0.04% surface coverage (SC). Red squares and blue diamonds series correspond to slides B and E for unfavorable conditions, and black circles correspond to favorable conditions.

of smaller colloids on the "excess" small heterodomains in the latter case was likely limited by the limited availability of near-surface small colloids (e.g., Figure 2.4 and corresponding description). Because the $\zeta$ of the 1.1 μm colloids was much more negative (-65.4 mV) relative to the other-sized colloids, we checked the sensitivity of our results to $\eta$ via comparison to simulations for the 1.1 μm colloids using a value of $\zeta$ (-24.1 mV) that was intermediate to those of the 0.25 and 1.95 μm colloids (-18.3 and -29.9 mV, respectively, at 6 mM IS). It was found that $\eta$ increased only 50% in response to this nearly factor of 3 reduction in $\zeta$ for the 1.1 μm colloids (Appendix A). The match of the simulated to experimental values was preserved, thereby demonstrating that sensitivity of $\eta$ is primarily driven by the size and spatial frequency of heterodomains and is much less sensitive to $\zeta$ of the colloid (demonstrated here) or oppositely-charged heterodomains (demonstrated in Appendix A). Overall, the results indicate that a Pareto-

distribution of heterodomain sizes provide a reasonable representation of heterogeneity on the collector surface.

Notably, the trajectory model with discrete heterogeneity did not capture the divergent retention behaviors observed between slides B and E under the higher fluid velocity condition (Figure 2.5). This likely indicates that other processes in addition to charge heterogeneity contribute to the observed retention under unfavorable conditions. Since heterodomains are represented solely in terms of surface charge in the GSI-LA approach, it is possible that roughness is another characteristic that may distinguish slides B and E, but that is not explicitly represented in the GSI-LA approach. Surface roughness of glass slides is expected to be small (rms roughness in the range of 4 nm[42]) but may potentially play a role in retention, according to simulations by Bendersky and Davis.[16]

Whereas the roughness of slides B and E would be expected to be equivalent, we cannot rule out differences in surface roughness as an explanation for the divergent behaviors of these slides. Likewise, it is also possible surface charge heterogeneities differ between the slides in some unknown way that manifests only at higher fluid velocity in the range of conditions examined here.

Whereas the trajectory simulations with discrete heterogeneity did not capture the divergence of slides B and E under high fluid velocity, they did reasonably capture the bulk of the colloid retention data on the soda lime glass surfaces for a range of colloid sizes, fluid velocities, and ionic strengths. A notable insight from the simulations is that the characteristic minimum retention for 1–2 μm sized colloids exists for different reasons under favorable versus unfavorable conditions.

Under favorable conditions, the minimum results strictly from transport

limitations in the 1–2 μm size range, i.e., lesser diffusion across streamlines relative to smaller colloids and lesser settling across streamlines relative to larger colloids. In contrast, under unfavorable conditions, while transport limitations still exist, the retention of the smallest colloids is mediated by their spending relatively less time in the near-surface fluid domain (discussed above) as well as a relative excess of smaller heterodomains on the collector surface, that is, a power-law or Pareto size distribution favoring smaller-sized heterodomains.

The range in heterodomain radii (120 to 60 nm) inferred from our array of experiments initially appears much larger than those examined by Duffadar et al.[21] (5 nm), who demonstrated that randomly placed 5-nm radius heterodomains (21% surface coverage) successfully simulated deposition rates of three colloid sizes (0.46, 1 and 2 μm) at high IS (90 mM) on silica surfaces coated with cationic polymer poly(dimethylaminoethylmethacrylate) (pDMAEMA). While we would not expect correspondence between heterodomain sizes inferred for bare silica (our study) versus pDMAEMA-coated silica (Duffadar et al.[21]), it is worth noting that clusters of 5 nm heterodomains produced by random (nonoverlapping) placement is responsible for colloid retention in the simulations of Duffadar et al.[21] For simulations at 90 mM IS, under which the ZOIs would be relatively small (equation 1), the necessary cluster size would be relatively modest. In contrast, under 6 mM IS ($\kappa^{-1}$ = 3.97 nm, contrasting to $\kappa^{-1}$ ~1 nm at 90 mM), the ZOIs would be approximately a factor of two larger, and simulations for our system show that random (nonoverlapping) placement of heterodomains (5 nm radius) cannot explain our experimental results (Figure 2.6). A surface coverage of 45% yielded simulated attachment of 1.1 μm colloids, but yielded no

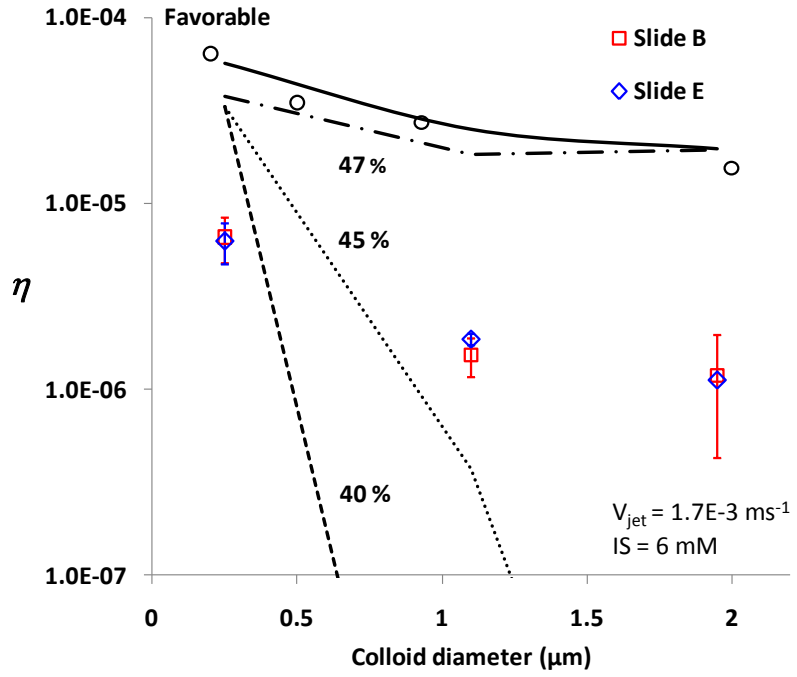


Figure 2.6 Colloid retention results for experiments (open symbols) and simulations: favorable conditions (solid lines), unfavorable simulation results (dashed lines) for randomly located 5-nm radius heterodomains.

simulated attachment of 1.95 µm colloids (Figure 2.6) while greatly over-predicting the attachment of 0.25 µm colloids (matching favorable conditions). A surface coverage of 47% yielded colloid retention equivalent to favorable conditions for all colloid sizes simulated (Figure 2.6). Therefore, randomly-placed 5 nm heterodomains did not yield the range of cluster sizes needed to explain our experimental results on bare silica, which instead required a Pareto type arrangement of heterodomains at low surface coverage (0.04%) that was uniform and sparse (Figure 2.7 top). In contrast, the pDMAEMA-coated silica of Duffadar et al.[21] was well simulated by ~25% coverage by 5 nm heterodomains for their 90 mM condition, which is represented in a scaled schematic with ZOIs for the colloids examined in our study at 6 mM IS (Figure 2.7 bottom).

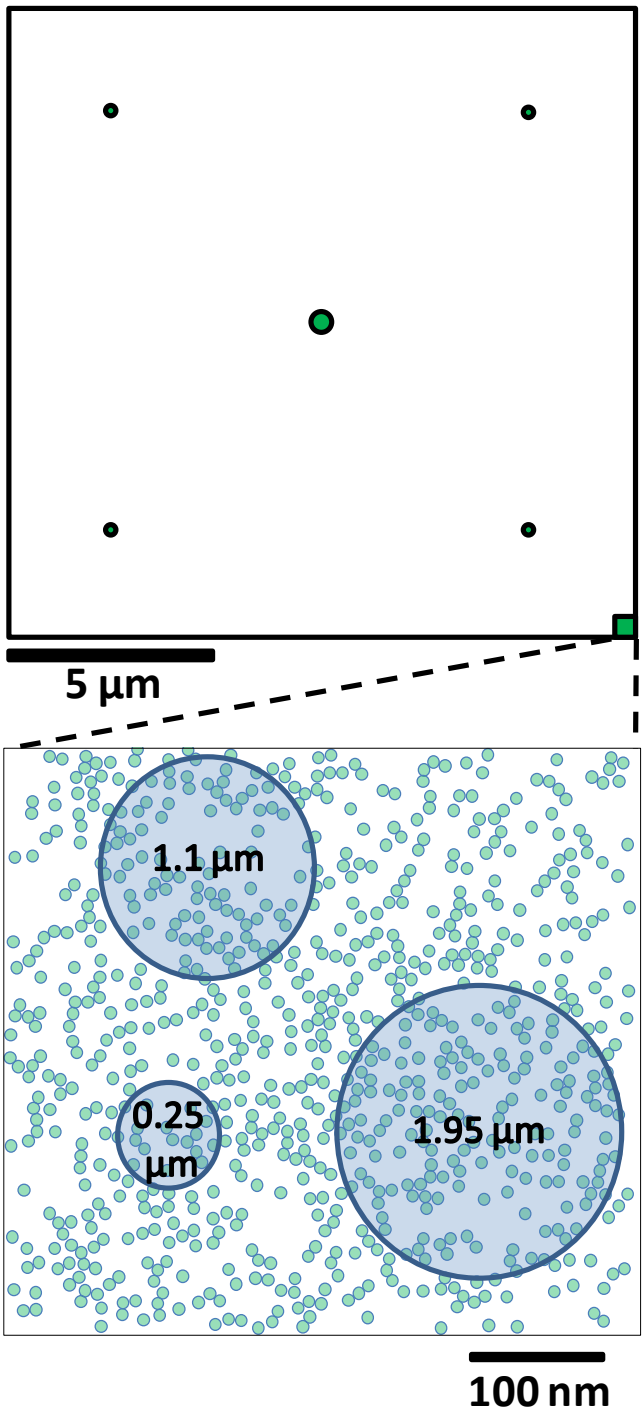


Figure 2.7 Power-law size distributed and random placed heterodomains tiles. Top: 120 and 60 nm-radius heterodomains 1:4 in number, at 0.04% surface coverage (heterodomain size exaggerated for visibility). Bottom: random placement of 5-nm radius heterodomains (at scale) at 25% surface coverage. The blue circles represent the zone of influence (ZOI) corresponding of 0.25, 1.1 and 1.95 µm colloids at 6 mM IS. The green corner at the lower right of the top tile represents (scales) the corresponding size of the bottom tile.

Notably, random placement of larger primary heterodomains would also fail to match observed trends since larger heterodomains require lower surface coverages to yield the observed retention. For example, observed attachment required > 45% surface coverage for 5 nm heterodomains (Figure 2.6), and 0.02% surface coverage for 120 nm heterodomains (Figure 2.4). The relatively low number of random heterodomain placements associated with large heterodomains at low surface coverage would yield negligible clustering, thereby approximating uniform placement. Hence, random placement of small (5 nm) heterodomains at high surface coverage maximizes the probability of developing the large range of cluster sizes necessary to explain the observed retention. The inability of random heterodomain placement to match observations under conditions that maximizes the range of heterodomain cluster sizes demonstrates that random placement is unable to explain the observed retention under larger heterodomain size conditions.

The realization that power-law-distributed heterodomain sizes are necessary to match observed colloid retention demonstrates that ranges in IS (and fluid velocity) and colloid size are necessary to infer representative heterogeneity characteristics of the collector surfaces.

That different soda-lime glass slides showed different amounts of colloid retention under equivalent conditions might be considered a cause for concern in the effort to predict colloid transport at larger scales. Balancing that concern is our anticipation that the range of colloid retention among glass surfaces will be distinct relative to other surfaces For subsurface transport, such other surfaces include micas, feldspars, carbonates, etc. A subsequent goal is to characterize such surfaces in terms of

experiment-based colloid retention and trajectory-based simulations with discrete heterogeneity in order to determine whether these surfaces show distinct retention ranges relative to each other and to glass. Such work will determine whether representing retention via discrete heterogeneity yields a distinct but logical set of heterodomain representations among mineral surfaces predominant in groundwater aquifers.

## Summary

In this work we demonstrated that experimentally-observed colloid retention under unfavorable conditions across a range of colloid sizes, fluid velocities, and IS was mechanistically simulated via inclusion of discrete surface charge heterogeneity in particle trajectory models. We determined that randomly placed heterodomains are insufficient to explain observed retention while power-law size distribution of heterodomains was able to quantitatively describe the observed retention over soda-lime glass slides. This approach may serve as a platform to extract representative heterogeneity responsible for colloid retention under unfavorable conditions on other aquifer-relevant minerals.

## References

(1) Rajagopalan, R.; Tien, C. Trajectory Analysis of Deep-bed Filtration with the Sphere-in-cell Porous Media Model. *AIChE J.* **1976,** *22* (3), 523–533.

(2) Tufenkji, N.; Elimelech, M. Correlation Equation for Predicting Single-collector Efficiency in Physicochemical Filtration in Saturated Porous Media. *Environ. Sci. Technol.* **2004,** *38* (2), 529–536.

(3) Nelson, K. E.; Ginn, T. R. New Collector Efficiency Equation for Colloid Filtration in both Natural and Engineered Flow Conditions. *Water Resour. Res.* **2011,** *47* (5), W05543.

(4) Long, W.; Hilpert, M. A Correlation for the Collector Efficiency of Brownian Particles in Clean-bed Filtration in Sphere Packings by a Lattice-Boltzmann Method. *Environ. Sci. Technol.* **2009,** *43* (12), 4419–4424.

(5) Ma, H.; Hradisky, M.; Johnson, W. P. Extending Applicability of Correlation Equations to Predict Colloidal Retention in Porous Media at Low Fluid Velocity. *Environ. Sci. Technol.* **2013,** *47* (5), 2272–2278.

(6) Elimelech, M.; O'Melia, C. R. Kinetics of Deposition of Colloidal Particles in Porous Media. *Environ. Sci. Technol.* **1990,** *24* (10), 1528–1536.

(7) Vaidyanathan, R.; Tien, C. Hydrosol Deposition in Granular Beds: An Experimental Study. *Am. Inst. Chem. Eng., [Spring Natl. Meet.]* **1988**, *81*, 122–144.

(8) Song, L.; Johnson, P. R.; Elimelech, M. Kinetics of Colloid Deposition onto Heterogeneously Charged Surfaces in Porous Media. *Environ. Sci. Technol.* **1994,** *28* (6), 1164–1164.

(9) Shen, C.; Li, B.; Huang, Y.; Jin, Y. Kinetics of Coupled Primary- and Secondary-minimum Deposition of Colloids under Unfavorable Chemical Conditions. *Environ. Sci. Technol.* **2007,** *41* (20), 6976–6982.

(10) Johnson, W. P.; Li, X.; Assemi, S. Deposition and Reentrainment Dynamics of Microbes and Non-biological Colloids during Non-perturbed Transport in Porous Media in the Presence of an Energy Barrier to Deposition. *Adv. Water Resour.* **2007,** *30* (6-7), 1432–1454.

(11) Shellenberger, K.; Logan, B. E. Effect of Molecular Scale Roughness of Glass Beads on Colloidal and Bacterial Deposition. *Environ. Sci. Technol.* **2002,** *36* (2), 184–189.

(12) Taboada-Serrano, P.; Vithayaveroj, V.; Yiacoumi, S.; Tsouris, C. Surface Charge Heterogeneities Measured by Atomic Force Microscopy. *Environ. Sci. Technol.* **2005,** *39* (17), 6352–6360.

(13) Drelich, J.; Wang, Y. U., Charge heterogeneity of surfaces: Mapping and Effects on Surface Forces. *Adv. Colloid Interface Sci.* **2011,** *165* (2), 91–101.

(14) Bhattacharjee, S.; Chun-Han, K.; Elimelech, M. DLVO Interaction Between Rough Surfaces. *Langmuir* **1998,** *14* (12), 3365–75.

(15) Hoek, E. M. V.; Agarwal, G. K. Extended DLVO Interactions between Spherical Particles and Rough Surfaces. *J. Colloid Interface Sci.* **2006,** *298* (1), 50–58.

(16) Bendersky, M.; Davis, J. M. DLVO Interaction of Colloidal Particles with

Topographically and Chemically Heterogeneous Surfaces. *J. Colloid Interface Sci.* **2011,** *353* (1), 87–97.

(17) Duffadar, R. D.; Davis, J. M. Interaction of Micrometer-scale Particles with Nanotextured Surfaces in Shear Flow. *J. Colloid Interface Sci.* **2007,** *308* (1), 20–29.

(18) Duffadar, R. D.; Davis, J. M. Dynamic Adhesion Behavior of Micrometer-scale Particles Flowing over Patchy Surfaces with Nanoscale Electrostatic Heterogeneity. *J. Colloid Interface Sci.* **2008,** *326* (1), 18–27.

(19) Ma, H.; Pazmino, E.; Johnson, W. P. Surface Heterogeneity on Hemispheres-in-cell Model Yields all Experimentally-observed Non-straining Colloid Retention Mechanisms in Porous Media in the Presence of Energy Barriers. *Langmuir* **2011,** *27* (24), 14982–14994.

(20) Shen, C.; Lazouskaya, V.; Zhang, H.; Li, B.; Jin, Y.; Huang, Y. Influence of Surface Chemical Heterogeneity on Attachment and Detachment of Microparticles. *Colloids Surf., A* **2013,** *433*, 14–29.

(21) Duffadar, R.; Kalasin, S.; Davis, J. M.; Santore, M. M. The Impact of Nanoscale Chemical Features on Micron-scale Adhesion: Crossover from Heterogeneity-dominated to Mean-field Behavior. *J. Colloid Interface Sci.* **2009,** *337* (2), 396–407.

(22) Ohshima, H. Electrophoresis of Soft Particles. *Adv. Colloid Interface Sci.* **1995,** *62* (2–3), 189–235.

(23) Kern, W. Cleaning Solutions based on Hydrogen Peroxide for use in Silicon Semiconductor Technology. *RCA Rev.* **1970,** *31*, 187–206.

(24) Kirby, B. J.; Hasselbrink, E. F. Zeta Potential of Microfluidic Substrates: 1. Theory, Experimental Techniques, and Effects on Separations. *Electrophoresis* **2004,** *25* (2), 187–202.

(25) Johnson, W. P.; Tong, M. Observed and Simulated Fluid Drag Effects on Colloid Deposition in the Presence of an Energy Barrier in an Impinging Jet System. *Environ. Sci. Technol.* **2006,** *40* (16), 5015–5021.

(26) Lin, S.; Wiesner, M. R. Paradox of Stability of Nanoparticles at Very Low Ionic Strength. *Langmuir* **2012,** *28* (30), 11032–11041.

(27) Bradford, S. A.; Torkzaban, S. Colloid Adhesive Parameters for Chemically Heterogeneous Porous Media. *Langmuir* **2012,** *28* (38), 13643–13651.

(28) COMSOL Multiphysics™, http://www.comsol.com.

(29) Yang, C.; Dabros, T.; Li, D.; Czarnecki, J.; Masliyah, J. H. Kinetics of Particle Transport to a Solid Surface from an Impinging Jet under Surface and External Force Fields. *J. Colloid Interface Sci.* **1998,** *208* (1), 226–226.

(30) Pazmino, E.; Trauscht, J.; Johnson, W. P., Release of Colloids from Primary Minimum Contact under Unfavorable Conditions by Perturbations in Ionic Strength and Flow Rate. *Environ. Sci. Technol.* **2014,** *48*, (16), 9227–9235.

(31) Li, A.; Ahmadi, G. Dispersion and Deposition of Spherical Particles from Point Sources in a Turbulent Channel Flow. *Aerosol Sci. Technol.* **1992,** *16* (4), 209-226.

(32) Li, T.; Raizen, M. G. Brownian Motion at Short Time Scales. *Ann. der Physik* **2013,** *525* (4), 281–295.

(33) Einstein, A. Investigation on the Theory of the Brownian Movement. *Ann. der Physik* **1905**, *17*, 549–560.

(34) Israelachvili, J. N., *Intermolecular and Surface Forces: Revised Third Edition*. Elsevier Science: Atlanta, 2011.

(35) Johnson, K. L.; Kendall, K.; Roberts, A. D. Surface Energy and the Contact of Elastic Solids. *Proc. R. Soc. London, Ser. A* **1971,** *324*, 301–313.

(36) Franchi, A.; O'Melia, C. R. Effects of Natural Organic Matter and Solution Chemistry on the Deposition and Reentrainment of Colloids in Porous Media. *Environ. Sci. Technol.* **2003,** *37* (6), 1122–1129.

(37) Shi, G.; Atkinson, H. V.; Sellars, C. M.; Anderson, C. W. Application of the Generalized Pareto Distribution to the Estimation of the Size of the Maximum Inclusion in Clean Steels. *Acta Mater.* **1999,** *47* (5), 1455–1468.

(38) Harlow, D. G.; Wei, R. P. A Probability Model for the Growth of Corrosion Pits in Aluminum Alloys Induced by Constituent Particles. *Eng. Fract. Mech.* **1998,** *59* (3), 305–325.

(39) Buffle, J.; Leppard, G. Characterization of Aquatic Colloids and Macromolecules. 1. Structure and Behavior of Colloidal Material. *Environ. Sci. Technol.* **1995,** *29* (9), 2169–2175.

(40) Atteia, O.; Kozel, R. Particle Size Distributions in Waters from a Karstic Aquifer: from Particles to Colloids. *J. Hydrol.* **1997,** *201* (1), 102–119.

(41) Arnold, B. Pareto and Generalized Pareto Distributions. In *Modeling Income Distributions and Lorenz Curves*, Chotikapanich, D., Ed.; Springer: New York 2008; Vol. 5, pp 119–145.

(42) Ren, J.; Ganapathysubramanian, B.; Sundararajan, S. Experimental Analysis of the Surface Roughness Evolution of Etched Glass for Micro/Nanofluidic Devices. *J. Micromech. Microeng.* **2011,** *21* (2), 025012.

# CHAPTER 3

# PERTURBED RELEASE OF COLLOIDS FROM PRIMARY ENERGY MINIMUM CONTACT WITH HETEROGENEOUS SURFACES


## Abstract

Colloid release from surfaces in response to ionic strength and flow perturbations has been mechanistically simulated. However, these models do not address the mechanism by which colloid attachment occurs, at least in the presence of bulk colloid-collector repulsion (unfavorable conditions), which is a prevalent environmental condition. We test whether a mechanistic model that predicts colloid attachment under unfavorable conditions also predicts colloid release in response to reduced ionic strength (IS) and increased fluid velocity (conditions thought prevalent for mobilization of environmental colloids). The model trades in mean-field colloid-collector interaction for discrete representation of surface heterogeneity, which accounts for a combination of attractive and repulsive interactions simultaneously, and results in an attached colloid population (in primary minimum contact with the surface) having a distribution of strengths of attraction. The model moderates equilibrium separation distance by inclusion of steric interactions. Using the same model parameters to quantitatively predict attachment under unfavorable conditions, simulated release of colloids (for all three sizes) from primary minimum attachment in response to perturbations qualitatively

matched experimental results, demonstrating that both attachment and detachment were mechanistically simulated.

## Introduction

Waterborne disease outbreaks have been associated with heavy rainfall events, [1–3] suggesting that infiltration of fresh water into the subsurface may help to drive mobilization of pathogens.[4, 5] During rainfall events, the aquifer is perturbed not only by increased flow and transients in saturation,[6,7] but also by reduced ionic strength (IS). A major effect of reduced IS is increased repulsion between colloids and collectors. Both increased repulsion and increased fluid velocity may therefore promote mobilization of retained pathogens and other colloidal materials. Whereas increased fluid velocity and reduced IS are conceptually linked to colloid mobilization, the specific mechanisms that link them are debated. To date no mechanistic model predicts colloid attachment in the presence of bulk colloid-collector repulsion (unfavorable conditions) while also predicting colloid release in response to reduced ionic strength or increased fluid velocity. Notably, the term "attachment" is herein used to refer to immobilization (primary minimum association), as opposed to the broader term "retention," which may also include colloids that are not immobilized,[8, 9] but which are associated with the collector surface via secondary minimum interactions.

The primary and secondary minima arise from the theory describing colloid-surface interactions (DLVO theory, so called for the four authors by whom it was developed[10, 11]) as classically composed of van der Waals and electric double layer interactions. In this classic approach, if both interactions are attractive, there is no barrier to attachment, and colloids that approach close to the surface are attached, immobilized

in the primary minimum, where van der Waals attraction holds the colloid to the surface, e.g., at separation distances less than 0.5 nm. However, under conditions prevalent in the environment, the electric double layer (EDL) interaction is repulsive, yielding a barrier to attachment (so called unfavorable conditions). These features are shown for the corresponding force profiles (Figure 3.1). The magnitude of the barrier is dependent on colloid and collector surface properties such as charge, as well as solution IS and pH. Because the van der Waals interaction extends to greater distances from the surface relative to EDL repulsion, a zone of weak attraction (the secondary minimum) may exist beyond the barrier (10–100 nm separation distance), as shown in the corresponding force profiles (Figure 3.1 inset).

According to the above classic approach, a particle can only become attached (in primary minimum contact) if it has sufficient energy (e.g., by virtue of fluid drag, diffusion, and gravity) to overcome the repulsive barrier. Likewise, a particle attached in the primary minimum must overcome the barrier that exists between this well and the bulk fluid in order to be detached. Notably, the classic DLVO approach predicts large repulsive barriers that prevent attachment according to mechanistic models.[12] Likewise, for colloids that are assumed already attached, classic DLVO theory predicts no detachment in response to reduced IS since IS reduction does not significantly reduce the difference between the barrier maximum and primary minimum, as shown for the corresponding forces (Figure 3.1). In contrast, the secondary minimum depth, and proximity to the surface, is directly related to IS due to the dependence of the EDL interaction on IS. For the specific conditions corresponding to Figure 3.1, a change in IS from 20 to 6 mM displaces the secondary minimum outward and decreases the attractive

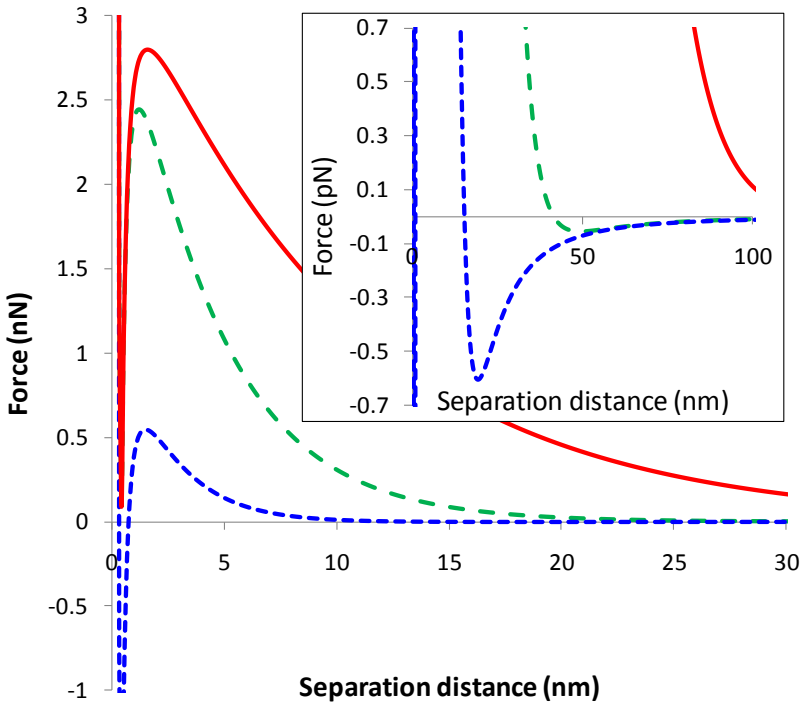


Figure 3.1 Force profiles for 1.95 µm colloids over a repulsive surface at pH = 6.72 for 1, 6, and 20 mM IS. Collector ζ-potential: 94.5, 70.0, and 53.5 mV; Colloid ζ-potential: 37.7, 29.9, and 8.2 mV, respectively. Force units pN = picoNewtons, nN = nanoNewtons. Separation distance units nm = nanometers.

forces by a factor of 10. Further reduction of IS to 1 mM eliminates the secondary minimum under these conditions.

Because classic DLVO theory predicts that the secondary minimum is eliminated with reduced IS, the reentrainment of retained colloids with reduced IS has been interpreted to represent release of colloids that were retained in secondary minima,[13, 14] and this approach has been adopted by multiple groups.[15–17] It must be noted that because secondary minimum forces are relatively weak and distant from the surface (tens to hundreds of nm), they are referred as noncontact forces,[18] and are not expected to immobilize colloids, except in the case where one extends surface friction (contact forces) to the secondary minimum.[19]

Experiments examining colloid retention in packed porous media columns cannot directly distinguish retention mechanisms, i.e., attachment/immobilization (primary minimum contact) versus retention without attachment in secondary minima. In contrast, experiments involving direct observation of colloid retention on flat surfaces with fluid shear (e.g. impinging jet experiments) specifically focus on immobilized colloids while also demonstrating translation of secondary minimum-associated colloids across the observation area.[20]

As noted above, mechanistic simulations using classic DLVO theory do not predict immobilization of colloids on surfaces under unfavorable conditions. This failure arises from use of a mean-field DLVO approach to describe surfaces. Specifically, the properties of the surfaces are assumed to be spatially homogeneous. More recently, replacement of mean-field representation of surfaces with discrete heterodomains representing nanoscale areas of colloid-surface attraction[21–25] successfully simulated the extent and mode of attachment (immobilization) of colloids in the presence of repulsive barriers. Specifically, the attachment to glass surfaces of colloids ranging in size from 0.25 to 1.95 μm under varied IS and fluid velocity conditions was mechanistically simulated under the condition that discrete heterogeneity was represented by Pareto power-law size-distributed heterodomains (nanoscale zones of attractive charge) at a total surface coverage of 0.04 %.[25] The Pareto power-law size distribution was approximated with two heterodomain sizes, radii of 120 and 60 nm, at a number frequency ratio of 1:4, respectively. Calibration of the heterogeneity characteristics of the glass surfaces, i.e., heterodomain size and surface coverage, was performed via comparison of simulations to experimentally-observed colloid retention as a function of colloid size, fluid velocity, and

IS, as described in Pazmino et al.[25]

As noted above, classic mean field DLVO theory does not predict the detachment of primary minimum-associated colloids in response to IS reduction. Previous studies using classic mean field DLVO theory explained colloid release from the primary minimum in response to IS perturbations in terms of reduction of colloid-surface attraction by means other than discrete heterogeneity. For example, Ryan and Gschwend[26] observed a 30% and 400% increase in clay colloid release rates from iron oxide-coated aquifer sand in response to IS reduction from 20 to 0.1 mM and in response to increased pH beyond the $pH_{zpc}$ of goethite, respectively. In order to explain the observed response to the imposed perturbations, i.e., to obtain a colloid-surface attractive force via DLVO interactions that could be overcome by the fluid drag (driven by imposed groundwater velocity) in the experiments, the authors modified the classic DLVO approach by shifting the minimum colloid-collector separation distance outboard to 0.7 nm, from the expected minimum equilibrium separation distance of 0.157 nm.[27] This shift was achieved by increasing the Born repulsion parameter in the DLVO calculations from 0.5 to 20 Å,[28] which eliminated the barrier to detachment when conditions corresponded to the perturbed state. In another study, Bergendahl and Grasso[29] observed release (~60%) of carboxylate-modified polystyrene latex 1-μm microspheres from packed glass beads in response to increased fluid velocity (factor 15). In order to explain the observed release from primary minima using a torque balance, the authors needed to reduce the resisting torque by reducing surface friction, which was performed using a hysteresis loss factor[30] $\beta = 1.77 \times 10^{-3}$ to represent adhesion energy loss via dissipation during rolling. Effectively, the resisting torque holding the colloids to the surface was reduced by a

factor of 0.00177 to reconcile torque balance prediction to observed release. It should be noted that both of the strategies employed by Ryan and Gschwend[26] and Bergendahl and Grasso[29] focus on the detachment of already-attached colloids and that neither strategy addresses the mechanism of colloid attachment prior to detachment.

A notable feature of the discrete heterogeneity approach to predict colloid attachment under unfavorable conditions is that individual colloids within the population of colloids immobilized on the heterogeneous surface may experience varying magnitudes of net attraction depending on the fractional coverage of heterodomains within the effective zone of colloid-surface interaction[25] (ZOI). The net colloid-collector interaction is determined by the combination of attractive and repulsive forces within the ZOI (prevalence of bulk repulsive surface versus attractive heterodomains within the ZOI). Since the radius of the ZOI directly depends on colloid size, and depends inversely on IS, the net colloid-collector interaction depends on the interplay of colloid size, heterodomain size, and IS. Colloid attachment occurs when net attraction is sufficient to arrest the colloid,[25] corresponding to a given threshold coverage of the ZOI by attractive heterodomains. Since coverage of ZOI by heterodomain(s) varies according to nondeterministic interception of heterodomains by the colloid trajectory, attachment will correspond to a variety of ZOI coverages by heterodomains (above the threshold). An attached population therefore experiences a distribution of strengths of adhesion and therefore may display partial mobilization in response to increased fluid velocity, and/or decreased IS. While a variety of strengths of attraction can be expected to result from the above approach, it is an open question whether simulated perturbations (ionic strength or flow) using this approach can also simulate the observed fractional release of colloids

that occurs in response to perturbation.

The goal of this study is therefore to determine whether observed reentrainment of colloids from surfaces in response to flow and IS perturbations are simulated using the same parameters to predict attachment on heterodomains, which would provide a mechanistic approach to explain both observed attachment under unfavorable conditions and observed release in response to perturbations.

## Materials and Methods

### *Microspheres*

Carboxylate-modified polystyrene microspheres (Molecular Probes, Inc. Eugene, OR) of three sizes (0.25, 1.1, and 1.95 μm in diameter) were used in the experiments. Microsphere suspensions were $1x10^7$, $3.5x10^6$, and $1x10^6$ microspheres per ml for the 0.25, 1.1, and 1.95 μm colloids, respectively. Decreasing concentration with colloid size was used in order to maintain dilute suspensions, e.g., <20 ppm for all sizes, and mitigate aggregation and/or conditions of blocking on the collector surface. The suspensions were prepared by dilution from microspheres stocks in pure water (Milli-Q). The desired ionic strength (IS) was adjusted by addition of NaCl, and the solution was buffered with 2.2 mM 3-(N-morpholino)propanesulfonic acid (MOPS). The initial solution pH (4.6) was raised to a final value of 6.72 using NaOH 0.5 M. Microspheres electrophoretic mobilities were measured using a Zetasizer analyzer (Zetasizer nano, Malvern Instruments Ltd. Worcestershire, UK). ζ potentials were calculated from the electrophoretic mobilities via the Smoluchowski equation.[31] ζ potentials for the 0.25, 1.1, and 1.95 μm colloids were -10.5, -50.1, and -8.2 mV (20 mM IS); -18.3, -65.4, and -29.9 mV (6 mM IS); and -61.2, -82.0, and -37.7 mV (1 mM IS), respectively.

*Impinging jet system*

A radial stagnation point flow cell was used to conduct colloid retention experiments. The jet diameter was 1.0 mm (i.d) and was located 1.22 mm from the impinging surface. Four outlets (0.5 mm i.d.) were evenly spaced at a distance of 12.5 mm from the jet center. Details of the experimental setup are provided in Pazmino et al.[25] A total internal reflection microscopy system (Eclipse TE2000-S inverted microscope) (Nikon, Japan) using a Melles Griot IMA 101 Argon laser illumination (Melles Griot Laser Group, Carlsbad, CA) was utilized to illuminate near surface and attached colloids, and images were acquired via a CCD camera CoolSNAP HQ (Photometrics, Tucson, AZ). A detailed description of the optical setup is provided in a previous publication.[32]

*Glass surfaces*

Microscope glass slides (Fisher Scientific, Inc; lot number: 18110116) were used as an impinging surface in the radial stagnation point flow cell. Glass slides were cleaned via the SC-1 procedure[33] prior to every experiment. Glass-slide ζ-potentials were adopted from representative values reported in the literature,[34] the corresponding ζ-potentials were -53.5, -70, and -94.5 mV for 20, 6, and 1 mM IS, respectively. For simplicity, heterodomain ζ potentials were assumed to be of the same magnitude and opposite charge relative to the bulk collector.

*Perturbation experiments*

Pazmino et al.[25] examined colloid retention on glass slides in the radial stagnation point flow cell under loading conditions of 6 mM and 20 mM IS and for two average jet

velocities of $1.7x10^{-3}$ and $5.94x10^{-3}$ $ms^{-1}$ for the three colloid sizes examined. In the present work, colloid release in response to perturbations in IS and fluid velocity were examined. To examine IS perturbations, colloids were deposited under the 20 mM IS condition under a specified jet velocity ($1.7x10^{-3}$ $ms^{-1}$) during a loading period ranging from 2 to 4 hours. Following loading, mobile colloids were eluted with colloid-free solution (20 mM, 10 minutes). Reduced IS buffered solution (1 mM) was then injected (15 minutes) with image collection every second. To examine fluid velocity perturbation, colloids were deposited under a specified jet velocity ($5.94$ $x10^{-3}$ $ms^{-1}$) and 6 mM IS during a loading period ranging from 4 to 6 hours, and mobile colloids were eluted with colloid free buffered solution (6 mM, 10 minutes). Fluid velocity was then increased by a factor of 5 (5 minutes) and then a factor of 25 (additional 5 minutes), with image collection as described above. Fractional release of initially attached colloids in response to the perturbations was quantified. The 5x and 25x flow perturbations correspond to average pore water velocities of 17.5 and 87.5 $mday^{-1}$ (calculated for a representative grain size of 510 μm in diameter and porosity of 0.378). Ambient groundwater velocities vary widely with hydrogeologic environment, e.g., 0.15 to 15 $mday^{-1}$ for sand to gravel aquifers, respectively.[35] Whereas the upper end of expected ambient groundwater velocities are a factor of six lower than the 25x perturbation, it seems plausible that extreme precipitation events could raise natural groundwater velocities into this range.

*Non-DLVO forces*

Whereas Ryan and Gschwend[26, 28] did not specify the forces that might lead to an outboard shift in the primary minimum, such forces may include (for example) steric forces arising from interactions of water molecules with surfaces (repulsive hydration

forces) and/or steric forces arising from molecular structures on the surfaces. Additionally, in silica and silica glass minerals in contact with water, formation of silanol groups has been observed due to hydroxylation of the silica surface.[36] These groups may create an extra hydration layer due to the formation of hydrogen bonds among vicinal silanol groups on the collector surface, effectively increasing steric repulsion as demonstrated by Kamiya et al.[37]

In our model we adopted the general representation of hydration repulsion provided by Israelachvili,[38] wherein the repulsive steric energy per unit area of interaction ($W(H)$) decays exponentially as a function of separation distance ($H$) and a characteristic decay length ($\lambda_0$):

$$W(H) = W_0 e^{-\frac{H}{\lambda_0}} \qquad (3.1)$$

where $W_0$ is the maximum repulsive energy per unit area at the closest possible separation distance. The exponential decay of this repulsive interaction is governed by $\lambda_0$ and depends on the surface material and the type of electrolyte in solution. While deviations of DLVO forces at close separation distances (<5 nm) have been attributed to steric interactions in glass,[39] mica,[40] and other mineral surfaces, a complete set of steric interaction parameters ($W_0$ and $\lambda_0$) was provided for mica only. In our simulations $W_0$ values were approximated with those from Pashley,[38] who examined hydration forces between two mica surfaces in 1:1 electrolytes. These values ranged from $3x10^{-3}$ to $3x10^{-2}$ $Jm^{-2}$. Using a $W_0$ value of 0.21 $Jm^{-2}$ for $Na^+$ electrolyte from Pashley,[40] the value of $\lambda_0$ was varied to determine whether colloid reentrainment was simulated. Whereas Pashley[38] found that $\lambda_0$ ranged from 0.17 to 1.1 nm for hydration forces in the presence of monovalent electrolytes between two crossed cylindrical mica sheets having 1-cm radii

of curvature,[38] we may not expect to obtain the same value for $\lambda_0$ in our far smaller radii of curvature microsphere-glass system. Steric and DLVO energy and force expressions are provided in the SI.

*Surface friction*

The stability of colloid deposition is determined by a balance between a driving torque arising from fluid drag and a resisting torque arising from colloid-surface interaction. Release occurs when the resisting torque is reduced below the driving torque (e.g., via IS reduction), or the driving torque is increased above the resisting torque (e.g., via increased fluid drag). In order to account for surface friction, we incorporate adhesion theory[41] into the colloid force and torque balance, as described in detail in Ma et al.,[23] and developed by Johnson et al.,[41] who established that deformation of materials occurs during contact and defines a contact area (contact radius), which couples to the attractive force to define an adhesion torque. The contact area is proportional to the colloid-collector attractive interaction energy. Johnson[30] accounts for losses due to rolling friction via a coefficient of rolling friction that is proportional to the product of the contact radius and a hysteresis loss factor ($\beta$), which accounts for the dissipation of energy of a deformed rolling sphere. Expressions for calculating colloidal forces and energies are provided in Appendix B.

We considered surface friction to be relevant (surfaces in contact) at separation distances inboard of the mean-field barrier maximum. This is an important contrast to other works (e.g., Torkzaban et al.[40]), which considered the surfaces to be in contact (surface friction relevant) under all conditions yielding net colloid-surface attraction, e.g., the secondary minimum. This latter assumption yields colloid arrest at large separation

distances, e.g., 10s to 100s of nm, whereas our assumption restricting contact to within the barrier maximum yields colloid arrest at separation distances in the region where adhesion (driven by van der Waals and net electric double layer attraction in the presence of heterodomains) is balanced by steric repulsion, e.g., approximately 0.86 nm for the range of IS conditions examined.

In contrast to Bergendahl and Grasso,[29] our simulations assumed $\beta = 1$, the reason being that colloid release via perturbation of flow or IS concerns *initiation* of rolling, i.e., a static colloid transitioning to rolling. Whereas by the above reasoning, our simulation of colloid arrest should include a value of $\beta < 1$ to account for increased adhesion energy during the transition from motion to arrest, data are sparse for this parameter, and so we considered it equivalent to 1. In the simulations, surface friction becomes zero when the net colloidal force or the interaction energy becomes repulsive, which occurs via transport of the colloid to a less favorable site, or in response to increased size of the ZOI under lower IS conditions.[25]

*Colloid reentrainment simulations*

A particle trajectory model[25] was used to simulate colloid reentrainment. This model incorporated discrete surface heterogeneity to simulate colloid attachment under unfavorable conditions. Perturbations in flow and IS were simulated in two stages: 1) loading, via colloid injection at the jet exit, and 2) perturbation, wherein fluid velocity was increased by a factor of 5 and 25 relative to the loading velocity, or solution IS was reduced by a factor of 20 relative to the loading IS. The value of $\lambda_0$ (Equation 1) used in all simulations was fit based on comparison of simulated and observed colloid release in response to perturbations, as described below.

## Results and Discussion

The number of attached colloids per unit area following loading differed for the different-sized colloids prior to imposing perturbations (Figure 3.2). It should be noted that error bars in Figure 3.2 represent replicate experiments performed on representative glass slides (n = 2). Colloid reentrainment in response to increased fluid drag and reduced IS was observed in experiments (Figure 3.2). Negligible reentrainment was observed for the 0.25 μm colloids in response to any of the perturbations examined. Negligible reentrainment was observed for all colloid sizes in response to a factor of five increased fluid velocity (not shown). Approximately 82% and 70% of 1.1 and 1.95 μm colloids remained attached after a decrease in IS from 20 to 1 mM (Figure 3.2). Observed colloid release in our experiments contrasts with previous experimental results from Tong and Johnson,[20] who indicated negligible reentrainment for a decrease in IS from 50 and 20 mM to 0.2 mM for all colloid sizes examined (0.1 to 2.0 μm). This lack of reentrainment can potentially be explained by differences in heterogeneity (e.g., coverage by heterodomains) among the slides used in Tong and Johnson[20] versus this study. Glass slides from major distributors show dramatic variations across particular time periods. For example, North et al.[43] showed dramatic variations in colloid retention, as well as Mg content, Ca content, and roughness for pre-2008 versus post-2008 glass slides. It is possible that such variations in glass slides occur periodically, and that manufacture-driven variations in glass slides cause (or at least contribute to) the different colloid iretention behaviors observed by Tong and Johnson[20] relative to this study. Approximately 77% and 48% of 1.1 and 1.95 μm colloids remained attached after

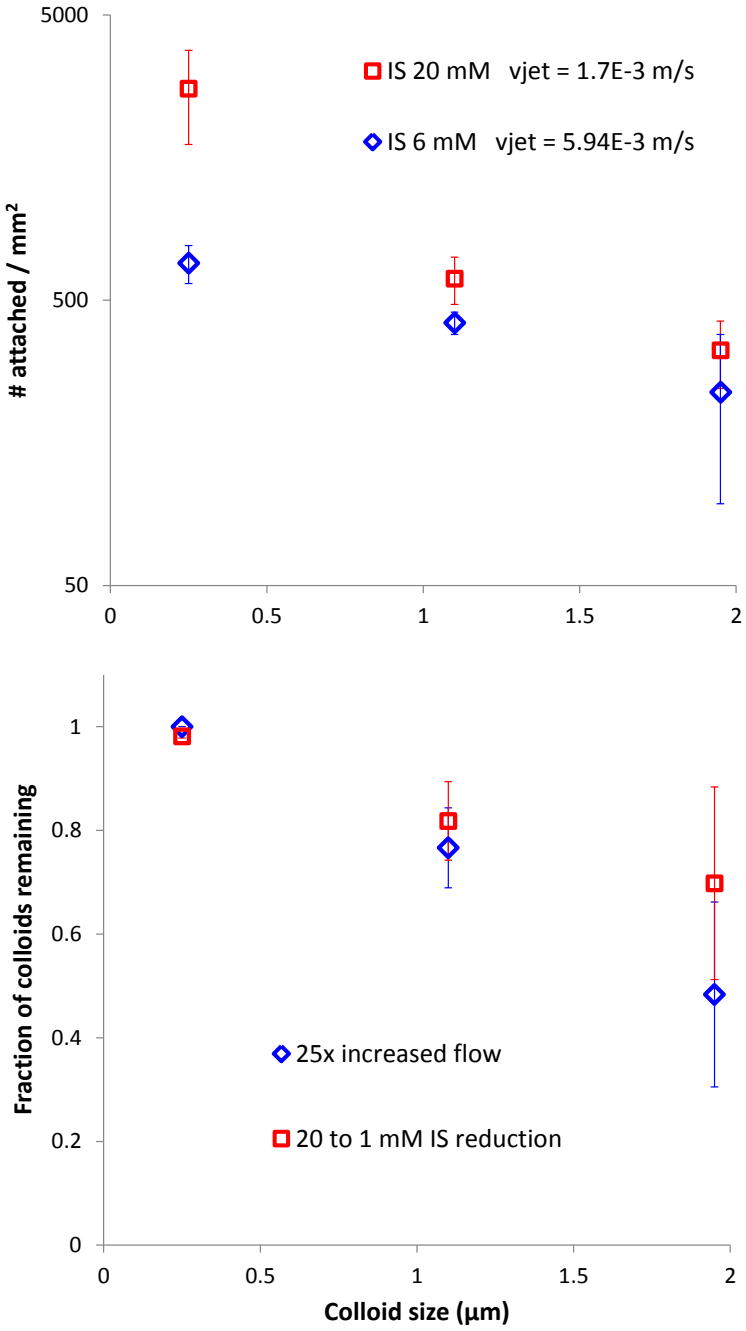


Figure 3.2 Number of colloids attached prior and after perturbations. Top: Number of colloids attached per unit area prior to perturbations. Blue series: IS 6 mM, *V*jet 5.94x10$^{-3}$ m/s. Red series: IS 20 mM, *V*jet 1.7x10$^{-3}$ m/s series. Bottom: Fraction of colloids remaining after IS reduction from 20 to 1 mM (red) and after 25x increased flow (blue). It should be noted that error bars represent replicate experiments (n = 2).

a factor of 25 increased fluid velocity. These results indicate that larger colloids are more

prone to reentrainment in response to perturbations (particularly flow) and were deposited in a relatively metastable mode. Mechanistically, the lesser stability of larger colloids is likely related to the greater fluid drag they experience, as well as possible less favorable interaction with the heterogeneous surface, as will be explored below.

The goal of the simulations was to test whether mechanisms imbedded in the model successfully capture both the differential attachment of various sized colloids on glass surfaces under unfavorable conditions as well as the preferential release of larger colloids in response to perturbations in IS and fluid velocity. Representation of discrete heterogeneity on the glass surfaces using 120 and 60 nm heterodomains with relative frequencies of 1:4, respectively (Pareto power-law size distribution), yielded numbers of attached colloids per unit area that matched well the experiments (Figure 3.2). The rationale for this representation is that the smallest colloids showed highest retention despite having relatively short residence times in the near-surface domain (enhanced diffusion). This indicated a prevalence of small heterodomains (which are able to capture only small colloids). A detailed exploration of surface heterogeneity representation is provided in Pazmino et al. [25] In the absence of steric forces, no simulated release occurred in response to either flow or IS perturbations. The colloid-surface separation distance at which arrest occurred according to the torque balance was ~0.75 nm. Even at this separation distance, simulated colloid-surface attraction was too strong to allow colloid release in response to the perturbations examined here (data not shown).

Inclusion of steric forces in the DLVO-predicted colloid-collector interaction shifted the equilibrium separation distance outward and reduced the strength of colloid surface interactions as shown in an exemplary force profile (Figure 3.3), where the

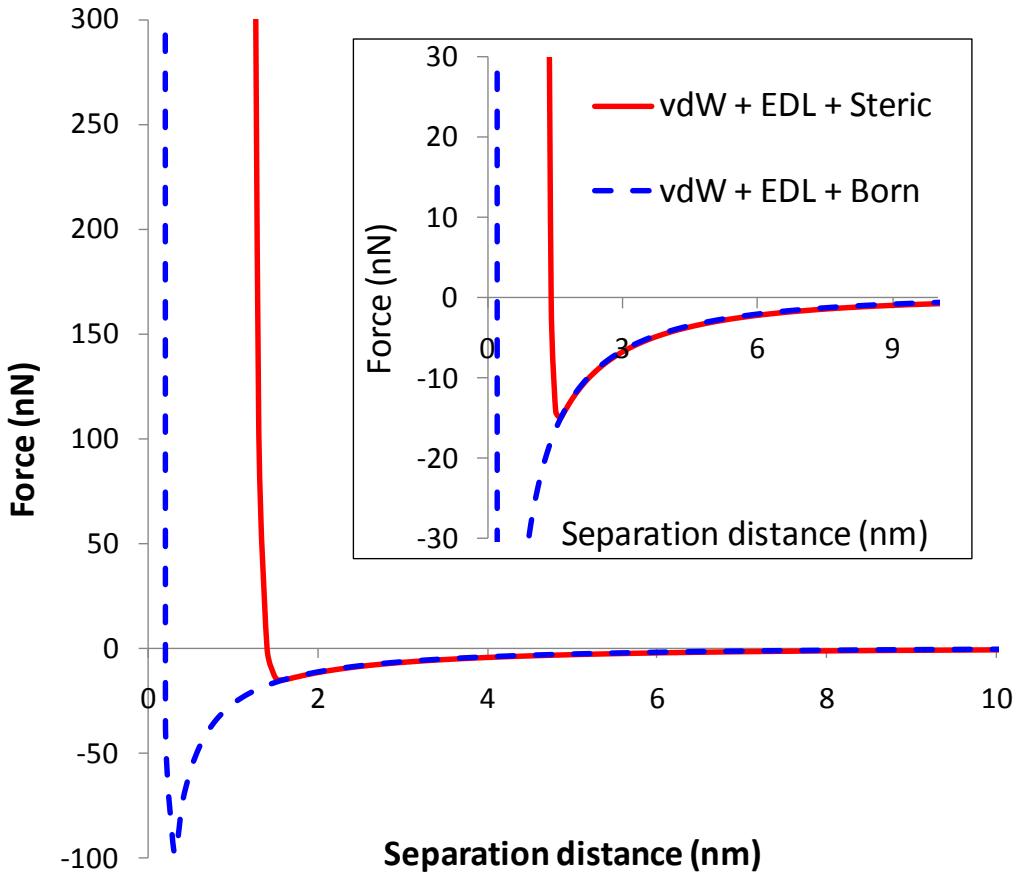


Figure 3.3 Exemplary force profiles with (red) and without (blue) steric contributions assuming complete coverage of ZOI by heterodomain. Force profiles were calculated as described in methods for a 1.95 µm colloid, 6 mM IS, pH = 6.72. $\zeta$ potentials (mV): collector -70, heterodomain +70, particle –29.9. Steric profile corresponds to $\lambda_0$ = 0.12 nm, $W_0$ = 0.21 J/m$^2$. Inset: detail of the outward-shifted primary minimum.

equilibrium separation distance shifted from < 1 nm to ~1.4 nm when steric forces were included (Figure 3.3 inset). With the outward shift, the attractive force within the primary energy minimum decreased one order of magnitude, from 9.4x10$^{-8}$ to 1.2x10$^{-8}$ N (Figure 3.3). The increased fluid drag and decreased adhesion force resulting from the outward shift of the primary energy minimum promoted mobilization of colloids in primary minimum contact. The attractive force corresponding to the secondary minimum was not affected by inclusion of steric forces (not shown). It should be noted that the

steric force was included in attachment simulations (Figure 3.2) that explored the optimal representation of heterogeneity determined by matching the array of colloid retention experiments as described in detail in Pazmino et al. [25]

The simulated release under perturbation was strongly dependent on $\lambda_0$, as shown for the 1.95 μm colloids in response to decreased IS (Figure 3.4), which showed a range from zero to complete release across the range of $\lambda_0$ values from 0.05 to 0.1 nm, which corresponded to average equilibrium separation distances ranging from 0.8 to 1.3 nm (Figure 3.4). A $\lambda_0$ value of 0.0635 nm yielded simulated fractional releases in response to IS and flow perturbations that were reflective of experimental observations (Figure 3.5), although differences between simulated and experimental results were apparent. In the IS perturbations, simulation of a reduction in IS (20 to 1 mM), yielded fractions of colloids remaining of 100% for the 0.25 and 1.1 μm colloids and 87% for the 1.95 μm colloids, whereas experimentally-observed remaining fractions were 98±0.3, 82±7.6, and 70±18.6% for the 0.25, 1.1, and 1.95 μm colloids, respectively (Figure 3.5).

In the fluid velocity perturbations, simulation of a factor of 25 increased fluid velocity yielded a remaining fractions of deposited colloids of 67.9, 0.45, and 0 % for 0.25, 1.1, and 1.95 μm colloids, respectively (Figure 3.5). Whereas this simulated trend with colloid size correctly reflected the trend observed in experiments (100.0, 76.6±7.7, and 48.4±17.8% remaining 0.25, 1.1, and 1.95 μm colloids, respectively), the magnitude of release was overpredicted in the mechanistic simulations.

Simulated release was progressively decreased by reducing the fluid (jet) velocity to factors of 10 and 5, the former being in closest agreement with experimental results (among the three velocity perturbations examined) (Figure 3.5).

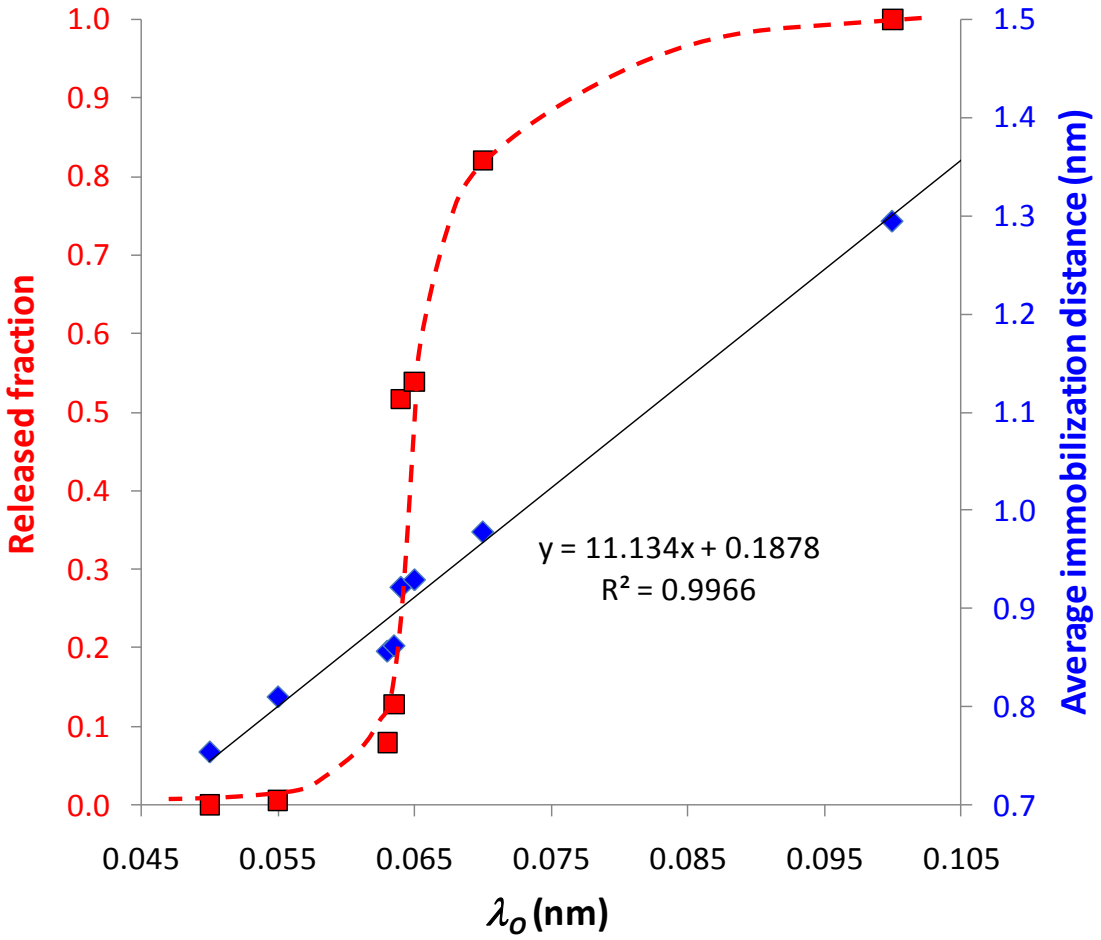


Figure 3.4 Simulated fractional release of 1.95 µm colloids (red squares) in response to decreased IS (20–1 mM) for different steric force decay lengths ($\lambda_0$) and $W_0$ = 0.21 J/m$^2$. Corresponding average colloid immobilization distance (red squares) over 60 and 120-nm radii heterodomains, number ratio 1:4, surface coverage 0.04%.

Qualitative mechanistic prediction of colloid detachment in response to perturbations using the same parameters for quantitative prediction of attachment under unfavorable conditions is a critical step forward for colloid transport simulation under environmental conditions.

Many potential reasons exist for our ability to qualitatively (but not

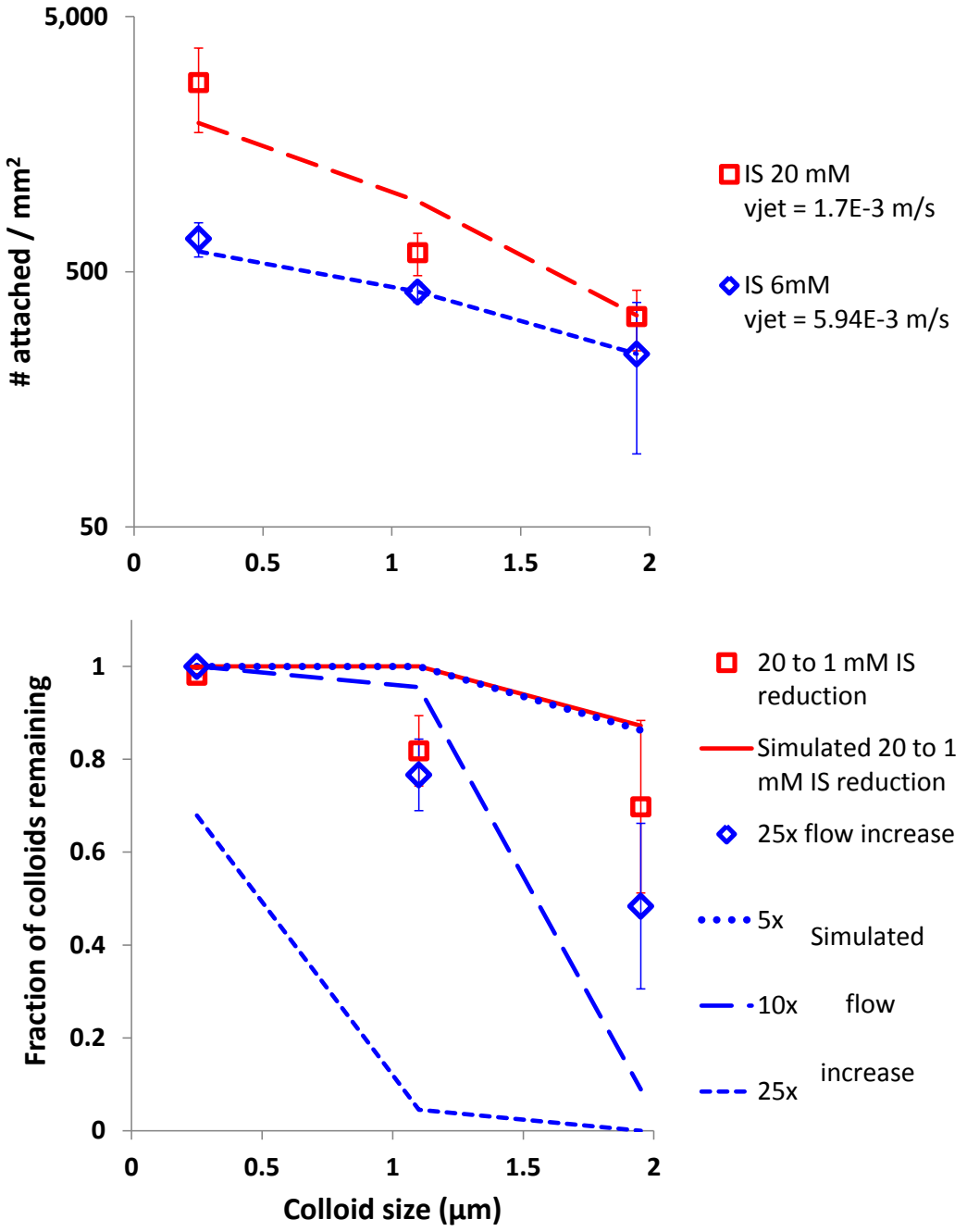


Figure 3.5 Colloid attached prior and after flow and IS perturbations. Top panel: number of colloids attached per unit area as a function of colloid size under two conditions prior to perturbations. Experimental observations shown as discrete symbols, simulations shown as lines. Blue series condition: IS 6 mM, *V*jet $5.94 \times 10^{-3}$ m/s. Red series condition: IS 20 mM, *V*jet $1.7 \times 10^{-3}$ m/s. Bottom panel: Fraction of colloids remaining following perturbation. Red series condition: IS reduction from 20 to 1 mM. Blue series condition: 25x increased flow. Error bars represent replicate experiments (n = 2).

unfavorable conditions is an important step forward for colloid transport simulation under quantitatively) match experimentally-observed colloid release in response to perturbations. One reason is that the process is dynamic, and there may exist kinetic controls on actual release by virtue of fluid mixing and possible kinetic limitations on interfacial processes. The fact that roughness is not explicitly accounted for in the simulations is one potential contributor to the discrepancy. This effect may be significant even on glass surfaces for which roughness is expected to be in the root mean square roughness range of 0.5 nm.[43, 44] Roughness is known to mediate steric forces. For example, the representation of repulsive hydration forces as a monotonic function is more accurate for rough surfaces as opposed to an oscillatory function for perfectly smooth surfaces.[42] Notably, the steric force profile reported by Peschel et al.[39] was obtained by subtraction of DLVO forces from experimentally-observed force profiles on fused silica having asperities ranging 2–3 nm.

Our best-fit primary minimum separation distance was 0.86 nm, a distance that one must consider relative to a datum that is the rough surface. Notably, in experiments, colloid release in response to perturbations is rapid, occurring over the initial few minutes of perturbation. However, the observed release is not instantaneous, whereas in simulations, the release is not only rapid, it is instantaneous. This discrepancy is also related to the concept of colloid relaxation to greater stability on the surface, which is further considered below.

Overprediction of colloid release in response to fluid velocity perturbations might also occur in response to our representation of the fluid flow field as laminar even at a factor of 25 increased flow. Assuming that the experimental flow field was laminar

under all conditions, the corresponding average values of Re were 0.03 for the loading flow and 0.054 and 1.517 for the factor of 10 and 25 flow perturbations, respectively, as determined from the numerical solution of the flow fields. However, for the 25x flow perturbation, the 90$^{th}$ percentile of the Re number distribution was 3.4, indicating a significant fraction of the flow field was in the turbulent regime. This finding indicates that the actual flow field was turbulent at the 25x flow perturbation, and that near-surface fluid velocities in assumed-laminar simulations would overpredict those in the experiment. Furthermore, examination of streamlines for the laminar numerical flow field of the factor of 10 and 25 flow perturbations (Appendix B) indicate the formation of vortices in the jet chamber, leading to the possibility that turbulence in the experimental system shifted near-surface fluid velocities to values below those expected under laminar conditions, possibly explaining the improved simulation under the 10x flow condition.

An additional important characteristic to improve prediction of release in response to perturbation is the heterodomain size and size distribution. The surface heterogeneity calibrated from colloid retention experiments by Pazmino et al.[25] was a simplified power law distribution consisting of only two heterodomain sizes (120 and 60 nm-radii heterodomains). The steep response in simulated colloid release with $\lambda_0$ reflects the narrow distribution of the fractional area of ZOI occupied by heterodomains for an immobilized colloid, e.g, 0.49±0.028 average fractional area for 1.95 μm colloids ($\lambda_0$ = 0.0635 nm, 20 mM IS), which yielded a narrow distribution of immobilization distances, i.e., 0.862±0.041 nm. An example distribution of fractional areas of ZOI coverage by heterodomains for an attached population is given in Appendix B. The narrow distribution of fractional area of ZOI occupied by heterodomains would likely be

widened by incorporation of more heterodomain sizes within the power-law distribution, potentially yielding increased release for 1.1 μm colloids immobilized over smaller heterodomains.

The parameter $\lambda_0$ is a characteristic decay length, as opposed to the larger range over which steric interactions act. This is analogous to the Debye length, which is much smaller than the range over which electric double layer interactions act. As such, $\lambda_0$ has been experimentally fitted to experimental observations.[39, 40] The best-fit $\lambda_0$ values reported by Peschel et al.[39] (0.6–1.2 nm) and Pashley[40] (0.17–1.1 nm) corresponded to steric interaction ranges of ~6 nm. [39, 40] In our system, the best-fit $\lambda_0$ value was 0.0635 nm, which yielded significant steric force (e.g., $>1x10^6$ N for 1.95 μm colloids) out to separation distances ≤1.5 nm. Our relatively small value of $\lambda_0$ may represent 1) the much smaller radii of curvature in our system (0.25 to 2 μm) relative to those of Pashley[38] and Peschel et al.[39] (2-cm). The latter two are more prone to deformation at macroscopic scales under applied loading (which was absent in our system), thereby extending interfacial area and potentially enhancing the range of steric interactions. 2) An aspect not captured in our combined attachment-detachment simulations was the potential relaxation of colloids following arrest deeper into the primary minimum via diffusion while in contact. We did not attempt to simulate this expected behavior because of the difficulty in identifying *a priori* the net motion in the tangential dimension (to which surface friction would be applied) since random diffusion and tangential fluid drag are typically not aligned. Such diffusion in contact would likely yield a greater distribution of stabilities among the attached population, thereby enhancing the fractional release in response to perturbations in IS and flow while potentially allowing greater values of $\lambda_0$ to simulate

the observed attachment, as well as detachment in response to perturbations. Our simulations were terminated upon arrest (zero tangential velocity), suggesting that potential future improvement includes representation of near-surface diffusion in the torque balance leading to arrest. Notably, our flow perturbation experiments indicate that colloids do in reality relax into an equilibrium separation distance that supports strong adhesion, as evidenced by relatively negligible release upon a factor of 5 increase in flow, a behavior that we also observed video microscopy experiments in soda lime glass bead porous media.[9]

The model, even with opportunities for further improvement, allows the influence of IS versus flow perturbations to be examined in mechanistic predictions. However, direct comparison is difficult because the two influences are mechanistically independent (increased flow increases the driving torque, whereas decreased IS decreases the resisting torque). Furthermore, these influences have different ranges in groundwater. While it is reasonable to estimate a potential IS decrease from, e.g., 20 mM to 1 mM in response to heavy precipitation, the corresponding velocity increase depends on the particular attributes of the hydrologic system. Generalizing which influence is more important is not straightforward since the predominance of IS versus flow perturbations is contextual. Our goal was not to rank these influences, but rather to demonstrate that they could be predicted mechanistically via incorporation of heterogeneity in the force and torque balance.

An advantage of the impinging jet system is that the entire observed surface is subject to fluid shear, which allows testing of the hypothesis that surface friction extends to secondary minima and immobilizes colloids there. [40] Under the loading conditions in

the impinging jet, average pore water velocities were in the range of 4–14 mday$^{-1}$,[20] and significant colloid immobilization was observed in these experiments. In simulations extending surface friction to the secondary minimum (heterodomains absent, 20 mM IS), immobilization of 1.95 μm colloids was not simulated until the fluid velocity was reduced by three orders of magnitude below the lowest fluid velocity in our experimental range. This indicates that immobilization in secondary minima cannot explain our experimental observations. Furthermore, when surface friction was extended to the secondary minimum, the simulated average colloid-surface separation distance was 50.72 ± 0.031 nm, and subsequent reduction of IS to 1 mM, or increase in fluid velocity by a factor of two, mobilized the entire (not partial) population of previously immobilized colloids. This simulated result contradicts the observed fractional release of the attached population in response to significant perturbations. Therefore, extension of surface friction to the secondary minimum cannot explain colloid immobilization in the impinging jet under the conditions examined here, nor can it explain colloid immobilization in glass bead porous media under the conditions examined by Johnson et al.[9]

Qualitative agreement of simulated versus experimental release in response to perturbations suggests that steric repulsion (e.g., hydration forces), along with attachment to discrete heterodomains, may be responsible for the observed release of immobilized colloids from surfaces in response to perturbations. This is an important contrast to interpretations that relegate colloid release to secondary minima.[45, 46] The results shown here demonstrate that incorporation of steric interactions and discrete heterogeneity not only quantitatively predicts colloid immobilization (attachment) as a function of colloid

size, fluid velocity, and IS under unfavorable conditions,[25] but also provides mechanistic qualitative prediction of colloid release (from primary minimum contact) in response to perturbations using the same physicochemical parameters used to predict attachment.

Our experiments and simulations correspond to release of colloids from soda lime glass slides, which are chemically homogeneous and topographically smooth relative to natural aquifer minerals. However, even these simplest of surfaces display heterogeneity (oxides of Na, Mg, Ca, and Al) that is likely responsible for colloid attachment under unfavorable conditions. It is reasonable to expect that natural aquifer minerals will show greater extent of chemical and physical heterogeneity relative to soda lime glass. We have begun to examine colloid deposition on representative mineral surfaces that are expected to be unfavorable under groundwater conditions, e.g., muscovite, albite, and quartz. Notably, trends in colloid deposition on these surfaces as a function of colloid size, IS, and fluid velocity are similar to those on soda lime glass. However, the extent of attachment (and detachment) varies greatly among these surfaces and relative to soda lime glass, as will be reported in a forthcoming manuscript.

With respect to relevance to pathogen mobilization, pathogen extra-cellular polymers and surface structures (e.g., fimbriae or flagella) may enhance microbial adhesion and may enhance or reduce attachment stability.[47, 48] The presence of humic substances and divalent cations in natural waters may also diminish or enhance adhesion through electrosteric and cation bridging mechanisms. These characteristics of pathogen surfaces in environmental settings create complexity relative to carboxylate modified polystyrene latex microspheres. Whereas the results shown here correspond to the latter, our findings for simple colloids suggest that the process may apply to pathogen release.

These models at least provide a platform from which to examine whether immobilized pathogens in primary minimum contact with surfaces may potentially be released in response to perturbations in IS or fluid velocity.

## References


(1) Curriero, F. C.; Patz, J. A.; Rose, J. B.; Lele, S. The Association between Extreme Precipitation and Waterborne Disease Outbreaks in the United States, 1948–1994. *Am. J. Public Health* **2001,** *91* (8), 1194–1199.

(2) Auld, H.; MacIver, D.; Klaassen, J. Heavy Rainfall and Waterborne Disease Outbreaks: The Walkerton Example. *J. Toxicol. Environ. Health, Part A* **2004,** *67* (20-22), 1879–1887.

(3) Dorner, S. M.; Anderson, W. B.; Slawson, R. M.; Kouwen, N.; Huck, P. M. Hydrologic Modeling of Pathogen Fate and Transport. *Environ. Sci. Technol.* **2006,** *40* (15), 4746–4753.

(4) Bradbury, K. R.; Borchardt, M. A.; Gotkowitz, M.; Spencer, S. K.; Zhu, J.; Hunt, R. J., Source and Transport of Human Enteric Viruses in Deep Municipal Water Supply Wells. *Environ. Sci. Technol.* **2013,** *47* (9), 4096–4103.

(5) Uejio, C. K.; Yale, S. H.; Malecki, K.; Borchardt, M. A.; Anderson, H. A.; Patz, J. A., Drinking Water Systems, Hydrology, and Childhood Gastrointestinal Illness in Central and Northern Wisconsin. *Am. J. Public Health* **2014,** *104* (4), 639–646.

(6) Ray, C.; Schubert, J.; Linsky, R. B.; Melin, G. Introduction. In *Riverbank Filtration: Improving Source Water Quality*; Ray C. Melin G., Linsky R. B. (Eds.); Kluwer Academic Publishers and National Water Res. Institute: Boston, 2002.

(7) Kenst, A. B.; Perfect, E.; Wilhelm, S. W.; Zhuang, J.; McCarthy, J. F.; McKay, L. D. Virus Transport during Infiltration of a Wetting Front into Initially Unsaturated Sand Columns. *Environ. Sci. Technol.* **2008,** *42* (4), 1102–1108.

(8) Kuznar, Z. A.; Elimelech, M., Direct Microscopic Observation of Particle Deposition in Porous Media: Role of the Secondary Energy Minimum. *Colloids and Surfaces A: Physicochemical and Engineering Aspects* **2007,** *294* (1-3), 156–162.

(9) Johnson, W. P.; Pazmino, E.; Ma, H. Direct Observations of Colloid Retention in Granular Media in the Presence of Energy Barriers, and Implications for Inferred Mechanisms from Indirect Observations. *Water Res.***2010,** *44* (4), 1158–1169.

(10) Derjaguin, B. Theory of the Stability of Strongly Charged Lyophobic Sols and the Adhesion of Strongly Charged Particles in Solutions of Electrolytes. *Acta Physicochim. USSR* **1941,** *14*, 633–662.

(11) Verwey, E.; Overbeek, J. T. G. Theory of the Stability of Llyophobic Colloids. J. Colloid Sci. **1955,** *10* (2), 224–225.

(12) Elimelech, M.; O'Melia, C. R. Kinetics of Deposition of Colloidal Particles in Porous Media. *Environ. Sci. Technol.* **1990,** *24* (10), 1528–1536.

(13) Hahn, M. W.; Abadzic, D.; O'Melia, C. R. Aquasols: On the Role of Secondary Minima. *Environ. Sci. Technol.* **2004,** *38* (22), 5915–5924.

(14) Redman, J. A.; Walker, S. L.; Elimelech, M. Bacterial Adhesion and Transport in Porous Media: Role of the Secondary Energy Minimum. *Environ. Sci. Technol.* **2004,** *38* (6), 1777–1785.

(15) Shen, C.; Li, B.; Huang, Y.; Jin, Y. Kinetics of Coupled Primary- and Secondary-minimum Deposition of Colloids under Unfavorable Chemical Conditions. *Environ. Sci. Technol.* **2007,** *41* (20), 6976–6982.

(16) Tosco, T.; Tiraferri, A.; Sethi, R. Ionic Strength Dependent Transport of Microparticles in Saturated Porous Media: Modeling Mobilization and Immobilization Phenomena under Transient Chemical Conditions. *Environ. Sci. Technol.* **2009,** *43* (12), 4425–4431.

(17) Sang, W.; Morales, V. L.; Zhang, W.; Stoof, C. R.; Gao, B.; Schatz, A. L.; Zhang, Y.; Steenhuis, T. S. Quantification of Colloid Retention and Release by Straining and Energy Minima in Variably Saturated Porous Media. *Environ. Sci. Technol.* **2013,** *47* (15), 8256–8264.

(18) Frautschi, S. C., *The Mechanical Universe: Mechanics and Heat*. Cambridge University Press: New York, 1986.

(19) Johnson, W. P.; Li, X.; Tong, M.; Ma, H. Comment on "Transport and Fate of Bacteria in Porous Media: Coupled Effects of Chemical Conditions and Pore Space Geometry" by Saeed Torkzaban et al. *Water Resour. Res.* **2009,** *45* (9).

(20) Tong, M.; Johnson, W. P. Excess Colloid Retention in Porous Media as a Function of Colloid Size, Fluid Velocity, and Grain Angularity. *Environ. Sci. Technol.* **2006,** *40* (24), 7725–7731.

(21) Duffadar, R. D.; Davis, J. M. Interaction of Micrometer-scale Particles with Nanotextured Surfaces in Shear Flow. *J. Colloid Interface Sci.* **2007,** *308* (1), 20–29.

(22) Duffadar, R. D.; Davis, J. M. Dynamic Adhesion Behavior of Micrometer-scale Particles Flowing over Patchy Surfaces with Nanoscale Electrostatic Heterogeneity. *J. Colloid Interface Sci.* **2008,** *326* (1), 18–27.

(23) Ma, H.; Pazmino, E.; Johnson, W. P. Surface Heterogeneity on Hemispheres-in-cell Model Yields all Axperimentally-observed Non-straining Colloid Retention Mechanisms in Porous Media in the Presence of Energy Barriers. *Langmuir* **2011,** *27* (24), 14982–14994.

(24) Bendersky, M.; Davis, J. M. DLVO Interaction of Colloidal Particles with Topographically and Chemically Heterogeneous Surfaces. *J. Colloid Interface Sci.* **2011,** *353* (1), 87–97.

(25) Pazmino, E.; Trauscht, J.; Dame, B.; Johnson, W. P., Power Law Size-distributed Heterogeneity Explains Colloid Retention on Soda Lime Glass in the Presence of Energy Barriers. *Langmuir* **2014**, *30* (19), 5412–5421

(26) Ryan, J. N.; Gschwend, P. M. Effect of Solution Chemistry on Clay Colloid Release from an Iron Oxide-coated Aquifer Sand. *Environ. Sci. Technol.* **1994,** *28* (9), 1717–1726.

(27) Van Oss, C. J.; Chaudhury, M. K.; Good, R. J., Interfacial Lifshitz-van der Waals and Polar Interactions in Macroscopic Systems. *Chem. Rev.* **1988,** *88* (6), 927–941.

(28) Ryan, J. N.; Gschwend, P. M. Effects of Ionic Strength and Flow Rate on Colloid Release: Relating Kinetics to Intersurface Potential Energy. *J. Colloid Interface Sci.* **1994,** *164* (1), 21–34.

(29) Bergendahl, J.; Grasso, D. Prediction of Colloid Detachment in a Model Porous Media: Hydrodynamics. *Chem. Eng. Sci.* **2000,** *55* (9), 1523–1532.

(30) Johnson, K. L. *Contact Mechanics*. Cambridge University Press: Cambridge, U.K., 1985; pp 179–184.

(31) Ohshima, H. Electrophoresis of Soft Particles. *Adv. Colloid Interface Sci.* **1995,** *62* (2–3), 189–235.

(32) Johnson, W. P.; Tong, M. Observed and Simulated Fluid Drag Effects on Colloid Deposition in the Presence of an Energy Barrier in an Impinging Jet System. *Environ. Sci. Technol.* **2006,** *40* (16), 5015–5021.

(33) Kern W.; Poutinen D. A**.** Cleaning Solution based on Hydrogen Peroxide for Use in Silicon Semiconductor Technology. *RCA Rev.* **1970**, *31*, 187–205.

(34) Kirby, B. J.; Hasselbrink, E. F. Zeta Potential of Microfluidic Substrates: 1.

Theory, Experimental Techniques, and Effects on Separations. *Electrophoresis* **2004,** *25* (2), 187–202.

(35) Harter, T., *Basic Concepts of Groundwater Hydrology*. UCANR Publications: Sacramento, 2003.

(36) Zhuravlev, L., The Surface Chemistry of Amorphous Silica. Zhuravlev Model. *Colloids Surfaces A*. **2000,** *173*, (1), 1–38.

(37) Kamiya, H.; Mitsui, M.; Takano, H.; Miyazawa, S., Influence of Particle Diameter on Surface Silanol Structure, Hydration Forces, and Aggregation Behavior of Alkoxide-Derived Silica Particles. *J. Am. Ceram. Soc.* **2000,** *83*, (2), 287–293.

(43) Israelachvili, J. N., *Intermolecular and Surface Forces: Revised Third Edition*. Elsevier Science: Atlanta, 2011.

(38) Peschel, G.; Belouschek, P.; Müller, M.; Müller, M.; König, R., The Interaction of Solid Surfaces in Aqueous Systems. *Colloid Polym. Sci.* **1982,** *260* (4), 444–451.

(39) Pashley, R. M., Hydration Forces between Mica Surfaces in Electrolyte Solutions. *Adv. Colloid Interface Sci.* **1982,** *16* (1), 57–62.

(40) Johnson, K. L.; Kendall, K.; Roberts, A. D., Surface Energy and the Contact of Elastic Solids. *Proc. R. Soc. London, Ser. A* **1971,** *324* (1558), 301–313.

(41) Torkzaban, S.; Tazehkand, S. S.; Walker, S. L.; Bradford, S. A., Transport and Fate of Bacteria in Porous Media: Coupled Effects of Chemical Conditions and Pore Space Geometry. *Water Resour. Res.* **2008,** *44* (4, W04403).

(42) North, S. H.; Lock, E. H.; King, T. R.; Franek, J. B.; Walton, S. G.; Taitt, C. R., Effect of Physicochemical Anomalies of Soda-lime Silicate Slides on Biomolecule Immobilization. *Anal. Chem.* **2009,** *82* (1), 406–412.

(43) Assemi, S.; Nalaskowski, J.; Johnson, W. P., Direct Force Measurements between Carboxylate-modified Latex Microspheres and Glass using Atomic Force Microscopy. *Colloids and Surfaces A*. **2006,** *286* (1-3), 70–77.

(44) Hahn, M. W.; Abadzic, D.; O'Melia, C. R., Aquasols: On the Role of Secondary Minima. *Environ. Sci. Technol.* **2004,** *38* (22), 5915–5924.

(45) Tufenkji, N.; Elimelech, M., Breakdown of Colloid Filtration Theory: Role of the Secondary Energy Minimum and Surface Charge Heterogeneities. *Langmuir* **2005,** *21* (3), 841–852.

(46) Jucker, B. A.; Zehnder, A. J. B.; Harms, H., Quantification of Polymer

Interactions in Bacterial Adhesion. *Environ. Sci. Technol.* **1998,** *32* (19), 2909–2915.

(47) McClaine, J. W.; Ford, R. M., Reversal of Flagellar Rotation is Important in Initial Attachment of *Escherichia coli* to Glass in a Dynamic System with High- and Low-ionic-strength Buffers. *Appl. Environ. Microbiol.* **2002,** *68* (3), 1280–1289.

# CHAPTER 4

# MECHANISTIC CORRELATION EQUATION FOR PREDICTING NANO- AND MICROPARTICLE COLLISION EFFICIENCIES ($\alpha$) IN GRANULAR FILTRATION UNDER ENVIRONMENTAL CONDITIONS


## Abstract

We present a mechanistically-based correlation equation to predict collision efficiency for colloid attachment under unfavorable conditions in granular media. The correlation was developed from a mechanistic discrete heterogeneity colloid trajectory model that includes discrete nanoscale zones of attraction (heterodomains) to explain colloid attachment under bulk-repulsive colloid-collector interactions, which are prevalent in environmental systems. In a previous study, heterodomain characteristics (size distribution and surface coverage) on soda-lime glass were extracted via comparison of colloid (carboxylate-modified polystyrene latex) retention experiments and trajectory simulations for a range of colloid diameters (0.25 to 1.95 μm), ionic strengths (IS, 6 to 20 mM), and pore water velocities (1.9 to 8.2 $mday^{-1}$) at a solution pH of 6.7. In this study, we demonstrate that a simple correlation equation calibrated from the discrete heterogeneity simulations accurately predicts previously-reported collision efficiencies ($\alpha$) of carboxylate-modified polystyrene latex colloids in packed porous media (soda-lime glass beads) across a much broader range of colloid sizes (0.06 to 3.1 μm), IS (0.1 to

300 mM), and pore water velocities (4 to 588 $mday^{-1}$). The correlation equation captures experimental trends of $\alpha$ with colloid size via the product of two dimensionless parameters: 1) the colloidal number defined as the ratio of attractive (van der Waals) to repulsive (electric double layer) energies and 2) the fraction of colloids that persist in the secondary minimum as determined via the Maxwell kinetic energy distribution. This product is scaled by a leading coefficient that is a linear function of the surface coverage by heterodomains. This approach provides the first mechanistic predictor of colloid filtration under environmental (unfavorable) conditions, with anticipated extension to noncircumneutral pH conditions, as well as other unfavorable environmental surfaces via representative heterogeneity, i.e., the leading coefficient (surface coverage by heterodomains) and heterodomain size distribution.

## Introduction

### *Background*

Granular filtration is a critical process for several environmental contexts including low energy water treatment using river bank filtration,[1, 2] subsurface delivery of nanoparticles and bacteria for contaminant remediation,[3] and determination of set-back distances between pathogen sources and drinking water supplies.[4, 5] Under environmental conditions, the above-mentioned nano- and microparticles, herein referred to as colloids, experience repulsive forces with the granular media, resulting in unfavorable conditions for attachment. Prediction of colloid retention under unfavorable conditions has challenged colloid transport research for several decades. The mechanistic basis for colloid filtration theory (CFT), colloid force, and torque balance predicts zero attachment even for very modest colloid-collector repulsion.[6–8] This outcome of mechanistic

simulations prompted introduction of an empirically-based parameter ($\alpha$) to represent the number of colloids that are observed to attach under unfavorable conditions relative to those that attach under favorable conditions (absent colloid-collector repulsion). Because CFT predicts well attachment under favorable conditions ($\eta_{fav}$), at least for simple uniform colloids and media, $\alpha$ is multiplied by $\eta_{fav}$ in order to predict attachment under unfavorable conditions ($\eta_{unf}$).

*Semiempirical approaches*

Among the approaches to predict $\alpha$ are semiempirical approaches, the first and simplest being a correlation equation developed by Elimelech[9]:

$$\alpha_{Eli} = 0.0257(N_{col})^{1.19} \qquad (4.1)$$

where $N_{col}$ represents the ratio of attractive to repulsive colloidal interactions and is defined as follows:

$$N_{col} = \frac{A_{132}}{\varepsilon_0 \varepsilon_r \xi_p \xi_c \ \kappa^{-1}} \qquad (4.1b)$$

where $A_{132}$ is the combined Hamaker constant for the colloid, water, and porous media, $\varepsilon_o$ and $\varepsilon_r$, are the absolute and relative permittivities in vacuum and water, respectively. The parameters $\zeta_p$ and $\zeta_c$ are the mean-field potentials of the colloid and collector surfaces, and $\kappa^{-1}$ is the inverse Debye length. The reported fitted coefficient (0.0257) and power (1.19) correspond to the general set of experiments reported by Elimelech.[9]

Subsequently, Bai and Tien[10] used the Buckingham Pi theorem to conduct dimensional analysis of relevant variables applied to data from previous studies.[7, 9, 11]

They examined the utility of 11 dimensionless parameters and concluded that only four dimensionless parameters were necessary to explain the array of experimental data. Similar to Elimelech,[9] the dimensionless parameters are functions of mean-field characteristics of the system. In a subsequent study, Bai and Tien[12] updated the original equation coefficients via inclusion of additional experimental results, as described below. A more recent correlation equation was provided by Chang et al.[13] where $\alpha$ is represented as the summation of four terms that account for the contributions of colloidal forces, diffusion, interception, and settling. The coefficients and powers were fitted to previously-reported experiments[7, 9, 11] and also include experimental data provided by Bai and Tien.[12] The dimensionless parameters, coefficients, and powers for the Bai and Tien[10, 12] and Chang et al.[13] semiempirical equations are provided below.

Whereas semiempirical expressions are useful tools to quantify $\alpha$, their applicability is limited by the experimental data utilized in developing the expressions. Furthermore, these semiempirical approaches are based on mean-field parameters utilized to describe the repulsive barrier without representing the mechanisms that allow attachment to occur under unfavorable conditions.

*Maxwell mechanistic approach*

Whereas mechanistic force and torque balances rely on simulation of colloid trajectories to quantify attachment, an alternative mechanistic approach recognizes that colloids may remain in weak association with the collector surface via so called secondary minimum interactions outboard of (at greater separation distances than) the repulsive barrier. This approach proposed by Hahn and O'Melia[14] is called the Maxwell approach because it is based on the Maxwell–Boltzmann distribution of kinetic energies

within a colloid population.[15] The Maxwell approach determines the fraction of the colloid population that has kinetic energies less than the depth of the secondary energy minimum. This so called "cold" fraction of colloids has insufficient kinetic energy to escape the secondary minimum and is effectively retained near the collector surface. The apparent proportionality between secondary minimum depth, cold fraction of colloid population, and observed colloid retention in packed column experiments[14, 16, 17] indicate that the Maxwell approach is a useful first-order predictor of colloid retention. However, the Maxwell approach does not predict immobilization of colloids since they remain outboard of the repulsive barrier, unless one considers surface friction to extend to secondary minima.[19] Retention in packed column experiments includes both genuinely attached (immobilized) and secondary minimum-associated colloids, as known from direct observation in micromodels (e.g., experiments reported by Tong and Johnson,[8] Auset and Keller,[19] and Johnson et al.[20]).

*Discrete heterogeneity mechanistic approach*

Only recently have models been developed that predict genuine attachment when colloid-collector repulsion exists. Predominant among these models are those that represent local reduction or elimination of repulsion due to the presence of nanoscale domains of colloid-collector attraction arising from chemical and/or physical heterogeneity.[21–27]

The discrete heterogeneity model[27] incorporates the contributions of nanoscale zones of colloid-collector attraction (heterodomains) in the force and torque balance that governs colloid trajectories. Attachment to glass surfaces of carboxylate-modified polystyrene latex colloids ranging in size from 0.25 to 1.95 μm was correctly predicted

under varied IS and fluid velocity conditions when the discrete heterogeneity was represented by Pareto power-law size-distributed heterodomains at a total surface coverage of 0.04%. The Pareto power-law size distribution was approximated with two heterodomain sizes, 120 and 60 nm (radii), at a number frequency ratio of 1:4, respectively. Notably, after quantitatively predicting attachment, this model was also able to qualitatively predict detachment in response to fluid velocity and IS perturbation using the same set of parameters.[28]

*Objective*

In this paper, we compare predictions of deposition efficiency ($\alpha$) among the various approaches described above to examine the performance of the discrete heterogeneity mechanistic model relative to the other existing approaches for prediction of $\alpha$. We provide a new correlation equation based on mechanistic discrete heterogeneity simulations for prediction of $\alpha$ under unfavorable conditions. The predictions match observations from porous media and impinging jet geometries under a large range of colloid sizes, fluid velocities, and solution IS. Because the majority of reported experiments with detailed characteristics concern carboxylate-modified polystyrene latex microsphere on silica surfaces, we discuss anticipated extension of the correlation equation to other pH conditions and other unfavorable surfaces using representative discrete heterogeneity.

## Methods

*Rationale for using impinging jet system*

The goal of our investigation is to predict colloid attachment (immobilization) under unfavorable conditions. In packed porous medium column experiments, attachment is not distinguished from retention without attachment (i.e., retention via secondary minimum association). This distinction is made; however, in impinging jet systems, also known as radial stagnation point flow systems, where the flow is directed orthogonal to a planar surface, and colloid motion and immobilization are observed directly. Because CFT considers porous media to be fundamentally comprised of multiple forward flow stagnation zones where colloids are delivered to surfaces, impinging jets are a logical choice to represent this critical topological feature in porous media.

*Representative discrete heterogeneity via comparison of simulations to experiments*

In a previous study,[27] representative surface heterogeneity characteristics of soda-lime glass slides were determined via comparison of experimentally-observed deposition under unfavorable conditions with trajectory simulations in an impinging jet geometry. The discrete heterogeneity model was used to simulate colloid attachment on a surface with nanoscale heterodomains (discrete zones of favorable colloid-collector interaction), and their characteristics (size and surface coverage) were tuned to quantitatively capture observed depositions across a range of colloid sizes (0.25 to 1.95 μm), ionic strengths (IS) (6 to 20 mM), and average jet fluid velocities (148 to 513 $mday^{-1}$).

The model revealed that different-sized colloids interact differently with a given

heterodomain size; e.g., 1.95 μm colloids require relatively large heterodomains to attach, and 0.25 μm colloids attach indiscriminately to small and large heterodomains. The interaction is governed by the zone of influence (ZOI), which is the zone surrounding the closest separation point between the interacting surfaces, within which colloid-collector interactions are significant. Because of the rapid decay of this interaction with increasing separation distance (due to colloid curvature), the ZOI is significantly smaller than the projected area of the colloid. Duffadar et al.[29] determined that the radius of the ZOI ($a_{ZOI}$) is

$$a_{ZOI} \sim 2\sqrt{\kappa^{-1}a_p} \qquad (4.2)$$

where $a_p$ is the colloid radius. Note that $a_{zoi}$ is a function of the inverse Debye length, and therefore it increases with decreasing IS.

In order to generate net attraction, the heterodomain must occupy a significant fraction of the ZOI. Because the ZOI increases with colloid size, a given heterodomain will be more effective in arresting smaller relative to larger colloids. Likewise, because the ZOI of a given colloid is larger at lower IS, a given heterodomain will be more effective in arresting a given-sized colloid at higher IS relative to lower IS. The drag force resisting attachment (or driving detachment) increases with increasing velocity, thereby making colloid attachment and detachment each functions of colloid size, IS, and fluid velocity.

*Maxwell approach*

Hahn and O'Melia[14] proposed that the fraction of colloids retained in the secondary minimum ($\alpha_{2min}$) is equal to

$$\alpha_{2min} = 1 - \int_{v_{p(hot)}}^{\infty} f_{Max(v_p)} dv_p \qquad (4.3a)$$

where $f_{max(vp)}$ is the Maxwell-Boltzmann distribution cast in terms of velocity[15]:

$$f_{Max(v_p)} = 4\pi \left(\frac{m_p}{2\pi kT}\right)^{(3/2)} {v_p}^2 e^{\left(\frac{-\frac{1}{2}m_p {v_p}^2}{kT}\right)} \qquad (4.3b)$$

where $m_p$ is the particle mass, $v_p$ is the particle velocity, $k$ the Boltzmann constant, and $T$ the absolute temperature. The integral of $f_{max(vp)}$ represents the fraction of the population of colloids with kinetic energy greater than the corresponding secondary minimum energy depth ($\Phi_{2min}$), where the integral lower limit is the velocity threshold at which the colloid is "hot" enough to escape the secondary minimum:

$$v_{p(hot)} = \left(\frac{2\Phi_{2min}}{m_p}\right)^{0.5} \qquad (4.3c)$$

*Semiempirical approaches*

The semiempirical correlation equation developed by Bai and Tien[10] is

$$\alpha_{Bai\&Tien\ 1996} = 1.0118x10^{-3}\ [(N_{LO})^{0.8459}(N_{E1})^{-0.2676}\ (N_{E2})^{3.8328}(N_{DL})^{1.6776}\ ] \qquad (4.4a)$$

where $N_{LO}$ is the London-van der Waals number, $N_{E1}$ and $N_{E2}$ the first and second

electrokinetic parameters, and $N_{DL}$ is the electric double layer force parameters defined as

$$N_{LO} = \frac{4A_{132}}{9\pi\mu {d_p}^2 v_{sup}} \quad (4.4b)$$

$$N_{E1} = \frac{\varepsilon_0 \varepsilon_r ({\xi_p}^2 + {\xi_c}^2)}{3\pi\mu d_p v_{sup}} \quad (4.4c)$$

$$N_{E2} = \frac{2\xi_p \xi_c}{({\xi_p}^2 + {\xi_c}^2)} \quad (4.4d)$$

$$N_{DL} = \frac{d_p}{\kappa^{-1}} \quad (4.4e)$$

where $\mu$ is the fluid viscosity, $v_{sup}$ is the superficial water velocity, and $d_p$ is the colloid diameter. Bai and Tien[12] updated equation 4a coefficients and powers via inclusion of additional experimental results to yield the following correlation equation:

$$\alpha_{Bai\&Tien\ 1999} = 2.527x10^{-3}\ (N_{LO})^{0.7031}(N_{E1})^{-0.3121}(N_{E2})^{3.5111}(N_{DL})^{1.352} \quad (4.5)$$

A more recent correlation equation was provided by Chang et al.,[13] where $\alpha$ is represented as the summation of four terms that account for the contributions of colloidal forces, diffusion, interception, and settling as shown in the following equation:

$$\alpha_{Chang} = 0.024N_{DLC}^{0.969}N_{E1C}^{-0.423}N_{E2C}^{2.88}N_{LOC}^{1.5} + 3.176A_S^{\frac{1}{3}}N_R^{-0.081}N_{Pe}^{-0.715}N_{LOC}^{2.687} + 0.222A_S N_R^{3.041}N_{Pe}^{-0.514}N_{LOC}^{0.125} + N_R^{-0.24}N_G^{1.11}N_{LOC} \quad (4.6a)$$

where the $N_{DLC}$, $N_{LOC}$, $N_{E1C}$, and $N_{E2C}$ dimensionless parameters are analogous to $N_{DL}$, $N_{LO}$, $N_{E1}$, and $N_{E2}$ in the Bai and Tien[10,12] equations. Their definitions are as follows:

$$N_{DLC} = \frac{d_p}{2\kappa^{-1}} \tag{4.6b}$$

$$N_{LOC} = \frac{A_{132}}{6kT} \tag{4.6c}$$

$$N_{E1C} = \frac{\varepsilon_0 \varepsilon_r d_p \left(\xi_p{}^2 + \xi_c{}^2\right)}{8kT} \tag{4.6d}$$

$$N_{E2C} = \frac{2\frac{\xi_p}{\xi_c}}{1+\left(\frac{\xi_p}{\xi_c}\right)^2} \tag{4.6e}$$

$N_R$, $N_{Pe}$, and $N_G$ are the aspect number (collector to colloid diameter ratio), the Péclet number (convective to diffusive transport), and gravity number (ratio of Stokes colloid settling velocity to fluid superficial velocity) as defined below:

$$N_R = \frac{d_p}{d_c} \tag{4.6f}$$

$$N_{Pe} = \frac{v_{sup} d_c}{D_{E-S}} \tag{4.6g}$$

$$N_G = \frac{v_{sup} d_p g \left(\rho_p - \rho_f\right)}{18\mu v_{sup}} \tag{4.6h}$$

where $d_c$ is the grain diameter, $D_{E\text{-}S}$ is the Einstein-Stokes diffusion coefficient,[30] $\rho_p$ and $\rho_f$ are the densities of the colloid and fluid, and g is the gravity acceleration. $A_S$ is a geometric parameter that describes the geometry of the flow field[31] and is dependent solely on the porosity ($\theta$) of the porous media:

$$A_S = \frac{2\left(1-(1-\theta)^{5/3}\right)}{2-3(1-\theta)^{1/3}+3(1-\theta)^{1/3}-2(1-\theta)^2} \tag{4.6i}$$

*Comparing predictions among impinging jet and porous media geometries*

Existing semiempirical approaches to predict $\alpha$ were developed from colloid transport experiments in porous media packed columns.[9,10,12,13] In contrast to porous media, impinging jet systems directly distinguish attached colloids from slow-moving secondary minimum-associated colloids; however, typically only the attached colloids are reported. Retention of secondary minimum-associated colloids over the scale of the impinging jet observation area can be quantified; however, relating this pore scale behavior to the assemblage (e.g., column) scale is complicated by multiple possible outcomes at the assemblage scale such as near-surface colloid reentrainment into the bulk fluid at rear flow stagnation zones on grains, or direct grain-to-grain transfer of near-surface colloids, or colloid diffusion out of secondary minima.[32]

Based on the fact that colloid concentrations observed during extended tailing tend to be orders of magnitude smaller than those observed under steady state breakthrough[33–35] the slow moving colloids in porous media maybe a small fraction of the attached colloids. Indeed, integrating the concentration history of the packed column effluent shows that the total number of colloids eluted during extended tailing (5 pore volumes following the first pore volume of elution) ranges from 0.4 to 0.7% of retained colloids in an array of experiments involving carboxylate-modified microspheres and glass beads.[8, 36] The data suggest that attachment is the predominant retention mechanism in porous media and that it is therefore reasonable to compare predictions from the discrete heterogeneity model for attachment in the impinging jet to semiempirical expressions for retention in porous media.

In contrast to porous media, impinging jets lack a defined porosity. We developed an algorithm to define a fluid subdomain in the impinging jet system to allow direct comparison of attachment parameters (e.g., $\eta$) among the two systems. The algorithm boils down to determining the superficial velocity in the Happel cell (porous media) that produces an equivalent fluid flow field to the impinging jet. We have proven that the algorithm produces equivalent prediction of $\eta$ between the two systems for favorable conditions. This algorithm is presented, and results for favorable conditions are given, in Appendix C. For the examined average jet fluid velocities (148 and 513 $mday^{-1}$); the equivalent average pore water velocities ($v_{pore}$) (1.9 and 8.2 $mday^{-1}$) were calculated for an arbitrary collector size (510 μm in diameter) and random packed porosity (0.378) according to the protocol provided in Appendix C.

## Results

### *Correlation equation for unfavorable conditions*

Based on the results described below we propose the following mechanistically-based correlation for predicting $\alpha$ under unfavorable conditions involving negatively charged colloids and silica surfaces:

$$\alpha = 0.2[(\alpha_{2min})^{0.3}(N_{col})^{0.5}] \qquad (4.7)$$

where the dimensionless parameters $N_{col}$ and $\alpha_{2min}$ are defined in equations 1b and 3a above.

The above correlation equation produces the lowest mean square log residual ($MSR_{log}$) for predicted versus experimental $\alpha$ for data from both impinging jet and porous media experiments over a large range of colloid sizes (60 nm to 3.1 μm), fluid velocities

(1.9 to 588 $mday^{-1}$), solution IS (0.1–300 mM), as well as grain size of uniform media (200 to 510 μm) (Figure 4.1). Whereas equation 4.7 represents a large range of colloid sizes, IS, and fluid velocities, the vast majority of existing experiments concern deposition of carboxylate-modified polystyrene latex microspheres on soda-lime glass collectors at circumneutral pH; therefore, the applicability of equation 7 (and the other existing correlations) to other pH conditions and other unfavorable surfaces has yet to be tested. The discrete heterogeneity-based equation 4.7 is unique in that it provides a mechanistic basis for extension to pH conditions and other unfavorable surfaces via the leading coefficient that represents surface coverage by heterodomains, as described in the Discussion section below.

*Prediction of $\alpha$ in impinging jet geometry*

Experimental values of $\alpha$ in the impinging jet (Figure 4.2) are relatively independent of colloid size, indicating that the physicochemistry of mass transfer from the near surface to the surface (attachment) is not strongly size-dependent. This is in contrast to the physics of mass-transfer from the bulk to the near-surface fluid domains ($\eta$), which shows significant size dependence (e.g., experiments reported by Pazmino et al.[27]). However, it would be inaccurate to ascribe all of the transport physics to $\eta$ since while there is no dependence of $\alpha$ on fluid velocity for silica slide E, there is a clear dependence for silica slide B (Figure 4.2 compare right-most to middle). Slide B and E are two representative glass microscope slides from among the same lot.[27] The reason for this discrepancy is not known, but may be related to differences in roughness or other surface properties between the two slides, which is an issue of further investigation. The

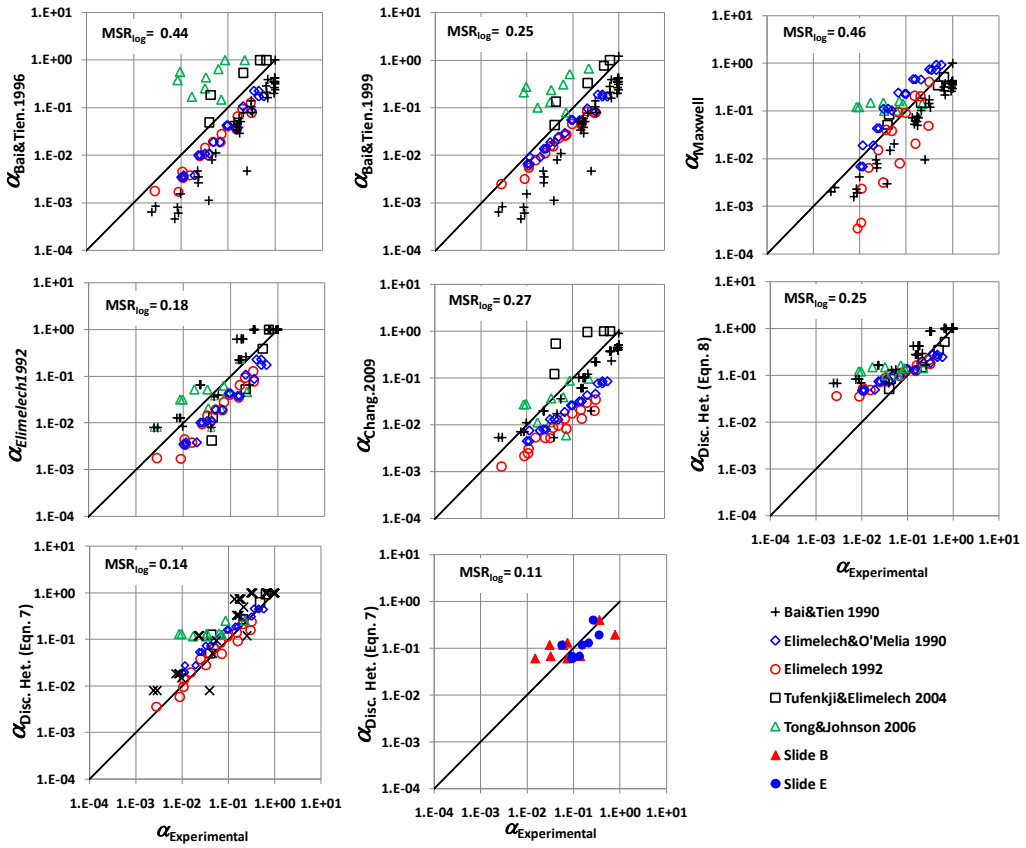


Figure 4.1 Predicted collision efficiency from the existing correlation equations for unfavorable conditions[9, 10, 12–14] and the proposed one parameter discrete heterogeneity correlation equations 4.7 and 4.8 for soda-lime glass. Experimental data provided from each corresponding reference. Slide B and E correspond to the experiments utilized to characterize the discrete heterogeneity of soda-lime glass reported by Pazmino et al.[27]

inverse dependence of $\alpha$ on fluid velocity has been also observed in porous media from several other studies.[8, 37–41]

The mechanistically-based Maxwell prediction of $\alpha$, which equates retention in the near-surface fluid domain to attachment, is generally in the correct range. However, it incorrectly predicts increased retention with increased colloid size across the size range examined here (Figure 4.2). Secondary minimum interactions also underlie colloid behavior in the near-surface fluid domain in the discrete heterogeneity simulations. However, the latter includes a mechanism of colloid attachment (immobilization), which

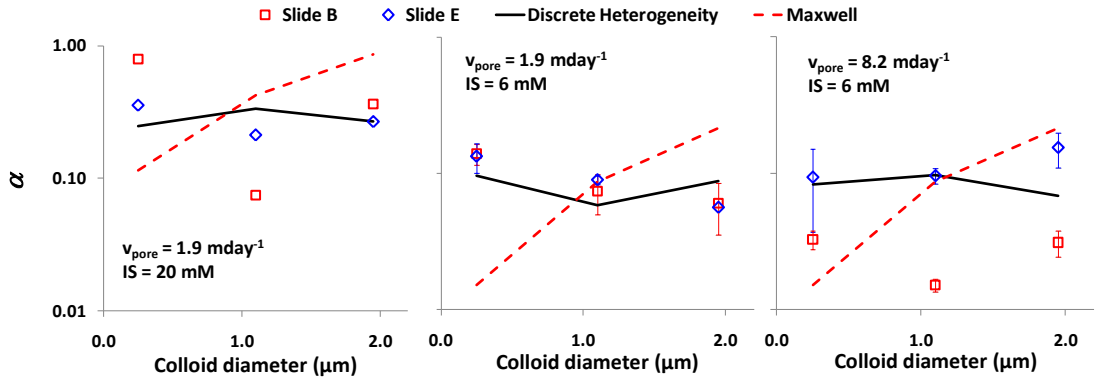


Figure 4.2 Experimental (symbols) and simulated (solid lines) collision efficiency for three experimental conditions. Experimental values correspond to deposition experiments on two characteristic soda-lime glass slides from Pazmino et al.[27] Dashed lines correspond to predicted values according to the Maxwell distribution approach. Surface heterogeneity utilized in simulations corresponds to 120 and 60 nm-radii heterodomains in 1:4 number ratio at a surface coverage of 0.04%.

when combined with the power-law size distribution of heterodomains (multitude of small relative to large heterodomains) predicts greater attachment of 0.25 μm colloids and lesser attachment of the 1.95 μm colloids, relative to the Maxwell prediction[27] (Figure 4.2).

All four semiempirical expressions predict a significant influence of colloid size on $\alpha$ (Figure 4.3). Three of the expressions[10, 12, 13] predict a maximum $\alpha$ corresponding to the 1 μm colloid size, whereas one[9] predicts a minimum $\alpha$ corresponding to that colloid size. The much stronger dependence of $\alpha$ on colloid size in the Bai and Tien[10, 12] expressions results from the strong sensitivity to bulk surface $\zeta$-potentials via their power law dependence in the expressions. In contrast, the discrete heterogeneity model simulations reflect a relatively minor influence of $\alpha$ with colloid size, which is characteristic of the experimental trend (Figure 4.3).

To compare the performance of the discrete heterogeneity model across the larger

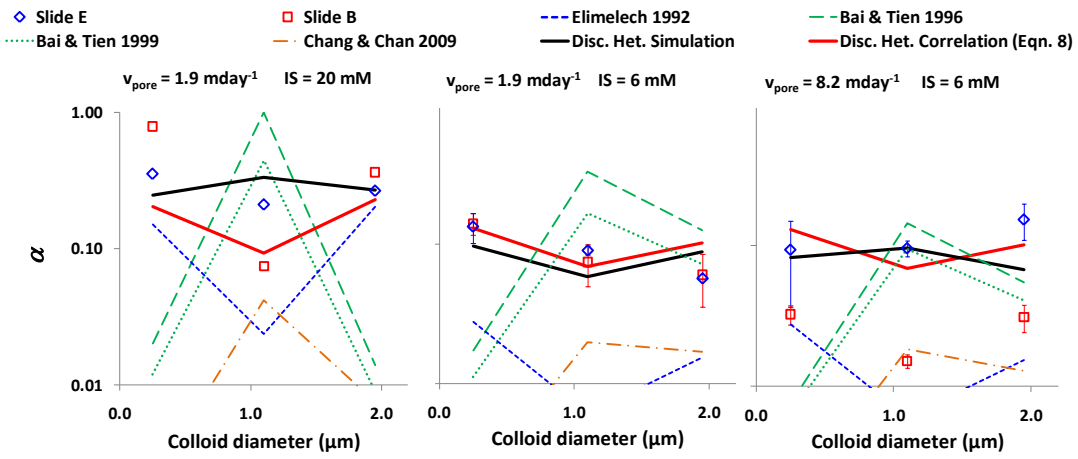


Figure 4.3 Comparison of predicted collision efficiency ($\alpha$) for the discrete heterogeneity correlation equation (red solid line), discrete heterogeneity trajectory simulations results (black solid line), and semiempirical correlation equations form the literature[9,10,12,13] (dashed lines). Experimental results (symbols) correspond to two soda-lime glass slides.[27]

range of conditions from which the porous media-based semiempirical correlations were derived, we developed a correlation equation matching the mechanistic impinging jet simulations. Following the principle of parsimony, we started the development of our heuristic from equation 1a, which is the simplest of the existing correlation equations.

In equation 4.1b, the parameter $N_{col}$ represents the ratio of mean-field attractive versus repulsive interactions. The attractive term (Hamaker constant) in the numerator of equation 4.1b represents van der Waals attraction, which is the only mean-field attractive force since electric double layer attraction is absent for a mean-field repulsive surface. The repulsive term in the denominator of equation 4.1b is the product of the range ($\kappa^{-1}$) and the scaling factor ($\varepsilon_r\varepsilon_o\zeta_p\zeta_c$), of the repulsive force.[9]

The best fit to the jet experiment data using equation 1a is shown in Figure 4.2, resulting in the following equation:

$$\alpha = 0.11(N_{col})^{0.5} \qquad (4.8)$$

The equation produces a mild dependence on colloid size, with minimum $\alpha$ corresponding to the 1.1 μm colloid size that is characteristic of the impinging jet data (Figure 4.3).

Because goodness of a prediction has traditionally been displayed in 1:1 plots of predicted versus experimental values, we also cast the results in that format (Figure 4.4). This figure reveals that the $MSR_{log}$ was the lowest for the discrete heterogeneity correlation (0.11) (equation 4.8), followed by the Maxwell approach[14] (0.38), and Elimelech[9] (0.53). It should be noted that the $\alpha$ values were first transformed to log scale before determining residuals in order to equally represent under and over prediction.

*Prediction of $\alpha$ in porous media*

In order to test the generality of the proposed heuristic, the comparison was extended to packed column experiment results from several studies[7, 9, 10, 12] as summarized by Bai and Tien[12] and Chang et al.[13] The comparison included column experiments for carboxylate-modified polystyrene latex microspheres ranging in size (diameter) from 0.05 to 3.1 μm, average pore water velocities ranging from 4 to 588 $mday^{-1}$, and IS ranging from 0.1 to 300 mM. Because we expect the leading coefficient in the correlation equation to be related to the surface coverage by discrete heterogeneity (further described below), we limit the comparison to silica-based collectors (e.g., soda-lime glass) and near neutral pH (6.7–7.0), which also happens to be the conditions corresponding to the vast majority of data for which detailed parameters are reported. Because correlation equations may predict $\alpha$ values greater than unity when applied to a much broader range of conditions relative to the experimental data from which they were developed, all correlation equations were therefore bounded by a maximum $\alpha$ equal to

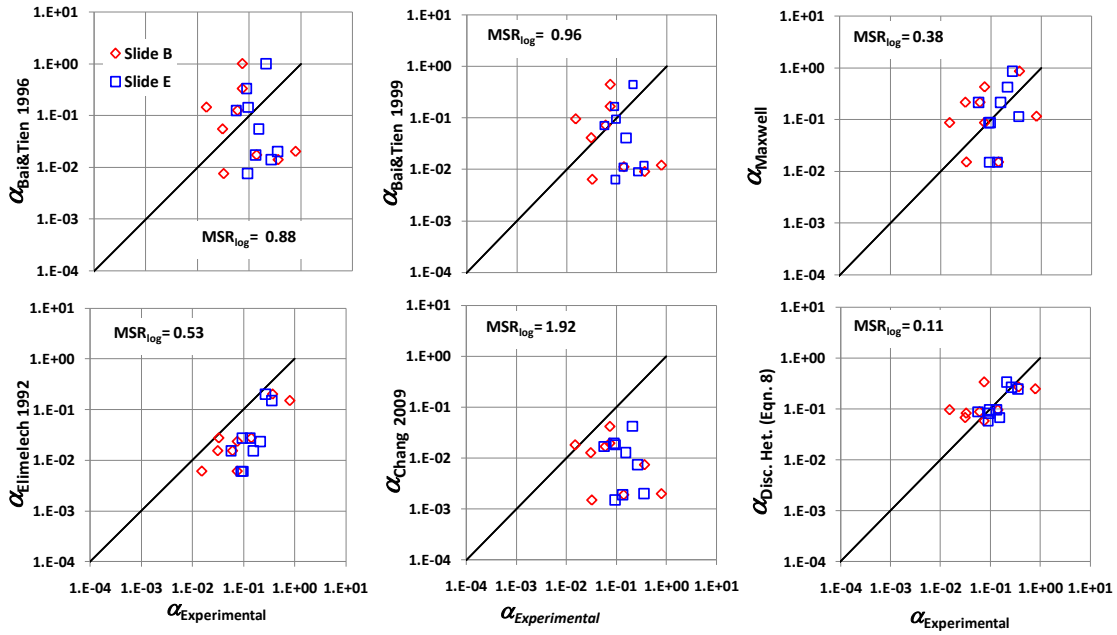


Figure 4.4 Comparison of predicted collision efficiency from the existing correlation equations[9, 10, 12–14] and proposed discrete heterogeneity heuristic equation with results for retention experiments on soda-lime glass slides (B and E) reported in Pazmino et al.

unity in order to conduct a fair comparison.

Application of equation 8 to the set of porous media experimental conditions shows that it performs similarly to the set of semiempirical correlations developed from that data, with $MSR_{log}$ values ranging 0.25 to 0.5 (unbounded) and from 0.18 to 0.44 (bounded) for the semiempirical expressions, and $MSR_{log}$ equal to 0.26 (unbounded) and 0.25 (bounded) for the discrete heterogeneity correlation.

This is a very promising result considering that the discrete heterogeneity expression was developed from a subset range of colloid sizes (0.25–1.95 μm), fluid velocities (1.9–8.2 $mday^{-1}$), and ionic strengths (6–20 mM) relative to the much broader range of experimental conditions.

However, the correlation provided above (equation 4.8) consistently

overpredicted experimental values of $\alpha$ that were relatively low (e.g., < 0.1), which are reflective of low IS experimental conditions. Since the term $N_{col}$ represents the balance of attractive versus repulsive energies associated with the primary minimum and repulsive energy barrier, the correlation does not represent the persistence of colloids in the near surface due to the influence of secondary minima. As such, the correlation in equation 8 is unable to capture the influence of colloid near-surface residence time via secondary minimum interaction under low IS conditions. Addition of the Maxwell term ($\alpha_{2min}$) reflects the influence of near-surface residence time and yields the final equation (4.7) that provides the best overall porous media data (n = 91) (MSRlog = 0.14) (Figure 4.1).

## Discussion

### *Inclusion of Maxwell approach term*

Further justification of inclusion of $\alpha_{2min}$ in the correlation is provided by the discrete heterogeneity simulations. Simulated colloid trajectories in the near surface fluid domain under low IS unfavorable conditions (Figure 4.5) demonstrate the influence of near-surface residence times in determining the likelihood of colloids finding attractive heterodomains. The plan view of representative trajectories of 0.25 and 1.95 μm colloids near a flat surface (Figure 4.5 top) show that the 0.25 μm colloid (red trajectory) scans a much larger collector area, thereby allowing them to "assay" greater areas of the surface. In contrast, the cross-sectional view (Figure 4.5 bottom) shows that persistence of colloids in the near surface fluid domain (via secondary minimum interactions) is reduced for 0.25 relative to 1.95 μm colloids. The reduced persistence of smaller colloids in the near-surface fluid domain is also reflected in the corresponding average residence times for each visit to the near surface (defined as separation distance, H < 200 nm), which

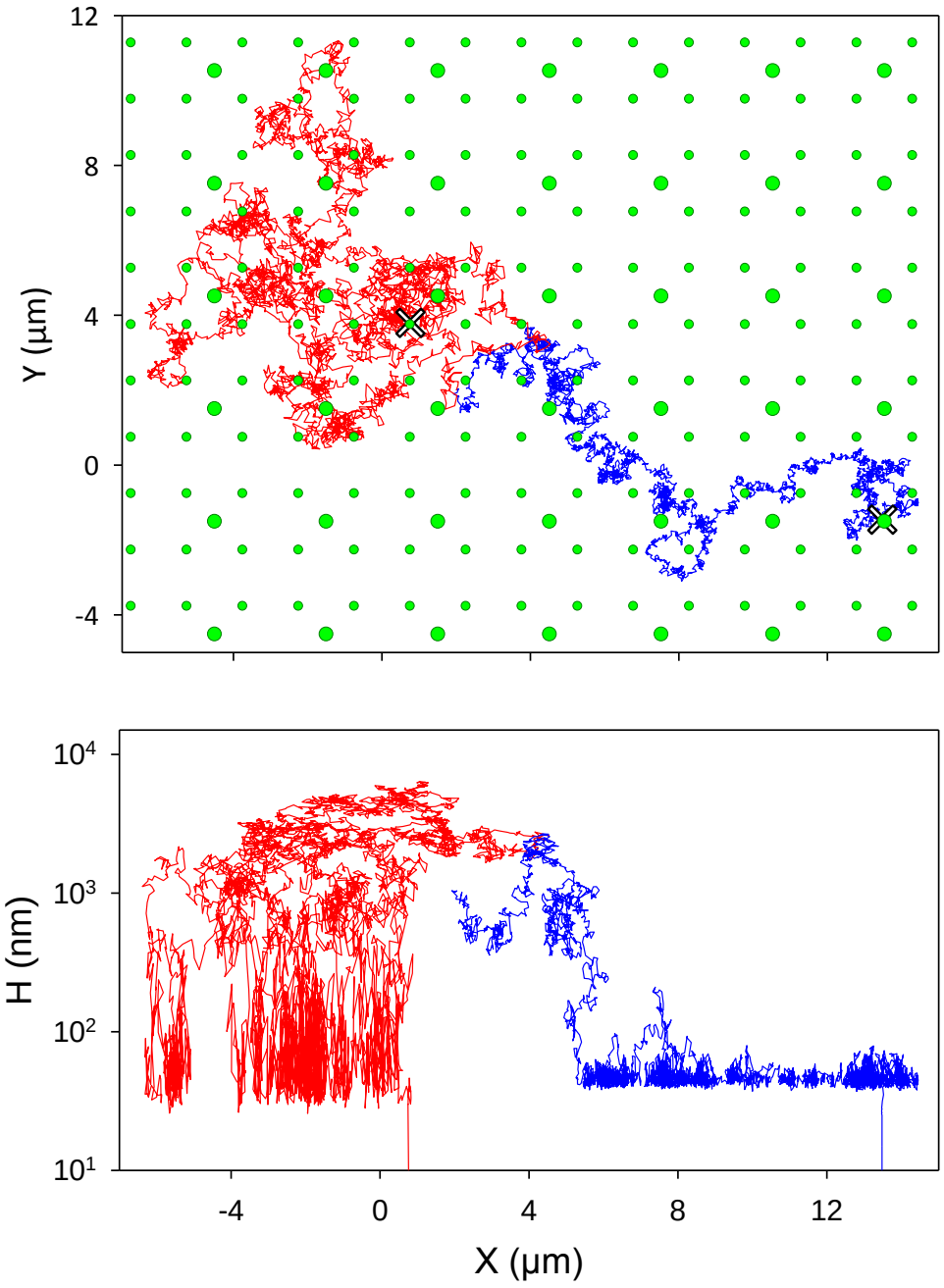


Figure 4.5. Representative trajectories of 0.25 (red) and 1.95 (blue) µm colloids. Top panel: plan view of trajectories over a 20µm-radius observation area. Green circles represent heterodomains (120 and 60 nm radii). Heterodomain size is exaggerated for presentations purposes. The cross symbols represent the attachment locations. Bottom panel: normal view of the respective trajectories. H is the minimum separation distance from the collector surface. Heterogeneity corresponds to power-law distribution of 120 and 60-nm radii, 1:4 number ratio at 1% surface coverage. Vjet = $1.7 \times 10^{-3}$ $ms^{-1}$, IS = 6 mM.

were 3.06, 32.05, and 34.7 seconds for the 0.25, 1.1, and 1.95 μm colloids, respectively (Appendix C). The persistence of colloids in the near-surface fluid domain influences the likelihood of attachment. This effect is reflected in equation 4.7 by inclusion of the Maxwell term ($\alpha_{2min}$).

*Attachment beyond 2-μm size colloids*

We note that the correlation is not representative of colloids larger than a few μm in diameter. Direct observation experiments in the impinging jet for attachment of 4.4 μm microspheres on silica at 6 mM IS and fluid velocities at the low end of the range (8.2 and 1.9 $mday^{-1}$) yielded $\alpha$ values close to favorable, ranging from 0.49 to 0.65, respectively (Appendix C).

These results contrast with the expected highly unfavorable conditions, as indicated by measured colloid zeta potential (-52 mV), which yields a repulsive energy barrier of $11.7x10^3$ kT. These experimental results are consistent with column experiments reported by Vaidyanathan and Tien[11] for (6.1 and 11.4 μm colloids) with average $\alpha$ equal to 0.64 within a range from 0.2 to 1 for IS conditions ranging from 10 to 180 mM, respectively.

In contrast, discrete heterogeneity simulations (again using power-law distributed 60 and 120-nm radius heterodomains at 0.04% surface coverage) predicted zero attachment of 4.36 μm colloids, indicating that additional factors govern attachment of these larger particles and that these factors are not well represented by discrete attractive zones as rendered to date.

An independent indicator of additional (nonelectrostatic) factors governing attachment of larger particles is provided by impinging jet experiments examining

attachment of 2-μm diameter carboxylate-modified polystyrene latex microspheres.

Their attachment was greatly enhanced by stoppage of flow for 10 hours to allow settling to bring colloids into proximity of the surface, and this attachment held even when flow was resumed (unpublished data), suggesting that a kinetically-limited process operated to increase adhesion upon settling-driven contact of the colloid with the surface. The results above strongly suggest a role of settling and deformation onto surface asperities (roughness) for larger colloids, which enhances the area of contact. Since roughness and kinetic colloid deformation are implicated in attachment of larger colloids, the experimental results of Vaidyanathan and Tien,[11] which correspond to 6.1 and 11.4 μm colloids, were not included in the above comparisons.

Explicit representation of surface roughness at the nanoscale in mechanistic simulations is likely intractable due to numerical intensity of nanoscale modification of the flow field relative to the scale of a collector. Our findings suggest that future work should include roughness and kinetic colloid deformation in representative discrete heterogeneity simulation of attachment of larger colloids. Notably, the discrete heterogeneity representation that quantitatively predicted colloid attachment[27] also qualitatively predicted colloid reentrainment in response to flow and IS perturbations,[28] and we anticipate improved quantitative prediction of colloid release in response to perturbations via inclusion of roughness and kinetic colloid deformation in the discrete heterogeneity approach.

Possibly related to roughness is the issue that colloid retention shows a dependence on fluid velocity in impinging jet versus porous media. Tong and Johnson[8] reported a much stronger decrease in $\alpha$ with fluid velocity in jet experiments relative to

porous media. These results are consistent with a single experiment at 300 $mday^{-1}$ and 6 mM IS for the 1.95 μm colloids, which showed no attachment in the jet, while experiments reported by Bai and Tien[12] for similar conditions, 366 $mday^{-1}$ and 10 mM IS, for 3.1 μm colloids verified attachment in the porous media. There is not a definitive explanation for this discrepancy; however, increased roughness of glass beads relative to glass slides and differences in the flow field between the two geometries (e.g., rear stagnation zones, grain-to-grain contacts, and potential vorticity exist in the porous media flow field) may enhance attachment in the porous media relative to the jet at higher flow regimes. The potential influence of roughness is consistent with measurements of mean square height (RMS) values of asperities reported in the literature ranging from 15 to 38 nm for glass beads[42] and approximately 4 nm for glass slides.[43] Differences in roughness may also account for the different dependencies of $\alpha$ on fluid velocity between slides B and E (Figure 4.2); i.e., the greater dependence on fluid velocity observed for slide B may reflect a smoother surface on that slide. The difference in roughness between surfaces is out of the scope of this study and warrants further examination.

*Discrete heterogeneity approach to represent other unfavorable aquifer-relevant surfaces*

This study demonstrated that a correlation equation developed from representative surface heterogeneity extracted via comparison of simulations to experiments on soda-lime glass in impinging jet systems (equation 4.8) matched well the observed colloid retention in soda-lime glass porous media across a much broader range of colloid sizes, IS, and fluid velocity conditions at circumneutral pH. The correlation prediction for the broader set of experiments was improved by inclusion of a Maxwell term to represent

colloid persistence in the near-surface domain as mediated by secondary minimum interaction (equation 4.7). The coefficient 0.11 used in equation 8 to match carboxylate-modified polystyrene latex colloid collision efficiency on soda-lime glass slides in the impinging jet at pH 6.7 reported by Pazmino et al.[27] was modified slightly to 0.2 to carboxylate-modified polystyrene latex collision efficiencies on both soda-lime glass slides (impinging jet) and soda-lime glass beads (porous media) at circumneutral pH (equation 4.7).

We anticipate that other pH ranges and other unfavorable surfaces will yield significantly different values of surface coverage (mechanistic simulations) and leading coefficient (corresponding correlations). The leading coefficient in the impinging jet correlation (equation 4.8) is directly related to surface coverage by discrete heterogeneity, as demonstrated by the sensitivity of $\alpha$ to heterodomain surface coverage (SC) in the mechanistic trajectory simulations (Figure 4.6, black solid lines) and the corresponding sensitivity of the leading coefficient in the correlation (Figure 4.6, red dashed lines) for an exemplary experimental condition (6 mM IS, average pore water velocity 1.9 $mday^{-1}$ and pH 6.7). Across the range of experiments, $\alpha$ ranges from 0.02 to 0.41 (Figure 4.6, left), and the surface coverage by heterodomains and the leading coefficient in the correlation correspondingly range from 0.01% to 0.16% and 0.06 to 0.75, respectively (Figure 4.6, right). We anticipate that the surface coverage (and possibly heterodomain size distribution) in mechanistic simulations, as well as the leading coefficient (and possibly powers on dimensionless terms) in corresponding correlations, will show useful trends with pH on other (nonglass) unfavorable environmental surfaces (e.g., quartz,

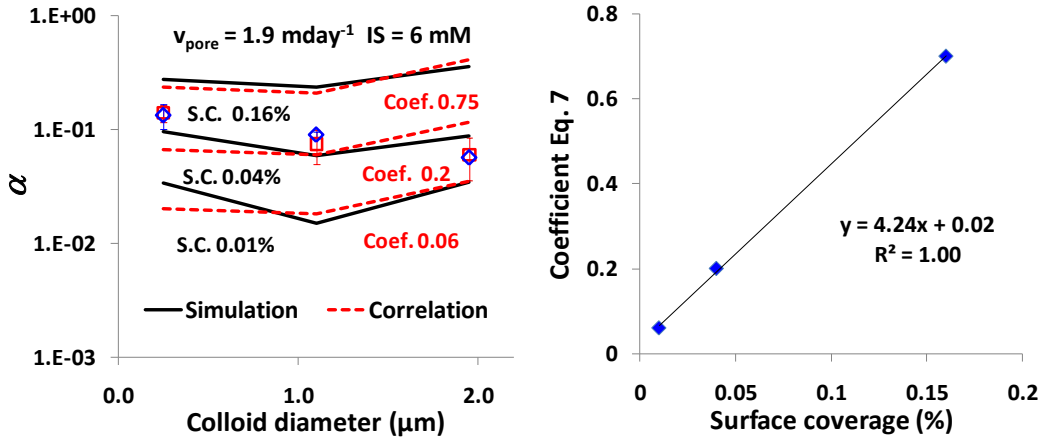


Figure 4.6 Collector efficiency simulations for different surfaces. Left: Simulations (solid lines) results for different surface coverages and same Power-law heterodomain size distribution (120–60 nm radii, 1:4 number ratio). Corresponding correlation equation predictions (dashed lines) for different leading coefficient values in equation 7. Discrete symbols correspond to soda-lime glass slides experiments at pH 6.72 reported in Pazmino et al.[27] Right: Equation 7 coefficient values correlation with surface coverage.

feldspars, micas), and such work is ongoing.

The discrete heterogeneity approach for predicting $\alpha$ under unfavorable conditions is uniquely based on mechanistic prediction of colloid attachment under conditions of bulk repulsion. Its utility is demonstrated above for prediction of CML colloid retention on glass surfaces. Future work will determine whether representative heterogeneities can be developed for other (nonglass and non-CML) unfavorable surfaces in order to greatly extend predictive capabilities.

## References

(1) Hiscock, K. M.; Grischek, T. Attenuation of Groundwater Pollution by Bank Filtration. *J. Hydrology* **2002,** *266* (3), 139–144.

(2) Tufenkji, N.; Ryan, J. N.; Elimelech, M. Peer Reviewed: The Promise of Bank Filtration. *Environ. Sci. Technol.* **2002,** *36* (21), 422A–428A.

(3) Zhang, W.X. Nanoscale Iron Particles for Environmental Remediation: An Overview. *J. Nanopart. Res.* **2003,** *5* (3-4), 323–332.

(4) Kretzschmar, R.; Borkovec, M.; Grolimund, D.; Elimelech, M. Mobile Subsurface Colloids and their Role in Contaminant Transport. *Adv. Agron.* **1999,** *66,* 121–193.

(5) Borchardt, M. A.; Bertz, P. D.; Spencer, S. K.; Battigelli, D. A. Incidence of Enteric Viruses in Groundwater from Household Wells in Wisconsin. *Appl. Environ. Microbiol.* **2003,** *69* (2), 1172–1180.

(6) Adamczyk, Z.; Dabros, T.; Czarnecki, J.; van de Ven, T. G. M. Particle Transfer to Solid Surfaces. *Adv. Colloid Interface Sci.* **1983,** *19* (3), 183–252.

(7) Elimelech, M.; O'Melia, C. R. Effect of Particle Size on Collision Efficiency in the Deposition of Brownian Particles with Electrostatic Energy Barriers. *Langmuir* **1990,** *6* (6), 1153–1153.

(8) Tong, M.; Johnson, W. P., Excess Colloid Retention in Porous Media as a Function of Colloid Size, Fluid Velocity, and Grain Angularity. *Environ. Sci. Technol.* **2006,** *40* (24), 7725–7731.

(9) Elimelech, M. Predicting Collision Efficiencies of Colloidal Particles in Porous Media. *Water Res.* **1992,** *26* (1), 1–8.

(10) Bai, R.; Tien, C. A New Correlation for the Initial Filter Coefficient under Unfavorable Surface Interactions. *J. Colloid Interface Sci.* **1996,** *179*, 631–634.

(11) Vaidyanathan, R.; Tien, C. Hydrosol Deposition in Granular Media under Unfavorable Surface Conditions. *Chem. Eng. Sci.* **1991,** *46* (4), 967–983.

(12) Bai, R. B.; Tien, C. Particle Deposition under Unfavorable Surface Interactions. *J. Colloid Interface Sci.***1999,** *218* (2), 488–499. 25

(13) Chang, Y.I.; Cheng, W.Y.; Chan, H.C. A Proposed Correlation Equation for Predicting Filter Coefficient under Unfavorable Deposition Conditions. *Separation and Purification Technology* **2009,** *65* (3), 248–250.

(14) Hahn, M. W.; O'Melia, C. R. Deposition and Reentrainment of Brownian Particles in Porous Media under Unfavorable Chemical Conditions: Some Concepts and Applications. *Environ. Sci. Technol.***2004,** *38* (1), 210–220.

(15) Kubo, R. The Fluctuation-dissipation Theorem. *Rep. Prog. Phys.* **1966,** *29* (1), 255.

(16) McDowell-Boyer, L. M. Chemical Mobilization of Micron-sized Particles in Saturated Porous Media under Steady Flow Conditions. *Environ. Sci. Technol.* **1992,** *26* (3), 586–593.

(17) Shen, C.; Li, B.; Huang, Y.; Jin, Y. Kinetics of Coupled Primary- and Secondary-minimum Deposition of Colloids under Unfavorable Chemical Conditions. *Environ. Sci. Technol.* **2007,** *41* (20), 6976–6982.

(18) Johnson, W. P.; Li, X.; Tong, M.; Ma, H. Comment on "Transport and Fate of Bacteria in Porous Media: Coupled Effects of Chemical Conditions and Pore Space Geometry" by Saeed Torkzaban et al. *Water Resour. Res.* **2009,** *45* (9). W09603.

(19) Auset, M.; Keller, A. A. Pore-scale Visualization of Colloid Straining and Filtration in Saturated Porous Media using Micromodels. *Water Resour. Res.* **2006,** *42* (12). W12S02.

(20) Johnson, W. P.; Pazmino, E.; Ma, H. Direct Observations of Colloid Retention in Granular Media in the Presence of Energy Barriers, and Implications for Inferred Mechanisms from Indirect Observations. *Water Res.* **2010,** *44* (4), 1158–1169.

(21) Bhattacharjee, S.; Chun-Han, K.; Elimelech, M. DLVO Interaction between Rough Surfaces. *Langmuir* **1998,** *14* (12), 3365–3375.

(22) Hoek, E. M. V.; Agarwal, G. K. Extended DLVO Interactions between Spherical Particles and Rough Surfaces. *J. Colloid Interface Sci.* **2006,** *298* (1), 50–58.

(23) Duffadar, R. D.; Davis, J. M. Interaction of Micrometer-scale Particles with Nanotextured Surfaces in Shear Flow. *J. Colloid Interface Sci.* **2007,** *308* (1), 20–29.

(24) Duffadar, R. D.; Davis, J. M. Dynamic Adhesion Behavior of Micrometer-scale Particles Flowing over Patchy Surfaces with Nanoscale Electrostatic Heterogeneity. *J. Colloid Interface Sci.* **2008,** *326* (1), 18–27.

(25) Ma, H.; Pazmino, E.; Johnson, W. P. Surface Heterogeneity on Hemispheres-in-cell Model Yields all Experimentally-observed Non-straining Colloid Retention Mechanisms in Porous Media in the Presence of Energy Barriers. *Langmuir* **2011,** *27* (24), 14982–14994.

(26) Bendersky, M.; Davis, J. M. DLVO Interaction of Colloidal Particles with Topographically and Chemically Heterogeneous Surfaces. *J. Colloid Interface Sci.* **2011,** *353* (1), 87–97.

(27) Pazmino, E.; Trauscht, J.; Dame, B.; Johnson, W. P. Power Law Size-Distributed Heterogeneity Explains Colloid Retention on Soda Lime Glass in the Presence of Energy Barriers. *Langmuir* **2014,** *30* (19), 5412–5421.

(28) Pazmino, E.; Trauscht, J.; Johnson, W. P. Release of Colloids from Primary Minimum Contact under Unfavorable Conditions by Perturbations in Ionic

Strength and Flow Rate. *Environ. Sci. Technol.* **2014,** *48* (16), 9227–9235

(29) Duffadar, R.; Kalasin, S.; Davis, J. M.; Santore, M. M. The Impact of Nanoscale Chemical Features on Micron-scale Adhesion: Crossover from Heterogeneity-dominated to Mean-field Behavior. *J. Colloid Interface Sci.* **2009,** *337* (2), 396–407.

(30) Einstein, A. Investigation on the Theory of the Brownian Movement. *Ann. der Physik* **1905**. *322* (8), 549–560.

(31) Rajagopalan, R.; Tien, C. Trajectory Analysis of Deep-bed Filtration with the Sphere-in-cell Porous Media Model. *AIChE J.* **1976,** *22* (3), 523–533.

(32) William, P. J.; Markus, H. Upscaling Colloid Transport and Retention under Unfavorable Conditions: Linking Mass Transfer to Pore and Grain Topology. *Water Resour. Res.* **2013,** *49* (9), 5328–5341.

(33) Johnson, W. P.; Blue, K. A.; Logan, B. E.; Arnold, R. G. Modeling Bacterial Detachment During Transport Through Porous Media as a Residence-Time-Dependent Process. *Water Resour. Res.* **1995,** *31* (11), 2649–2658.

(34) Ginn, T. R. On the Distribution of Multicomponent Mixtures over Generalized Exposure Time in Subsurface Flow and Reactive Transport: Foundations, and Formulations for Groundwater Age, Chemical Heterogeneity, and Biodegradation. *Water Resour. Res.* **1999,** *35* (5), 1395–140

(35) Ginn, T. R. On the Distribution of Multicomponent Mixtures over Generalized Exposure Time in Subsurface Flow and Reactive Transport: Theory and Formulations for Residence-time-dependent Sorption/Desorption with Memory. *Water Resour. Res.* **2000,** *36* (10), 2885–2893.

(36) Li, X.; Scheibe, T. D.; Johnson, W. P. Apparent Decreases in Colloid Deposition Rate Coefficients with Distance of Transport under Unfavorable Deposition Conditions: A General Phenomenon. *Environ. Sci. Technol.* **2004,** *38* (21), 5616–5625.

(37) Keller, A. A.; Sirivithayapakorn, S.; Chrysikopoulos, C. V. Early Breakthrough of Colloids and Bacteriophage MS2 in a Water-saturated Sand Column. *Water Resour. Res.* **2004,** *40* (8), W083041–W0830411.

(38) Li, X.; Zhang, P.; Lin, C. L.; Johnson, W. P., Role of Hydrodynamic Drag on Microsphere Deposition and Reentrainment in Porous Media under Unfavorable Conditions. *Environ. Sci. Technol.* **2005,** *39* (11), 4012–4020.

(39) Tong, M.; Camesano, T. A.; Johnson, W. P. Spatial Variation in Deposition Rate

Coefficients of an Adhesion-deficient Bacterial Strain in Quartz Sand. *Environ. Sci. Technol.* **2005,** *39* (10), 3679–3687.

(40) Tong, M.; Li, X.; Brow, C. N.; Johnson, W. P., Detachment-influenced Transport of an Adhesion-deficient Bacterial Strain within Water-reactive Porous Media. *Environ. Sci. Technol.* **2005,** *39* (8), 2500–2508.

(41) Johnson, W. P.; Li, X.; Assemi, S. Deposition and Reentrainment Dynamics of Microbes and Non-biological Colloids during Non-perturbed Transport in Porous Media in the Presence of an Energy Barrier to deposition. *Adv. Water Resour.* **2007,** *30* (6-7), 1432–1454.

(42) Shellenberger, K.; Logan, B. E. Effect of Molecular Scale Roughness of Glass Beads on Colloidal and Bacterial Deposition. *Environ. Sci. Technol.* **2002,** *36* (2), 184–189.

(43) Ren, J.; Ganapathysubramanian, B.; Sundararajan, S. Experimental Analysis of the Surface Roughness Evolution of Etched Glass for Micro/Nanofluidic Devices. *J. Micromech. Microeng.* **2011,** *21* (2), 025012.

# CHAPTER 5

# CONCLUSIONS

The results presented in this work indicate that nanoscale discrete heterogeneity explains colloid attachment and detachment directly observed at the pore scale (impinging jet) and provides the basis to understand the mechanisms of attachment in the porous media.

The discrete heterogeneity trajectory model is able to extract heterodomain characteristic from a small set of experiments varying colloid size, ionic strength (IS), and fluid velocity. It was determined that a Pareto power-law distribution of 60 and 120 nm radii heterodomains law distribution of heterodomains is able to quantitatively capture experimental trends for all conditions examined. The reason for this heterodomain size distribution is that, contrasting to favorable conditions, enhanced diffusion of small colloids (0.25 μm) reduces attachment relative to larger colloids (1.95 μm) due to shorter persistence in the near surface fluid domain (secondary minimum), and therefore many more small heterodomains that capture 0.25 μm colloids are required to match experimental results.

Additionally, the power-law distribution of heterodomains was able to qualitatively capture experimental trends of fractional release of a colloid population in response to reduced IS or increased flow perturbations and provided the mechanism of colloid release from contact (primary minimum) when steric interactions are considered.

Under lower IS, the collector surface becomes more repulsive due to longer-range electrostatic interactions. This increased range increases the colloid-collector zone of interaction and reduces the favorable contribution of the heterodomain to the net interaction, potentially releasing the colloid. Similarly, colloid release occurs if the heterodomain favorable contribution is not sufficient to overcome the increased driving torque at higher fluid conditions. The fractional release arises from a distribution of adhesive torque for a population of colloids attached over heterodomains.

A correlation equation based in the colloidal number that represents attractive energy (van der Waals interactions) relative to repulsive energy (electric double layer interactions) is able to capture the discrete heterogeneity simulation trends for collision efficiency ($\alpha$) in the impinging jet system. Notably, the sensitivity analysis of surface coverage of the same power-law size distributed heterodomains with collision efficiency indicates that the correlation equation scales linearly with surface coverage. This finding suggests that different minerals may be represented by the same power-law distribution and justifies the mechanistic basis of the proposed correlation. More notably, the correlation equation developed from a small set of jet experiments performs similarly to existing correlations when compared with numerous porous media experiments for a broad range of conditions. Analysis of trajectories indicates that the persistence of colloids in the secondary minimum is well represented by the Maxwell distribution of kinetic energy for a population of colloids. Inclusion of the Maxwell term ($\alpha_{2min}$) in the correlation equation increased the porous media comparison by a factor of 2 without affecting the predictive performance for the impinging jet experiments.

# APPENDIX A

# SUPPORTING INFORMATION FOR CHAPTER 2

## Impinging Jet Geometry

The impinging jet system utilized in the experiments is shown in schematic form in Figure A.1. Colloids are injected across the jet exit (blue circle), and attachment is verified over the collector surface across the area of observation (gray circle). In the simulations, colloids are injected only across a reduced area in the jet (red circle). Calculation of collector efficiency for both experiments and simulations is shown in the text.

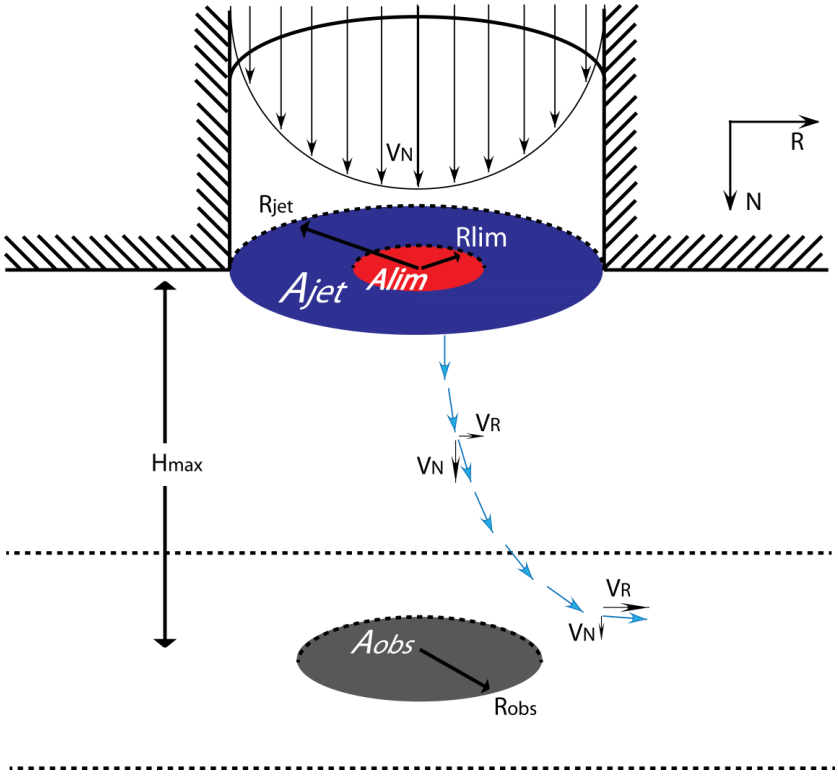


Figure A.1. Impinging jet system schematic. $R_{jet}$ is the jet radius, and $R_{lim}$ is the limiting trajectory injection radius used to inject particles in the simulations. $A_{jet}$ (blue) and $A_{lim}$ (red) are the corresponding cross-sectional areas. $R_{obs}$ is the radius of the area of observation, $A_{obs}$, shown in gray on the collector surface. $V_N$ correspond to the fluid velocity profile inside the jet, $V_R$ is the radial component of fluid velocity in the chamber, and $H_{max}$ is the separation distance between the jet exit plane and the impinging surface.

## Experimental Deposition Slopes

Colloid attachment was quantified by counting of particles deposited across the observation area during injection. The initial time was adjusted to fit the intersection of the linear equation to the origin. Counting was realized by postprocessing of the image stack via open source software (ImageJ). Figure A.2 shows a representative slope of deposition. Linearity of the slope denotes that neither blocking nor ripening occurred during the experiment.

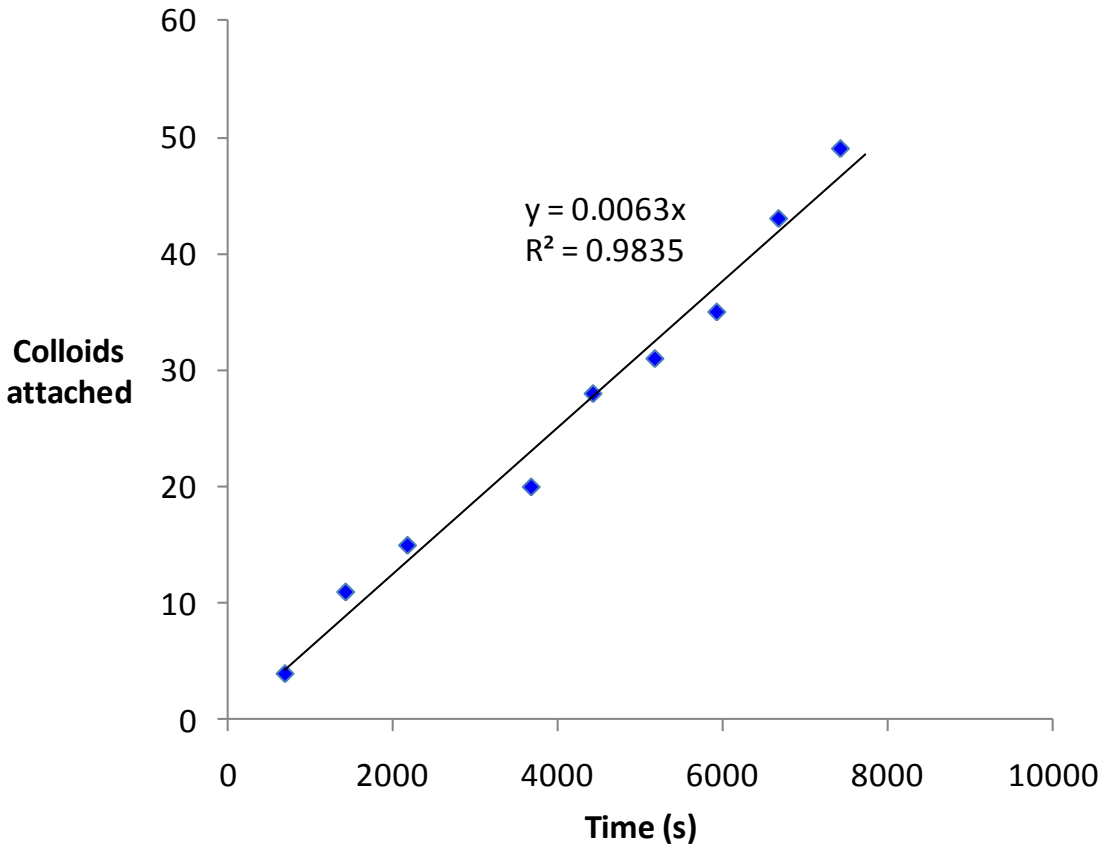


Figure A.2. Experimental deposition slope for 1.1 μm colloids. IS = 6 mM, vjet = $5.94 \times 10^{-3}$ $ms^{-1}$.

## Electric Double Layer Interaction

The electric double layer force between colloid-collector was calculated from the energy expression developed by Lin and Weisner[1] for a sphere-plate geometry:

$$W_{sphere-plate} = \frac{64\pi\varepsilon}{\kappa}\left(\frac{k_B T}{ze}\right)\tanh\left(\frac{ze\psi_c}{4k_B T}\right)\tanh\left(\frac{ze\psi_p}{4k_B T}\right)\left[(\kappa a_p - 1)e^{-kH} + (\kappa a_p + 1)e^{-k(H+2a_p)}\right] \quad \text{(A.1)}$$

where $\varepsilon$ is the absolute electric permittivity of water, $\kappa$ is the inverse Debye length, $k_B$ is the Boltzmann constant, $T$ the absolute temperature, $e$ the elementary charge, $z$ the electrolyte valance $\psi_c$ and $\psi_p$ the zeta potentials of collector and colloid, $a_p$ is the colloid radius, and $H$ is the separation distance. The electric double layer force corresponds to the derivative of the above expression with respect to $H$:

$$F_{sphere-plate} = 64\pi\varepsilon\left(\frac{k_B T}{ze}\right)\tanh\left(\frac{ze\psi_c}{4k_B T}\right)\tanh\left(\frac{ze\psi_p}{4k_B T}\right)\left[(\kappa a_p - 1)e^{-kH} + (\kappa a_p + 1)e^{-k(H+2a_p)}\right] \quad \text{(A.2)}$$

The advantage of this relationship is that it has no restrictions of colloid size and IS values, which means that is valid even to small values of the product $\kappa a_p$ (low IS and small particles size).

## GSI versus Linear Approximation

Force profile distributions calculated using GSI and LA approaches for 1.95 μm colloids and two collector surfaces of equivalent heterodomain coverage and different heterodomain sizes (Figure A.3). Colloidal force distributions were generated by locating

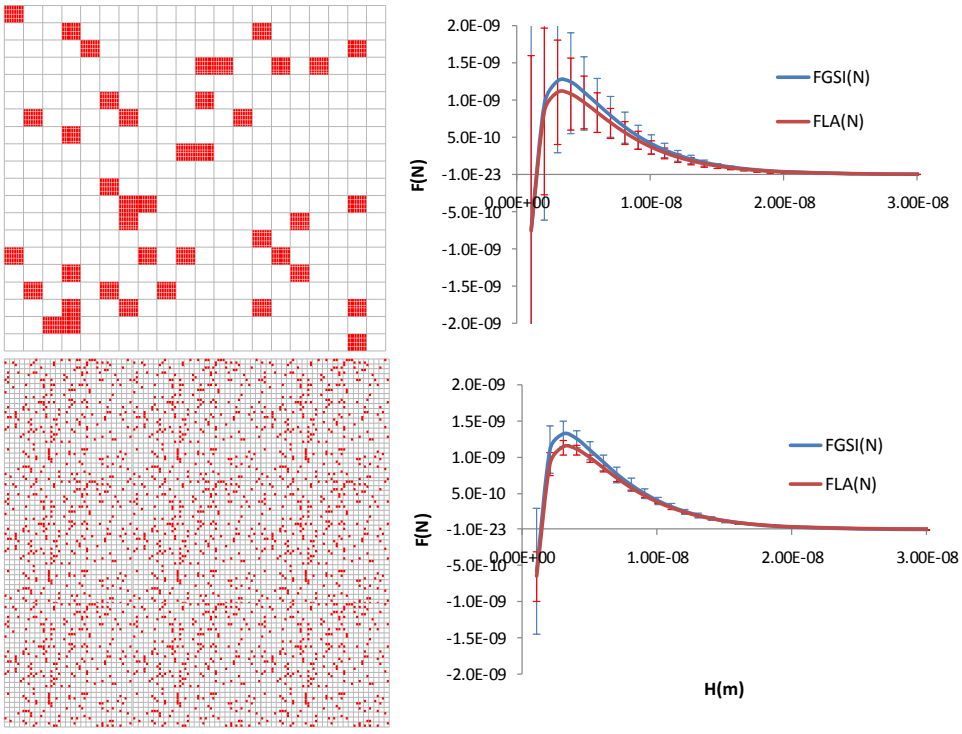


Figure A.3. Exemplary distribution of colloidal force profiles for a 1.95 µm colloid (6 mM IS) for two representative collector surfaces. Top: 80 nm heterodomains 10% surface coverage. Bottom: 10 nm heterodomains 10% surface coverage.

the colloid on 100 different locations (100 different realizations) evenly spaced across a 1.6 µm square modeled surface and calculating the force profile in each location. Force profiles are equivalent for both strategies. Variability, denoted by the standard deviation in the force profile, is proportional to heterodomain size. Small heterodomains (10 nm) have a negligible effect on force profile variability, and so the colloid reads a totally repulsive surface a mean-field surface. Larger heterodomains (80 nm) have an increasing effect on the variability of the force profile, eliminating repulsion for a subset of the realizations, indicating that colloids read a surface that varies from unfavorable to favorable depending on whether the ZOI lies predominantly over a heterodomain.

Sensitivity to Heterodomain ζ Potential

Sensitivity analysis of the influence of heterodomain ζ potential on colloid deposition demonstrate a minimum dependence (Figure A.4). Lesser attractive heterodomains (35 mV) yielded equivalent retention than strongly attractive heterodomains (75 mV). This finding indicates that the first order mechanism of attachment is locating the heterodomain while in the near surface fluid domain. At this stage the colloid diffuse to increasingly most favorable location until immobilization occurs (Figure A.5). The initial strength of interaction with heterodomains is quickly increased and therefore the charge magnitude of the heterodomain is not critical.

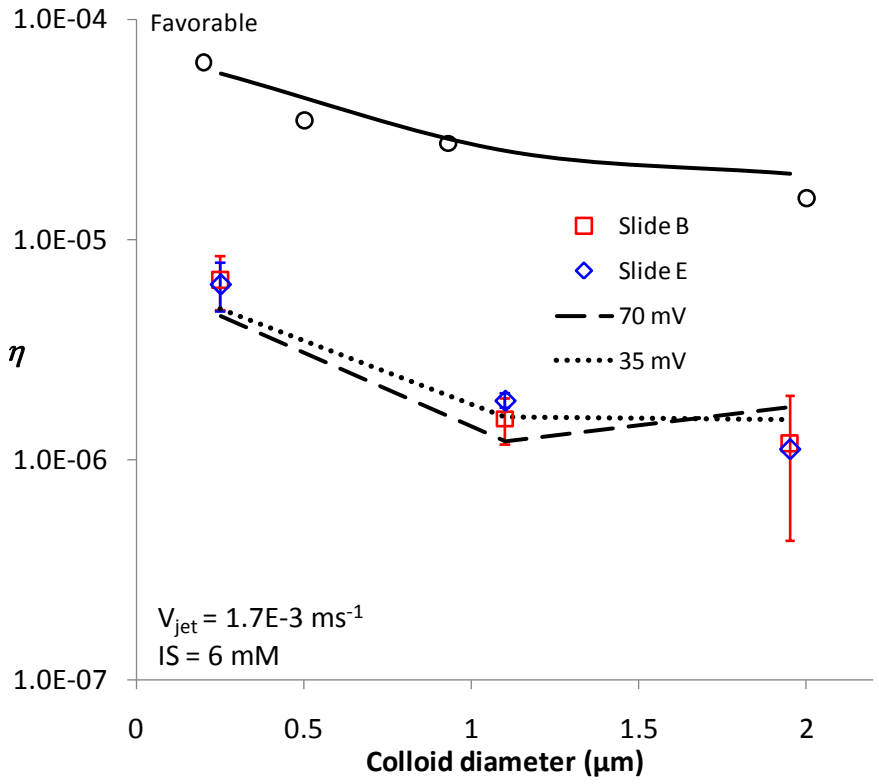


Figure A.4. Colloid retention experimental (open symbols) and simulated (lines) results. Lines correspond to 120 nm heterodomains with different zeta potential, +35 m (dotted line) and +70 mV (dashed line). Error bars denote maximum and minimum for duplicate experiments.

Exemplary Trajectories of Attachment Mechanisms

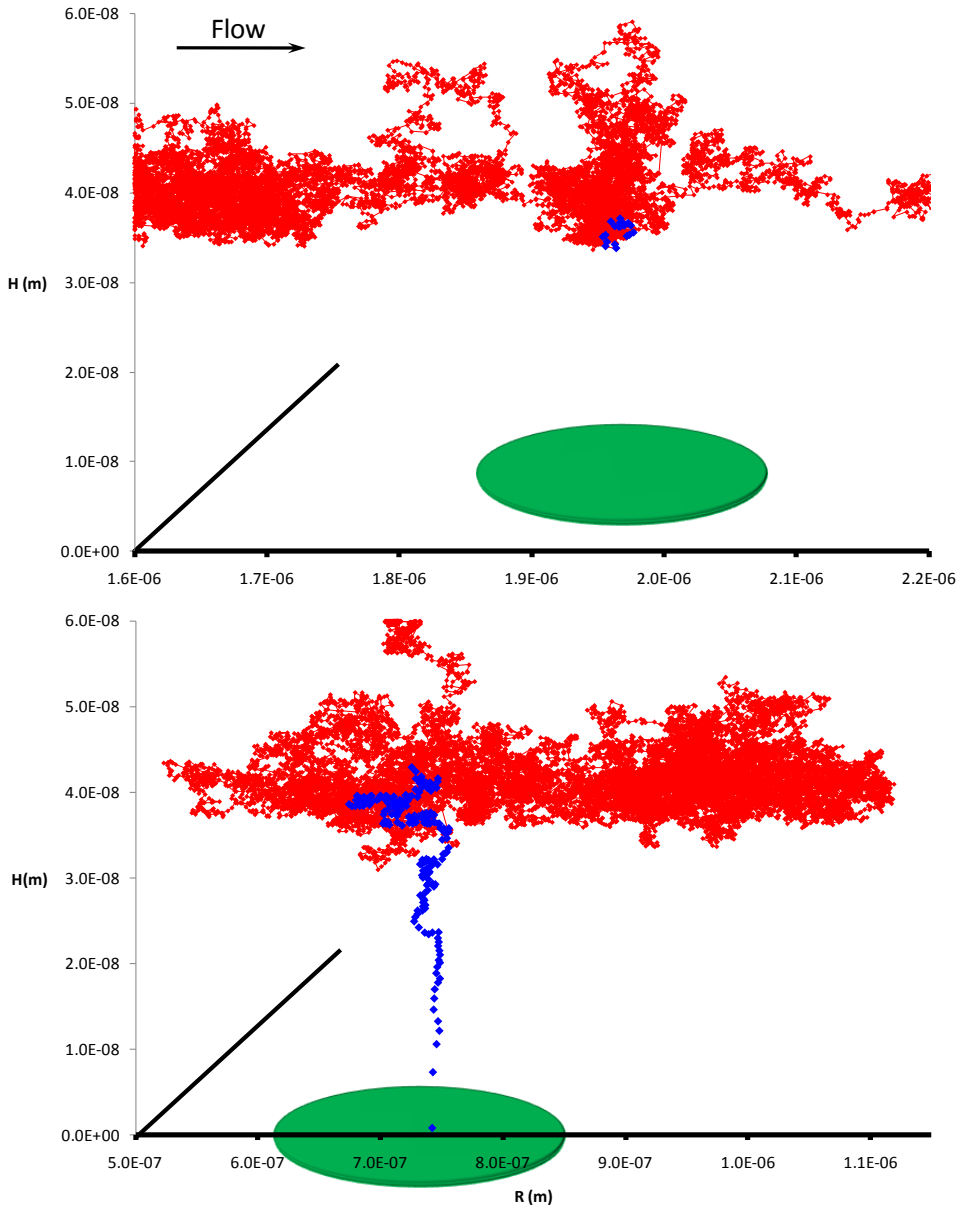


Figure A.5. Example trajectories of ultimately exiting (top) and ultimately attached (bottom) 1.95-µm colloids in the presence heterodomains (green) at $V_{jet}$ = 1.7E-3 $ms^{-1}$, IS = 20 mM. H is the closest separation distance between colloid and collector. R is the radial component. The red portion of the trajectory represents net repulsive colloid-surface interactions. The blue portion represents net attractive interactions (fractional heterodomain area of ZOI > 0.5). The green circles represent the heterodomains interacting with the colloid. Trajectories plotted at every 50 simulated translations.

## Heterodomain Location (Tiling Strategy)

A square subdomain of the collector surface was repeated in a fixed regular grid over the whole collector (Figure A.6) to represent heterogeneity characteristics with the minimum amount of data to be handled during the simulations. In this strategy the heterodomain locations ($x$, $y$ coordinates) are defined only once relative to the origin, $O$. During the simulations this location is shifted to a new origin, $O'$, defined by the grid element over which the position of the colloid is normally projected.

## Flow Intensity Parameter $\xi$

The flow intensity parameter ($\xi$) was fitted to match two fluid velocities regimes ($1.7 \times 10^{-3}$ and $5.94 \times 10^{-3}$ $ms^{-1}$ average jet velocities). The value of unity for $\xi$ represents uniform jet chamber geometry; i.e., height of the chamber corresponds to the diameter of the jet in a 1:1 ratio. In order to account for the 1.22:1 ratio of our jet chamber the parameter $\xi$ was fitted to match simulations under favorable conditions to represent observed delivery of colloids to the impinging surface. The same analysis was repeated for each flow regime (Figure A.7).

## Fluid Flow Field

A numerical flow field subdomain ($r < 100$ um, $z < 50$ um) was defined to fit a simplified solution of the flow field in the near surface near axis region. The numerical flow field solved via a finite element solution of the Navier-Stokes equations was compared to an analytical simplification based on two parameters only. Fitting of $\alpha_f$ parameters was obtained by simultaneous fits of normal ($v_z$) and radial ($v_r$) velocities as shown in Figure A.8.

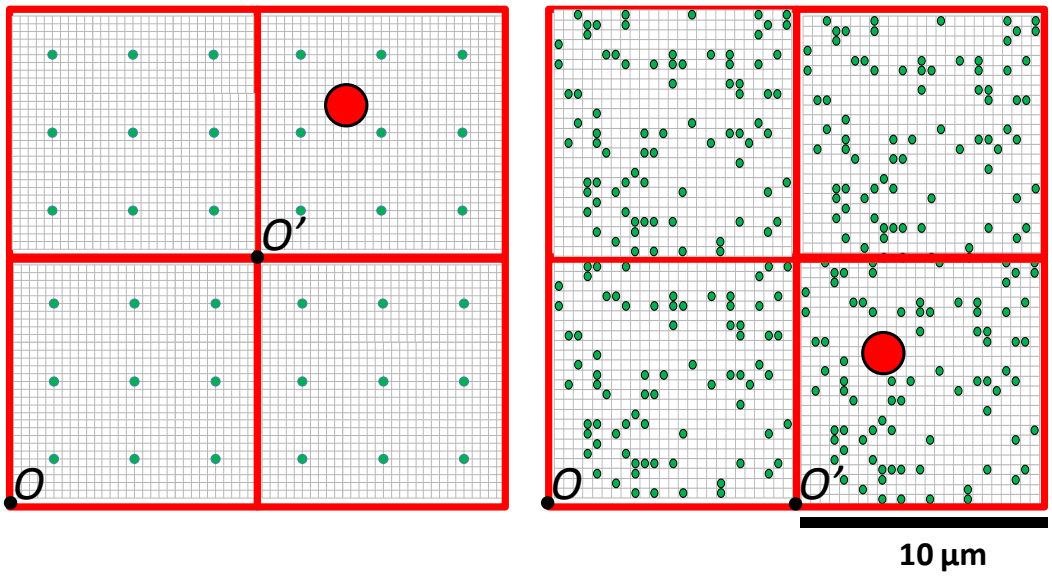


Figure A.6. Exemplary schematic of "tiling" strategy. The red grid represents the uniform fixed locations of 10-µm tiles. The red circle represents the projection of the colloid over the surface and green circles heterodomains. *O'* defines the element on which the colloid is normally projected. Uniform and randomly placed heterodomains surfaces are represented in the left and right panel, respectively.

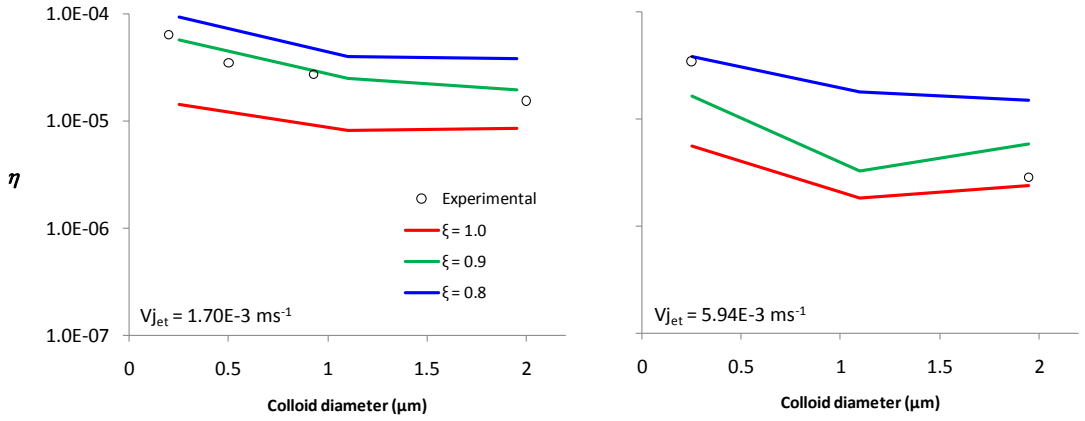


Figure A.7. Fluid in intensity parameter (ξ) fitting. Low (left) and high (right) fluid velocity. The discrete symbols and lines correspond to experimental and simulated values respectively.

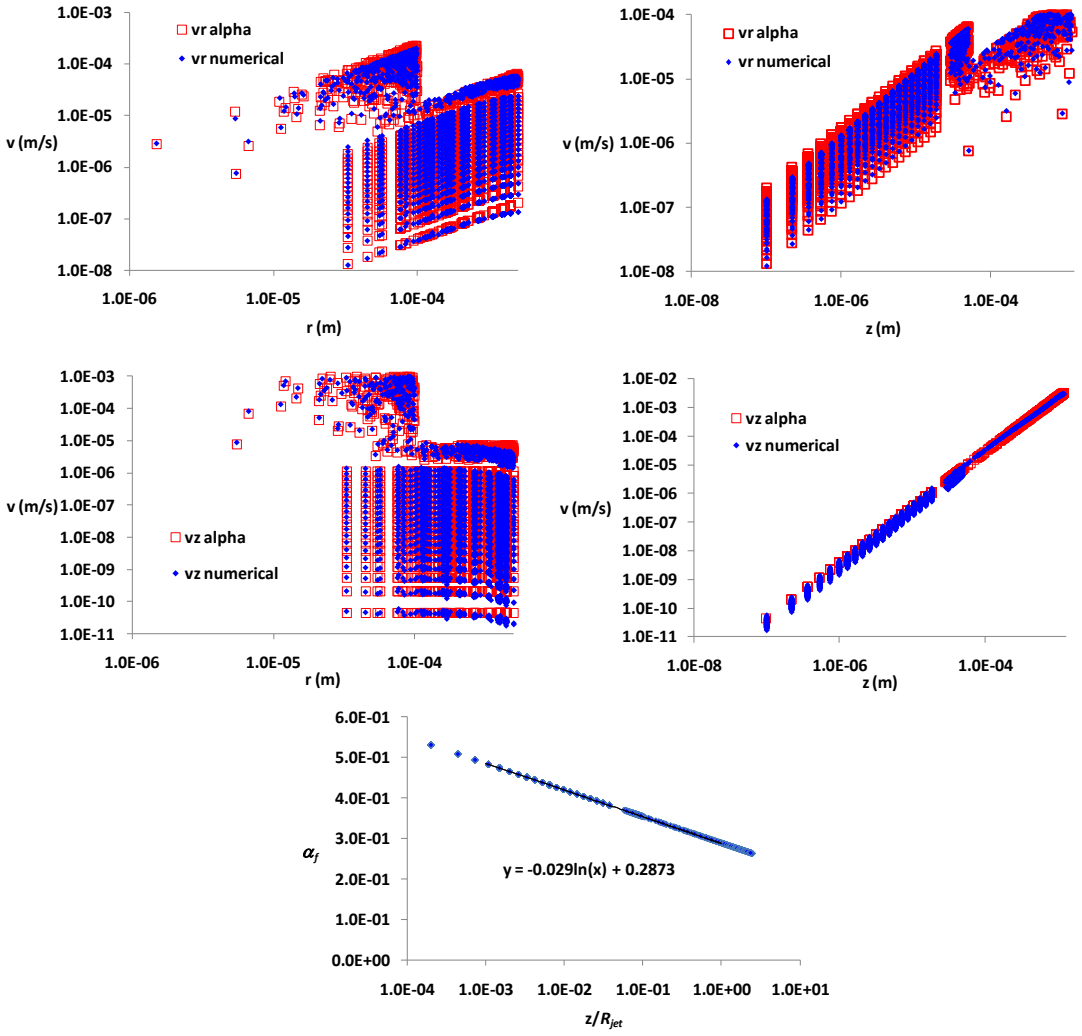


Figure A.8. Coefficient fitting of numerical flow field for jet velocity of 1.7E-3ms-1. Top four panels show *vr* and *vz* as functions of r and z coordinates. Blue is the numerical solution, and red the $\alpha_f$ calculated velocities. Bottom panel: corresponding $\alpha_f$ function that yields an accurate fit.

## Diffusion Force Scaling

Simulations of 500 particles trajectories only due to Brownian force indicated that average particle displacement is equivalent for $\Delta t \geq 10 x dt_{MRT}$ (Figure A.9). In order to match mean expected displacements values a correction factor $C_B$ was fitted to 1.35. Average simulated displacement where within +-3% of the expected mean displacement for of all colloid sizes examined (0.25, 1.1, and 1.95 μm). Parameters for simulations are given in Table A.1.

## Sensitivity to Colloid ζ Potential

Trajectory simulations indicate a minor influence of colloid ζ potential magnitude on colloid retention (Figure A.10). A decrease of z potential from 65.4 to 24.1 mV yielded an increase in retention much smaller than the experimental error bars. This finding suggest that variations in mean field surface charge parameters are not critical for attachment.

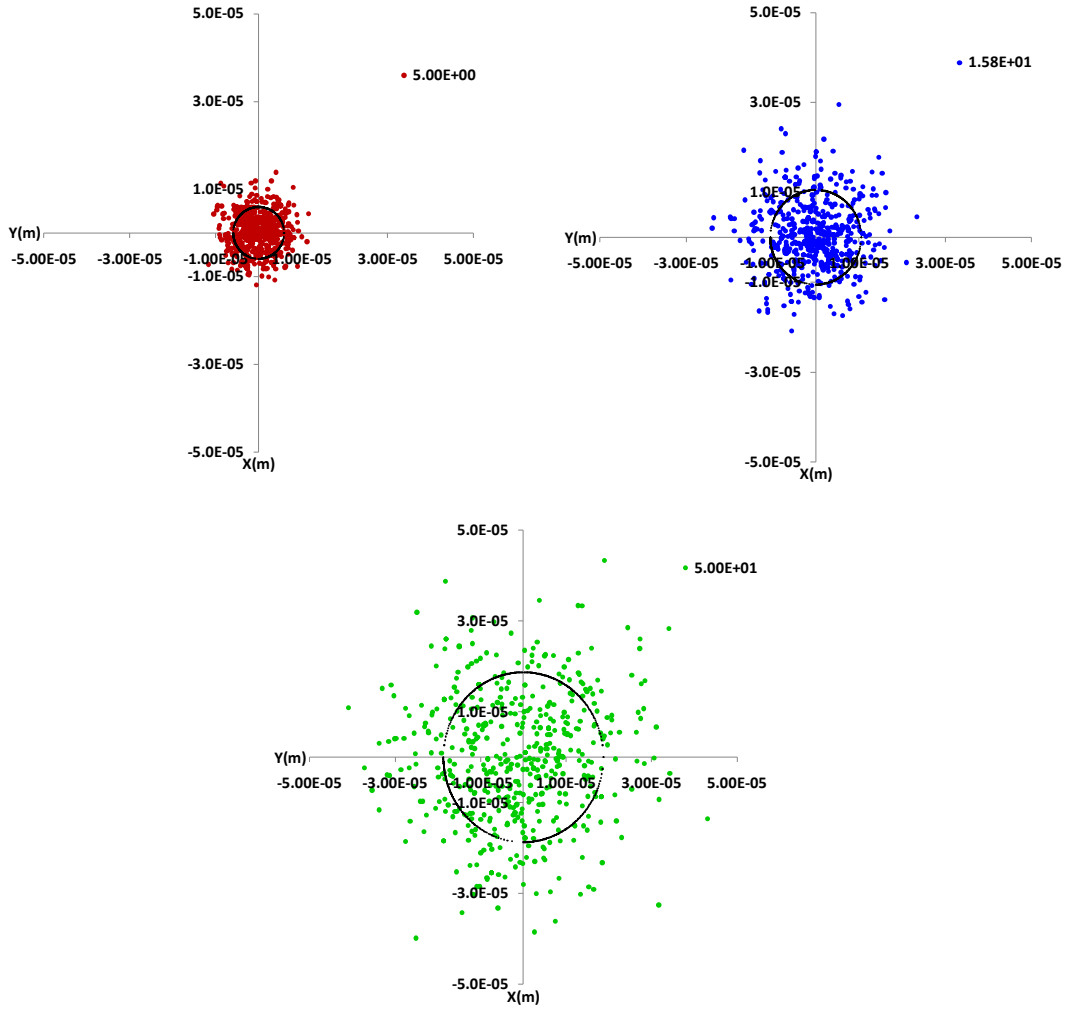


Figure A.9. Exemplary simulation results for displacement of 0.25 μm particles due solely to Brownian motion. Two-dimensional displacement is presented for illustrative purposes. The discrete points correspond to individual locations at 5 (red), 15.8 (blue), and 50 seconds (green). The corresponding expected mean displacements (Eq. 2.7) are represented as circles. Time step, $\Delta t$ = 10 times $dt_{MRT}$. $C_B$ = 1.35.

Table A.1. Parameters used to simulate colloid diffusion

| Colloid diameter | $D_{ES}$ | $dT_{MRT}$ |
|---|---|---|
| (μm) | ($m^2$/s) | (s) |
| 0.25 | 1.75E-12 | 3.67E-09 |
| 1.1 | 3.98E-13 | 7.11E-08 |
| 1.95 | 2.35E-13 | 2.23E-07 |

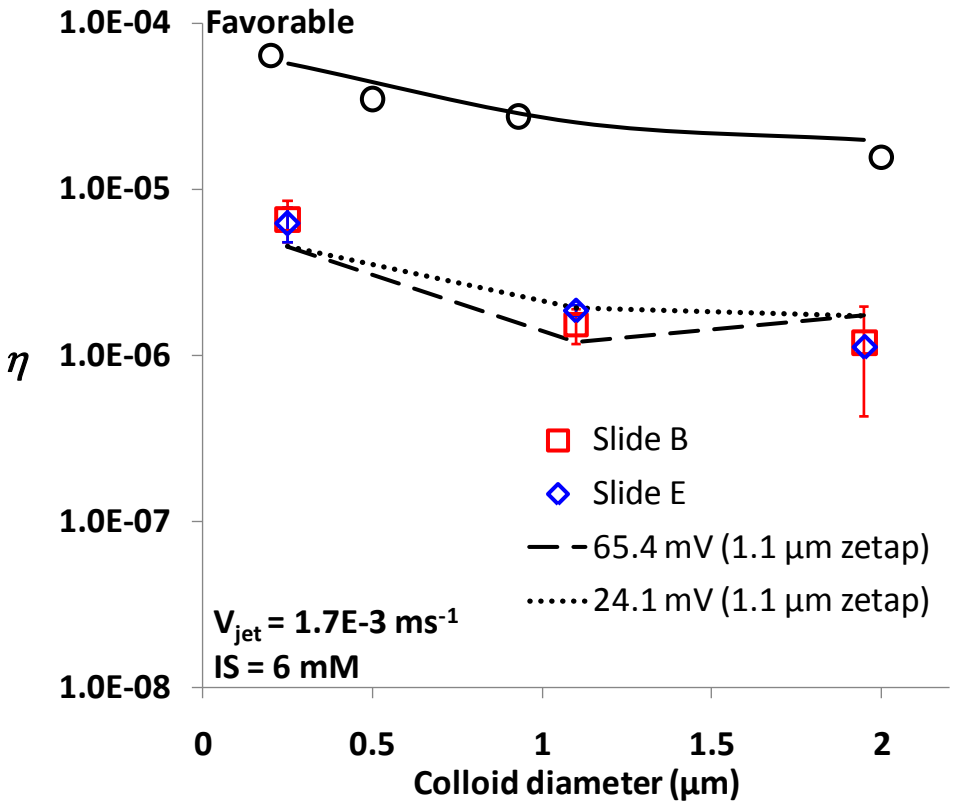


Figure A.10. Sensitivity of retention to different 1.1-µm colloids ζ-potentials (65.4 and 24.1 mV). IS = 6 mM.

References

(1) Lin, S.; Wiesner, M. R. Paradox of Stability of Nanoparticles at Very Low Ionic Strength. *Langmuir* **2012,** *28* (30), 11032–11041.

# APPENDIX B

# SUPPORTING INFORMATION FOR CHAPTER 3

## Fluid Flow Fields of Loading Jet Velocity and 5x and 25x Perturbations

Numerical simulations of the fluid flow field for increased average jet velocity ($v_{jet}$) for a factor 5, 10, and 25 of the loading condition ($v_{jet}$ = 5.94x10$^{-3}$ ms$^{-1}$) show increased vorticity in the system (Figure B.1). These results indicate that the fluid conditions in the experimental system may be not laminar and chaotic, and the perfectly laminar representation of the fluid flow field in the numerical model may not be appropriate to capture colloid release at these higher fluid velocity regimes. Nevertheless the model is able to quantitatively capture release trends with colloid size and fluid velocity, indicating that a first order approximation is achieved in this comparison.

## Distribution of Fractional Areas Occupied by Heterodomains Interacting with Immobilized Colloids

Colloid fractional release is simulated exploiting the discrete heterogeneity approach. In this approach the colloids are immobilized over heterodomains that occupy a significant fraction of the zone of influence. The coupling of the trajectory model and the discrete sites for attachment produces a distribution of fractional areas occupied by heterodomains for a population of immobilized colloids (Figure B.2). This distribution in fractional areas yields a distribution of adhesion energies that dictate the resisting torques that arrested the colloid during the loading phase. During the perturbation phase the driving torque increases. Therefore, only the fraction of colloids with relatively smaller adhesion energies (smaller fractional areas occupied by heterodomains) is released. It is important to indicate that the model predicts instantaneous release, while in reality the process may be kinetically limited and warrants further examination.

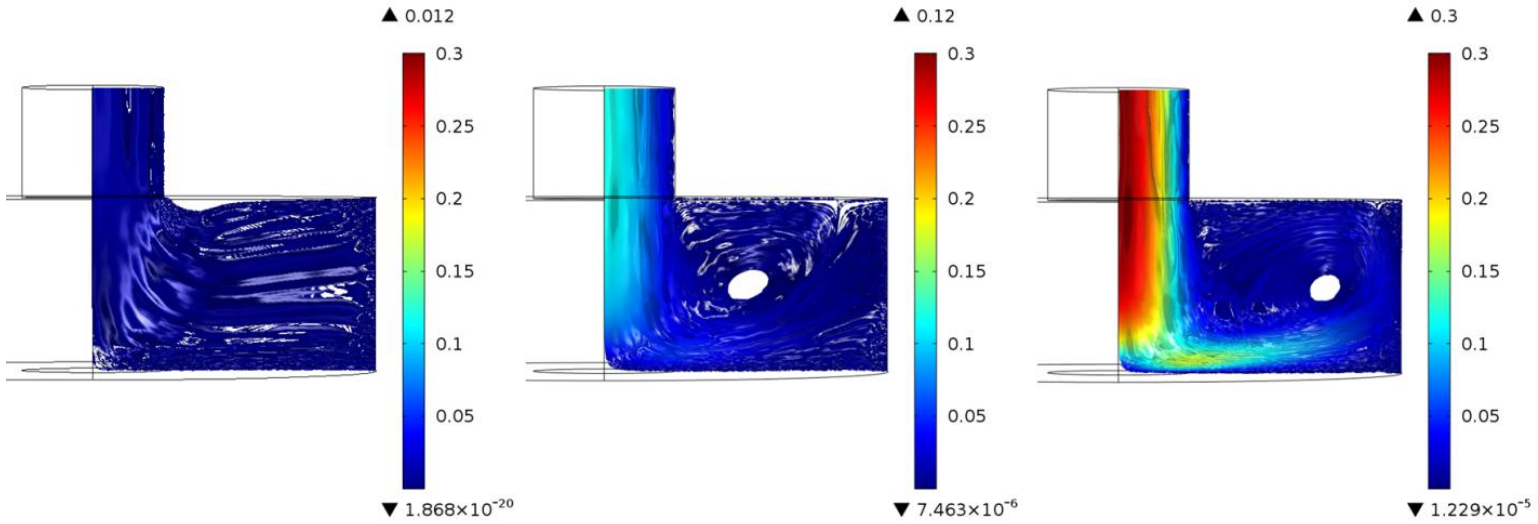


Figure B.1. Velocity flow field streamlines under laminar conditions. Left: nominal loading jet velocity ($v_{jet}$ = 5.94x10$^{-3}$ ms$^{-1}$). Center: 10x flow relative to loading. Right: 25x flow relative to loading. Color map shows velocity values in ms$^{-1}$. Up arrow and down arrow values on legend indicate maximum and minimum velocities in each flow field. The numerical flow fields were solved via the Navier-Stokes equations for a single phase laminar flow model using a finite-element computational software.

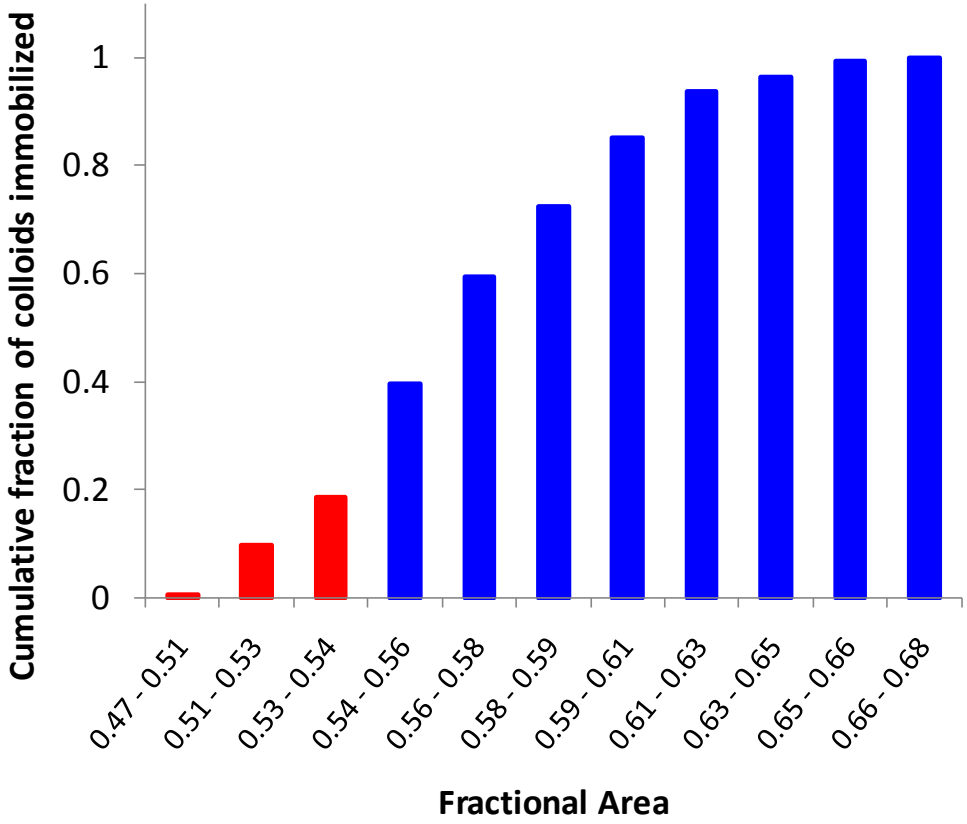


Figure B.2. Cumulative distribution of fractional areas occupied by heterodomains in the zone of influence (ZOI) for 1.95 µm immobilized colloids loaded at 20 mM IS, $1.7x10^{-3}$ ms-1 average jet velocity. Red denotes the fraction of the colloids prone to release in response to IS reduction (20 to 1 mM). Blue denotes the fraction of the colloids that remain attached. Simulated heterogeneity involved 120 and 60 nm radii heterodomains at 1 to 4 number ratio, respectively, at surface coverage 0.04%.

Electric Double Layer Interactions

The electric double layer force between colloid-collector was calculated from the energy expression developed by Lin and Weisner[1] for sphere-plate geometries:

$$W_{sphere-plate} = \frac{64\pi\varepsilon}{\kappa}\left(\frac{k_BT}{ze}\right)\tanh\left(\frac{ze\psi_c}{4k_BT}\right)\tanh\left(\frac{ze\psi_p}{4k_BT}\right)\left[(\kappa a_p - 1)e^{-kH} + (\kappa a_p + 1)e^{-k(H+2a_p)}\right] \quad \text{(B.1)}$$

where $\varepsilon$ is the absolute electric permittivity of water, $\kappa$ is the inverse Debye length, $k_B$ is the Boltzmann constant, $T$ the absolute temperature, $e$ the elementary charge, $z$ the electrolyte valance $\psi_c$ and $\psi_p$ the zeta potentials of collector and colloid, $a_p$ is the colloid radius, and $H$ is the separation distance. The electric double layer force corresponds to the derivative of the above expression with respect to $H$:

$$F_{sphere-plate} = 64\pi\varepsilon\left(\frac{k_BT}{ze}\right)\tanh\left(\frac{ze\psi_c}{4k_BT}\right)\tanh\left(\frac{ze\psi_p}{4k_BT}\right)\left[(\kappa a_p - 1)e^{-kH} + (\kappa a_p + 1)e^{-k(H+2a_p)}\right] \quad \text{(B.2)}$$

van der Waals Interactions

The retarded van der Waals force was calculated from the energy expression provided by Gregory[2] for a sphere plate geometry:

$$W_{sphere-plate} = -\frac{A_{132}a_p}{6H}\left[1 - \frac{5.32H}{\lambda}ln\left(1 + \frac{\lambda}{5.32H}\right)\right] \quad \text{(B.3)}$$

where $A_{132}$ is the Hamaker constant and $\lambda$ is the characteristic wavelength. The van der Waals force corresponds to the derivative of the above expression with respect to $H$:

$$F_{sphere-plate} = -\frac{A_{132}a_p}{6H}\left[6H^2\left(1 + \frac{5.32H}{\lambda}\right)\right] \quad \text{(B.4)}$$

## Steric Interactions

The steric force was calculated from the expression provided by Israelavichli,[3] which corresponds to the energy per unit area between two plates:

$$w_{plate-plate} = W_0 e^{-\frac{H}{\lambda_0}} \quad \text{(B.5)}$$

where $\lambda_0$ is the decay length and $W_0$ the maximum repulsive energy per unit area. The steric force was calculated via the Derjaguin approximation yielding:

$$F_{sphere-plate} = 2\pi a_p W_0 e^{-\frac{H}{\lambda_0}} \quad \text{(B.6)}$$

## Time-lapse Images

A time-lapse image acquisition is provided as a movie: "*Colloid reentrainment 1.7e-3 ms-1 1.95 um 20mM to 1 mM.avi,"* which shows release of 1.95 μm colloids in response to reduced ionic strength (20 to 1 mM). This material is available free of charge via the Internet at http://pubs.acs.org.

## References

(1) Lin, S.; Wiesner, M. R. Paradox of Stability of Nanoparticles at Very Low Ionic Strength. *Langmuir* **2012**, *28* (30), 11032–11041.

(2) Gregory, J. Approximate Expressions for Retarded van der Waals Interaction. *J. Colloid Interface Sci.* **1981,** *83* (1), 138–45.

(3) Israelachvili, J. N., *Intermolecular and Surface Forces: Revised Third Edition*. Elsevier Science: Atlanta, 2011.

(4) COMSOL Multiphysics™, http://www.comsol.com.

# APPENDIX C

# SUPPORTING INFORMATION FOR CHAPTER 4

## Introduction

Classic Colloid Filtration Theory (CFT) provides good predictions of the mass transport of colloids to porous media surfaces under simple conditions lacking colloid-collector repulsion (favorable attachment conditions) for uniform porous media and spherical collectors and colloids. CFT yields a collector efficiency ($\eta$) that represents the fraction of colloids in the bulk fluid that reach the near surface fluid domain in a given unit cell, which is most commonly the Happel sphere-in-cell unit collector.[1–5]

The CFT-based $\eta$ is upscaled based on the unit collector geometry to develop a rate constant ($k_f$) for colloid delivery to the near-surface fluid domain. The equation below corresponds to the Happel sphere-in cell unit cell, whereas other geometries exist such as the Hemisphere-in-cell, [6] constricted tube,[7] and random-packed spheres[8]

$$k_f = -\frac{3(1-\varepsilon)^{1/3}}{2d_c}\ln(1-\eta)v \qquad \text{(C.1)}$$

where $d_c$ is the grain diameter and $\varepsilon$ is the porosity.

Under conditions where colloid-collector repulsion is absent, delivery to the near surface yields attachment, and the rate constant according to Equation 7.1 can be included in the advection-dispersion equation to represent colloid removal from the mobile phase during transport

$$\frac{\partial C}{\partial t} = -v\frac{\partial C}{\partial x} + D\frac{\partial^2 C}{\partial x^2} - k_f C \qquad \text{(C.2)}$$

where $C$ is the concentration of colloids in the mobile phase, $v$ is the average pore water velocity, $D$ is the dispersion coefficient, and $x$ is the independent spatial variable for

transport distance.

It is well known that in the presence of colloid-collector repulsion that is typical of environmental settings, colloid delivery to the collector surface (near-surface fluid domain) does not necessarily yield attachment. The number of colloids that attach relative to the number that enter the near-surface fluid domain is called the attachment or collision efficiency ($\alpha$), and the equation for the colloid attachment rate constant in the presence of colloid-collector repulsion (unfavorable conditions) becomes

$$k_f = -\frac{3(1-\varepsilon)^{1/3}}{2d_c}\ln(1-\alpha\eta)v \qquad \text{(C.3)}$$

Equivalent Happel Sphere and Impinging Jet Fluid Flow Fields

In order to compare collector efficiencies ($\eta$) and collision efficiencies ($\alpha$) among impinging jet and other experimental systems for colloid transport, we developed the following algorithm in which the fluid velocities are matched across a subdomain volume ($V_{env,jet}$) of the impinging jet chamber and the forward flow stagnation zone of the Happel cell (Figure C.1 left).

These subdomains are defined relative to the forward flow stagnation axis in both systems (Figure C.1). The flow field volume is defined by the radius of observation in the jet ($R_{obs}$) and by the thickness of the fluid envelope ($s$) in the Happel cell. In the jet experimental system, $R_{obs}$ corresponds to 219 μm to represent a circular area of equivalent surface as the rectangular area of observation (450x336 μm), defined by the optical setup and magnification (20X) in the microscope.[9]

In the jet, the fluid subdomain is bounded by the flow line that connects the projection of $R_{obs}$ at a distance $s$ from the impinging surface (Figure C.1 right). The

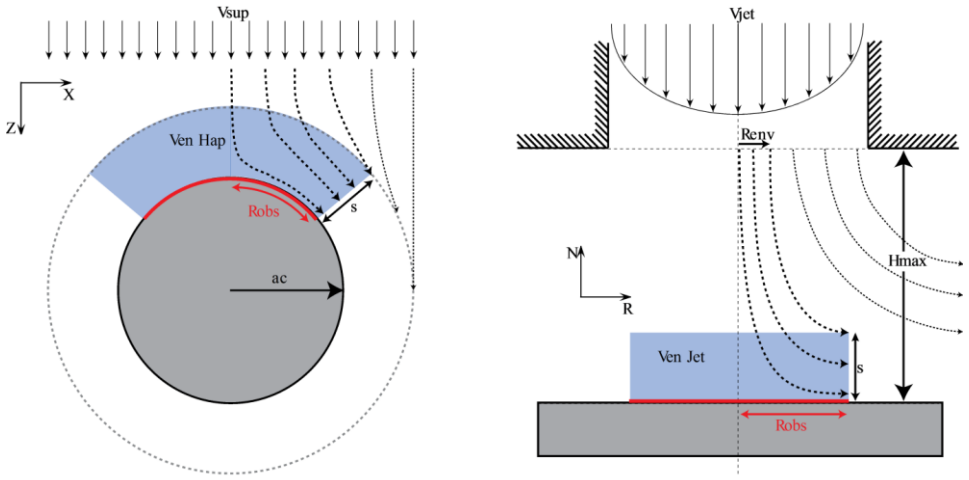


Figure C.1. Happel sphere (left) and impinging jet (right) geometries. The blue area represents the subdomain on which both flow fields are matched, and the gray area represents the collector surface. Colloid injection in the Happel sphere occurs at uniform velocity across the whole projection of the fluid shell (light blue) on a plane normal to the flow direction.

injection location of this flow line (at the jet exit) defines the maximum radius of injection ($R_{env}$) of the subdomain. In our system, $R_{env}$ is somewhat smaller (approximately 5%) than the radius of the jet. A smaller radius $R_{lim}$ is defined by the injection locations of the trajectories that intercept the surface under favorable conditions.

In the impinging jet simulations, beyond a limiting radius ($R_{lim}$) defined by observation area, colloid size, and fluid velocity, injected colloids will not intercept the collector surface. Therefore simulations minimize numerical demand by injecting within $R_{lim}$. Thus, determination of $\eta$ in the impinging jet (representing the porous media) requires extrapolation of the number of colloids that were injected within $R_{lim}$ to a value representing the number that would have been injected within $R_{env}$. The specific steps to perform this transformation are provided below.

## Calculation of Collector Efficiency from Trajectory Simulation Output

While the single collector efficiency of a Happel sphere is already provided elsewhere (e.g., described by Tien and Ramarao[10]), $\eta$ in the impinging jet system is calculated as follows (using the same approach described in Pazmino et al.[9]):

$$\eta = \frac{\left(\frac{\#_{attached}}{time}\right)_{A_{obs}}}{\left(\frac{\#_{injected}}{time}\right)_{A_{env}}} \tag{C.4}$$

where $A_{env}$ and $A_{lim}$ are the cross section areas defined by $R_{env}$ and $R_{lim}$. The total number injected in the subdomain is equal to

$$\left(\frac{\#_{injected}}{time}\right)_{A_{env}} = \frac{Q_{A_{env}}}{Q_{A_{lim}}}\left(\frac{\#_{injected}}{time}\right)_{A_{lim}} \tag{C.5}$$

where the ratio between flow rates can be calculated integrating a parabolic velocity profile across the jet exit, obtaining

$$\frac{Q_{A_{env}}}{Q_{A_{lim}}} = \frac{{R_{env}}^2\left(1-\frac{{R_{env}}^2}{3{R_{jet}}^2}\right)}{{R_{lim}}^2\left(1-\frac{{R_{lim}}^2}{3{R_{jet}}^2}\right)} \tag{C.6}$$

where $R_{jet}$ is the radius of the jet.

Note that the extrapolation ratio from $A_{lim}$ to $A_{env}$ is independent of the fluid velocity and only depends upon the geometry of the jet and the grain size and porosity represented via $R_{env}$. The velocity dependence is built into the simulation via the parameter *#attached/time*.

## Matching Fluid Velocities across Impinging Jet and Happel Fluid Subdomains

Fluid velocity flow fields are matched between the Happel and the jet subdomains (Figure C.1) via comparison of fluid velocity vectors across a 2D slice of the Happel flow field at the front stagnation point (vx and vz) and the normal and radial components of the jet flow field ($v_z$ and $v_R$).

In the Happel fluid subdomain, the normalized (dimensionless) fluid vectors are calculated as described by Rajagopalan and Tien[3]:

$$v_x = -\frac{xz}{r^2}\left(-\frac{3K_1}{2r^3} - \frac{K_2}{2r} + K_4 r^2\right) \quad \text{(C.7)}$$

$$v_z = \frac{z}{r^2}\left(\frac{K_1}{r^3} + \frac{K_2}{r} + K_3 + K_4 r^2\right) + \frac{x^2}{2r^2}\left(-\frac{K_1}{r^3} + \frac{K_2}{r} + 2K_3 + 4K_4 r^2\right) \quad \text{(C.8)}$$

where *r* is the distance from the center of the grain normalized to its radius and *x* and *z* are the corresponding normalized coordinates. The parameters $K_1$ to $K_4$ are defined as follows:

$$K_1 = 1/w \quad \text{(C.9)}$$

$$K_2 = (3 + 2p^5)/w \quad \text{(C.10)}$$

$$K_3 = p(2 + 3p^5)/w \quad \text{(C.11)}$$

$$K_4 = -p^5/w \quad \text{(C.12)}$$

where $K_1$ *to* $K_4$ are purely geometric parameters depending solely on the porosity via the functions *w* and *p*, defined as

$$w = 2 - 3p + 3p^5 - 2p^6 \quad \text{(C.13)}$$

$$p = (1 - \varepsilon)^{1/3} \tag{C.14}$$

The Happel flow field is oriented such that the superficial velocity direction coincides with the -z axis, and the overall dimensionless flow field is scaled directly by the multiplication of each vector by the superficial water velocity to obtain the real-units flow field.

In the jet, radial and normal fluid velocities are approximated utilizing two continuous expressions as described in Pazmino et al.[9] as follows:

$$v_R = v_{jet}\alpha_f \left(\frac{N}{\xi R_{jet}}\right)^2 \tag{C.15}$$

$$v_N = -v_{jet}\alpha_f \left(\frac{N}{\xi R_{jet}}\right)\left(\frac{R}{R_{jet}}\right) \tag{C.16}$$

where $v_{jet}$ is the average jet velocity, $N$ and $R$ are the normal and radial coordinates, $\xi$ is a z-scaling factor calibrated to a value of 0.90 for our experimental system, and $\alpha_f$ is a fluid intensity parameter that is a function of height from the impinging surface:

$$\alpha_f = \alpha_{f1}\, ln\left(\frac{N}{R_{jet}}\right)^2 + \alpha_{f2} \tag{C.17}$$

and $\alpha_{f1}$ and $\alpha_{f2}$ are two fitting coefficients that are calibrated to numerical solutions of the jet flow field.

In order to match both flow fields, the Happel velocity $v_x$ and $v_z$ vectors were transformed to normal and tangential relative to the grain surface. The normal and tangential Happel flow field vectors were directly compared with the normal and radial impinging jet flow field vectors for an equivalent fluid shell thickness. Figure C.2

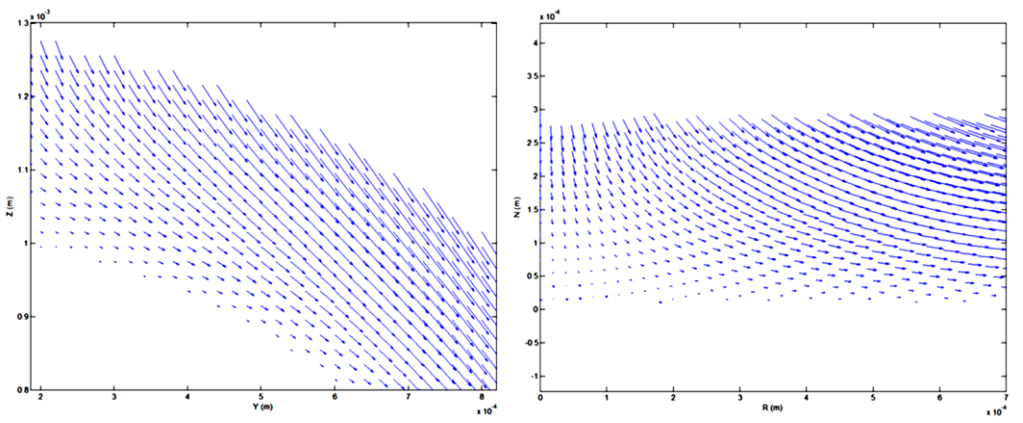

Figure C.2. Comparison of impinging jet and Happel sphere-in-cell fluid flow fields. Left: Happel sphere flow field vectors over a front stagnation point. Right: Reoriented Happel flow field for a flat front stagnation point.

visually demonstrates this process. The underlying assumption is that the curved surface of the front stagnation point of a grain can be reasonably approximated to a flat stagnation point in the jet.

Note that the Happel system can be matched to the jet system via fitting the superficial velocity; similarly the jet flow field can be matched to represent a given grain size porosity and pore water velocity via matching $v_{jet}$ and the $\alpha_{f1}$ and $\alpha_{f2}$ parameters. An exemplary match of fluid vectors in both Happel and jet fluid subdomains is provided in Figure C.3.

## Substantiation of the approach

We substantiate the approach by comparing predictions under favorable conditions from impinging jet simulations and other correlation equations for porous media from the literature.[8,11–13] Because the value of $\eta$ is dependent on the unit cell geometry (e.g., Happel sphere-in-cell versus Hemisphere-in-cell), we make this comparison in terms of the deposition rate coefficient ($k_f$). We arbitrarily chose a media

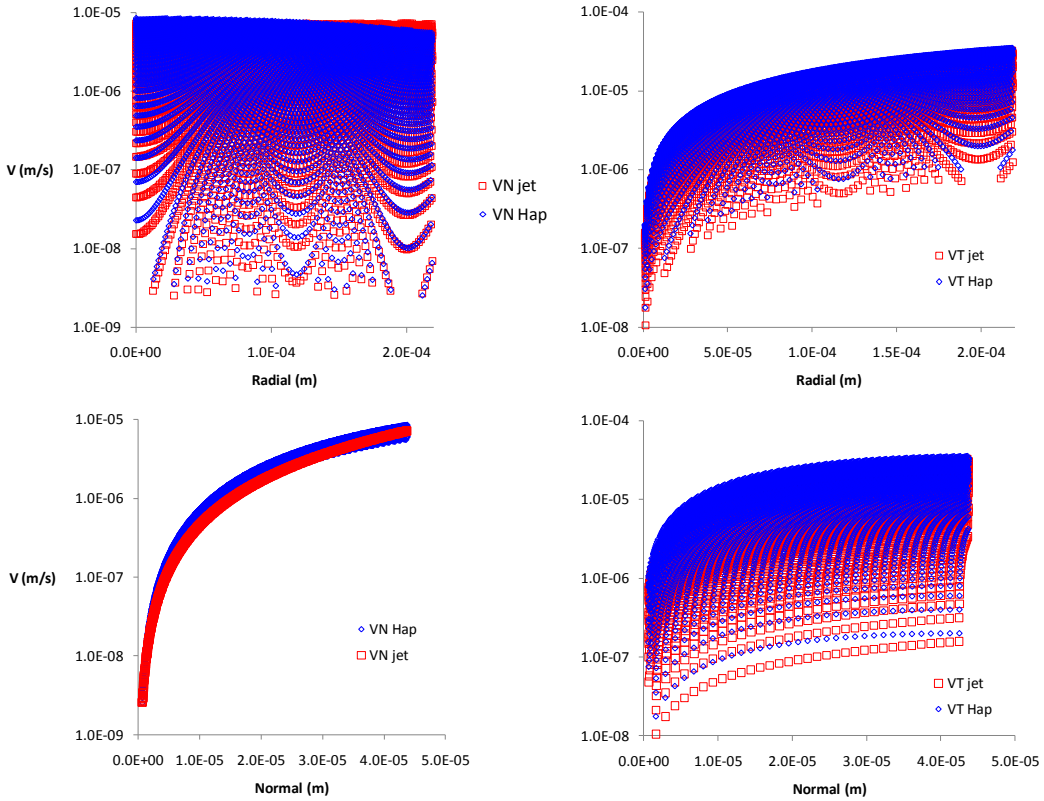


Figure C.3. Matching of impinging jet and Happel sphere-in-cell flow field parameters. Happel (blue diamonds) and impinging jet (red squares) normal and tangential velocity magnitudes. Average jet velocity is 147 $mday^{-1}$. Corresponding Happel sphere average water velocity is 1.9 $mday^{-1}$ for a 510-µm grain and 0.378 porosity.

grain size of 510 µm in diameter and porosities of 0.378 and 0.282 for this comparison.

Comparison of these impinging-jet based $k_f$ values with predictions based on existing correlations equations showed good agreement (~ factor of 2) across three different flow regimes for the nominal porosity ($\varepsilon$ = 0.378). For the low porosity ($\varepsilon$ = 0.282) and low velocity conditions (Figure C.4 bottom left panel), only the correlations that perform well are shown, NG [4] and MPFJ,[13] while the rest of the correlation equations predicted values of $\eta$ greater than unity for at least one condition among the range of colloid sizes examined (0.1–2.0 µm).

The good agreement of the simulated colloid retention in the impinging jet and the

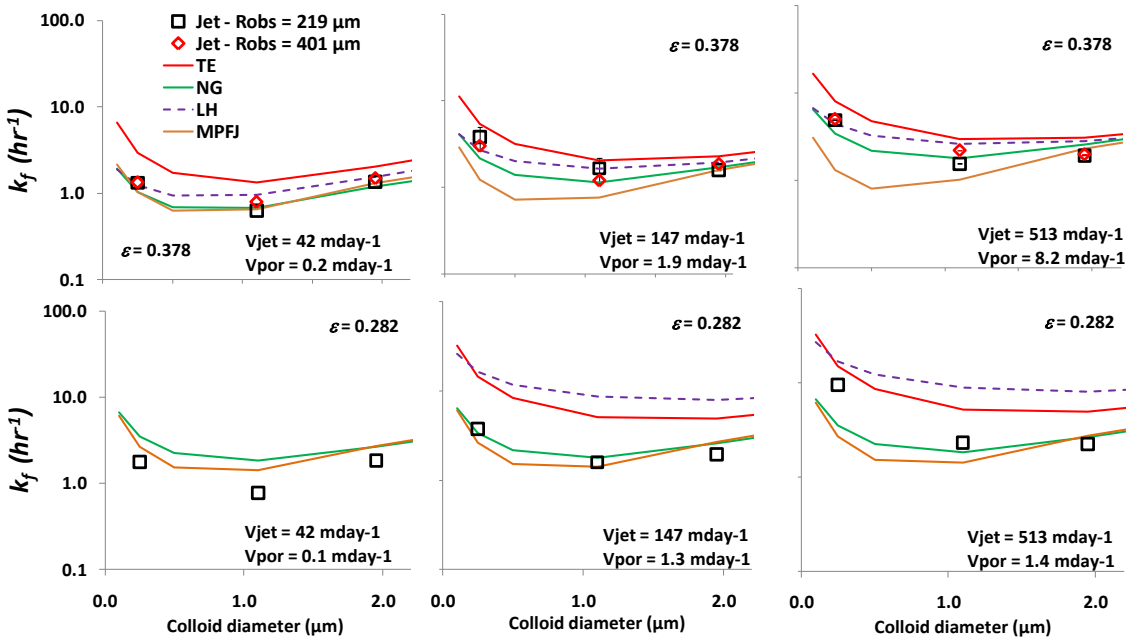


Figure C.4 Simulation and experimental results for colloid deposition under favorable conditions. Deposition rate coefficient results for favorable conditions at different regimes obtained from simulations in the impinging jet system (discrete symbols) and calculated from correlation equations TE (Tufenkji and Elimelech, 2004) and MPFJ (Ma et al. 2013). The corresponding average jet and water velocities yielded equivalent fluid flow fields representing a collector of 510 µm in diameter and porosities of 0.378 (Top panels) and 0.282 (Bottom panels).

predictions of existing correlation equations for a representative range of pore water velocity regimes (0.1 to 8.2 $mday^{-1}$) and porosities (0.282 and 0.378) (Figure C-4), demonstrate that the transformation between jet and Happel geometries is robust.

## Fraction of Colloids in BTC Tailing versus Retained in the Sediment

Colloid mass balance obtained via integration of breakthrough curves (BTC) and sediment-retained profiles revealed that the mass in the tailing part of the BTC is insignificant relative to the mass deposited in the porous media, obtained from dissection of the column after elution (Table C.1).

Table C.1. Fraction of colloids in tailing of BTC relative to the number of colloids deposited in porous media experiments.

| Source | Colloid size | Ionic strength | #colloids in BTC tail | #colloids attached | Fraction #BTC tail/#attached |
|---|---|---|---|---|---|
| | (µm) | IS (mM) | (#) | (-) | (-) |
| Li et al. 2004 | 1.1 | 20 | 1.84E+05 | 1.70E+08 | 1.08E-03 |
| Li et al. 2004 | 1.1 | 10 | 1.89E+05 | 7.61E+07 | 2.48E-03 |
| Li et al. 2004 | 1.1 | 6 | 1.37E+05 | 4.83E+07 | 2.84E-03 |
| Li et al. 2004 | 1.1 | 1 | 9.86E+04 | 1.33E+07 | 7.42E-03 |
| Tong &Johnson 2006 | 2 | 50 | 1.80E+03 | 3.25E+06 | 5.53E-04 |
| Tong &Johnson 2006 | 0.1 | 20 | 1.66E+05 | 5.84E+07 | 2.84E-03 |
| Tong &Johnson 2006 | 0.2 | 20 | 1.51E+05 | 3.74E+08 | 4.04E-04 |
| Tong &Johnson 2006 | 0.5 | 20 | 1.74E+05 | 6.56E+07 | 2.65E-03 |
| Tong &Johnson 2006 | 1 | 20 | 5.78E+05 | 3.21E+08 | 1.80E-03 |

## References


(1) Happel, J. Visous Flow in Multiparticle Systems: Slow Motion of Fluids Relative to Beds of Spherical Particles. *AIChE J.* **1958,** *4* (2), 197–201.

(2) Yao, K.-M.; Habibian, M. T.; O'Melia, C. R. Water and Waste Water Filtration: Concepts and Applications. *Environ. Sci. Technol.* **1971,** *5* (11), 1105–1112.

(3) Rajagopalan, R.; Tien, C. Trajectory Analysis of Deep-bed Filtration with the Sphere-in-cell Porous Media Model. *AIChE J.* **1976,** *22* (3), 523–533.

(4) Nelson, K. E.; Ginn, T. R. Colloid Filtration Theory and the Happel Sphere-in-cell Model Revisited with Direct Numerical Simulation of Colloids. *Langmuir* **2005,** *21* (6), 2173–2184.

(5) William, P. J.; Markus, H. Upscaling Colloid Transport and Retention under Unfavorable Conditions: Linking Mass Transfer to Pore and Grain Topology. *Water Resour. Res.* **2013,** *49* (9), 5328–5341.

(6) Ma, H.; Pedel, J.; Fife, P.; Johnson, W. P. Hemispheres-in-cell Geometry to Predict Colloid Deposition in Porous Media. *Environ. Sci. Technol.* **2009,** *43* (22), 8573–8579.

(7) Paraskeva, C. A.; Burganos, V. N.; Payatakes, A. C. Three-dimensional Trajectory Analysis of Particle Deposition in Constricted Tubes. *Chem. Eng. Commun.* **1991,** *108*, 23–48.

(8) Long, W.; Hilpert, M. A Correlation for the Collector Efficiency of Brownian Particles in Clean-bed Filtration in Sphere Packings by a Lattice-Boltzmann Method. *Environ. Sci. Technol.* **2009,** *43* (12), 4419–4424.

(9) Pazmino, E.; Trauscht, J.; Dame, B.; Johnson, W. P. Power Law Size-distributed Heterogeneity Explains Colloid Retention on Soda Lime Glass in the Presence of Energy Barriers. *Langmuir* **2014,** *30* (19), 5412–5421.

(10) Tien, C.; Ramarao, B. *Granular Filtration of Aerosols and Hydrosols;* Elsevier Science: Oxford, U.K., 2007.

(11) Tufenkji, N.; Elimelech, M. Correlation Equation for Predicting Single-collector Efficiency in Physicochemical Filtration in Saturated Porous Media. *Environ. Sci. Technol.* **2004,** *38* (2), 529–536.

(12) Ma, H.; Hradisky, M.; Johnson, W. P. Extending Applicability of Correlation Equations to Predict Colloidal Retention in Porous Media at Low Fluid Velocity. *Environ. Sci. Technol.* **2013,** *47* (5), 2272–2278.

(13) Li, X.; Scheibe, T. D.; Johnson, W. P. Apparent Decreases in Colloid Deposition Rate Coefficients with Distance of Transport under Unfavorable Deposition Conditions: A General Phenomenon. *Environ. Sci. Technol.* **2004,** *38* (21), 5616–5625.

(14) Tong, M.; Johnson, W. P. Excess Colloid Retention in Porous Media as a Function of Colloid Size, Fluid Velocity, and Grain Angularity. *Environ. Sci. Technol.* **2006,** *40* (24), 7725–7731.

(15) Li, X.; Scheibe, T. D.; Johnson, W. P. Apparent Decreases in Colloid Deposition Rate Coefficients with Distance of Transport under Unfavorable Deposition Conditions: A General Phenomenon. *Environ. Sci. Technol.* **2004,** *38* (21), 5616–5625.

(16) Tong, M.; Johnson, W. P. Excess Colloid Retention in Porous Media as a Function of Colloid Size, Fluid Velocity, and Grain Angularity. *Environ. Sci. Technol.* **2006,** *40* (24), 7725–7731.